공학박사 학위논문

Development of Ultrasound-Nanoparticles Drug Delivery System for Cancer Treatment

암 치료를 위한 초음파-나노입자 약물전달체의 개발

2022년 8월

서울대학교 융합과학기술대학원

융합과학부 나노융합전공

김 대 현

Development of Ultrasound-Nanoparticles Drug Delivery System for Cancer Treatment

지도 교수 이 학 종

이 논문을 공학박사 학위논문으로 제출함

2022년 6월

서울대학교 융합과학기술대학원

융합과학부 나노융합전공

김 대 현

김대현의 공학박사 학위논문을 인준함

2022년 6월

위 원 장 박 원 철 (인)

부위원장 이 학 종 (인)

위 원 임 형 준 (인)

위 원 김 미 정 (인)

위 원 박 재 형 (인)

Abstract

Development of Ultrasound-Nanoparticles Drug Delivery System for Cancer Treatment

Daehyun Kim

Program in Nano Science and Technology

Graduate School of Convergence Science & Technology

Seoul National University

Cancer is one of the most lethal diseases, and various studies are currently under investigation in a hope to overcome it. Nevertheless, the most widely used anticancer drugs are often associated with serious side effects in patients, limiting their application. In this publication, a series of studies on ultrasound drug delivery and diagnosis for reduced side effects and improved anticancer effects were conducted. Nanoparticles, which are drug delivery materials used in the experiment, are largely divided into two types composed of organic and inorganic substances. The organic nanoparticles include microbubbles used as contrast agents, liposomes made of phospholipids, albumin nanoparticle based on human

serum albumin, micelles made of polymers and porphyrins, and ultrasound-sensitive liposomes made of phospholipids and porphyrins. Nanoparticles composed of inorganic materials include carbon-based nanoparticles and iron oxide nanoparticles.

First, microbubbles (~1,000nm sized) were conjugated with an immunotherapeutic agent, anti-PD-L1 antibody, to form the immune-microbubble complex (IMC). These microbubbles can absorb the energy of ultrasound and create transient fenestrations around the vascular tissue in the tumor microenvironment. As these microbubbles burst open, the PD-L1 antibody attached to the bubble phospholipid can better target the cancerous cell, improving the efficacy and toxicity as observed in the in vivo experiments (Kim et al 2020). Furthermore, albumin nanoparticles were synthesized using human serum albumin through the desolvation method and their potential as drug delivery vesicles in combination with microbubbles and ultrasound were demonstrated through animal experiments (Kim et al 2020).

In addition, liposome-based approaches were also investigated. First, a small amount of docetaxel was loaded on liposomes made of phospholipids (membrane fusogenic liposomes, MFL) that are designed to fuse with cell membrane. Furthermore, the anti-cancer effects of porphyrin-based liposomes (DLPL) designed to release

chemotherapeutic agents upon ultrasound treatment and not microbubble-based cavitation were confirmed through animal experiments. Finally, after manufacturing micelles by synthesizing polymer and porphyrin, PSMA targeting material was developed and the improvement of imaging performance in prostate cancer through photoacoustic equipment was confirmed through animal experiments.

If future ultrasound-based chemotherapy experiments and ROS formation in porphyrins are carried out, it is suggested that these particles can be used for diagnosis and treatment at the same time.

In nanoparticles composed of inorganic materials, improved MRI performance was confirmed in the ultrasound sensitive liposomes, in which the exposure to ultrasound caused the release of iron oxide nanoparticles in a controlled manner. Finally, the drug was loaded by carbon-based nanoparticles and the release of these drugs upon ultrasound treatment and their therapeutic effects were evaluated through in vitro experiments. Although the drug loading on the carbon-based nanoparticles was more than 50%, the release through ultrasound irradiation was less than 10%, so it did not show a high release rate, but cytotoxicity was confirmed by in vitro experiments. Furthermore, it was observed that the interaction with the drug could be controlled by improving the particle surface. It has been suggested that the

development of particles with existing particles can achieve better results. Through combining the ultrasound technology and various nanoparticles-based drug delivery methods that can be used in clinical settings, the possibility of anticancer treatment and diagnostic imaging was confirmed.

Keywords: Cancer, ultrasound, drug delivery, nanoparticle, theranostics.

Student Number: 2017-29842

Contents

List of Figures

2.1. PD-L1 Targeting Immune-Microbubble Complex

2.2. Combination Therapy with Doxorubicin-Loaded Reduced Albumin Nanoparticles and Focused Ultrasound

2.3. Antitumor Efficacy of Focused Ultrasound-MFL Nanoparticles Combination Therapy

2.5. PMP(Porphyrin-Micelle-PSMA) Nanoparticles for Photoacoustic and Ultrasound Signal Amplification

3.1. *In Vitro* Cell Cytotoxicity and MRI imaging of an Iron Oxide Nanoparticle-Loaded Ultrasound Sensitive Liposome(IOL)

3.2. *In vitro* Evaluation of Carbon-Based Nanospheres as Drug Delivery Vesicels in Breast Cancer Cell

List of Tables

2.2. Combination Therapy with Doxorubicin-Loaded Reduced Albumin Nanoparticles and Focused Ultrasound

2.3. Antitumor Efficacy of Focused Ultrasound-MFL Nanoparticles Combination Therapy

2.4. Sonodynamic therapy of Doxorubicin-Loaded Porphyrin-Liposome(DLPL)

Chapter 1
General Introduction

1.1. What is Cancer?

1.1.1. Mechanism of Cancer development

Cancer is one of the most common yet lethal diseases in which some cells in the body grow out of control, damaging not only the organs but also invading to other parts of the body [1]. Cancer cells can start growing almost anywhere in the body; it is a phenomenon in which abnormal or damaged cells proliferate and grow out of control as they mechanism fail to follow the normal cell cycle [2,3]. These cells can form tumors, which can be noncancerous (benign) or cancerous (malignant), of latter which can be lethal.

Benign tumors do not spread or invade surrounding tissues and do not grow back upon removal. On the other hand, malignant tumors often undergo dormancy. Of course, benign tumors may also pose a health risk depending on their size and location. For example, a tumor mass in the brain would be lethal, regardless of whether it is benign or malignant.

When a benign tumor develops in the brain, it can cause serious symptoms and even life-threatening [4].

1.1.2. Statistics of Cancer

The American Cancer Society estimates that by 2021 there will be 1,898,160 cancer cases and 608,570 cancer deaths in the United States alone [5]. Cancer is the most dangerous disease worldwide and is

considered the second leading cause of death in the United States alone as a serious disease [5,6].

1.1.3. Advances in technology for cancer treatment

To overcome cancer, various methods and technologies are actively under investigation. Through the development of novel diagnostic and surgical technology, development of new anticancer drugs, and improved drug delivery methods, we are stepping closer to conquering cancer[7].

Until now, various treatment technologies have been studied. Of the many different methods, the most common treatment for cancer is surgery and chemotherapy [8]. In particular, anticancer drugs have been widely used in clinical practice to date. Nevertheless, various side effects - including damages to normal cells - pose a serious problem due to their low transmissibility to cancer [9,10,11].

In order to overcome these shortcomings - with drug delivery technology in the spotlight - various research on novel substances for drug delivery are being actively conducted [12]. Thanks to the development of nanotechnology, research on drug delivery systems through nanoparticles is ever-expanding [13].

1.2. Nanomedicine

1.2.1. General introductio of Nanomedicine

Nanoparticles used in nanomedicine refer to particles that are about 10 to 1000 nm. The use of these small particles can be increase drug half-life, improve solubility for some hydrophobic drugs, and enhance drug efficacy through controllable and sustained drug release[14].

Nanotechnology was not initially applied to nanomedicine. Nanotechnology first became known to the public through K.Eric Drexler's 1986 book Engines of Creation: The Coming Era of Nanotechnology, and later nanotechnology was introduced to wastewater treatment, textile industry, high-performance batteries, biology, medicine and has been applied to various fields [15]. Through numerous studies, nanotechnology has brought significant improvements in cancer treatment, diagnostic imaging, tissue engineering, and drug delivery systems (DDS) [16,17]. Today, nanotechnology in medicine and life sciences is termed nanomedicine and is regarded as one of the key growth areas in nanotechnology [18].

1.2.2. The role of nanomedicine in drug delivery

Nanomedicine mainly plays an important role in solving major limitations and problems on the delivery system of existing anticancer drugs [19]. A problem with existing DDS is the difficulty in removal of

the residual amount of the drug or the carrier in the body, and substances that are not biodegradable may cause acute and long-term toxicity [20, 21]. Drug administration using nanoparticles is smaller than the amount that is used in conventional drug formulations, and it can also deliver a larger amount around the cancer and alleviate the side effects by using biocompatible materials [22,23].

In addition, the use of nanoparticles may improve the ability to reach the target site, and research and development of cancer diagnosis and treatment (theranostic) through drug delivery control, and smart drug release system through internal and external stimulation are actively conducted in the DDS field [24,25]. Since anticancer drugs tend to be insoluble in water, the use of nanoparticles may increase the drug solubility through enhanced surface-to-volume ratio and thus improving bioavailability [26]. Accordingly, many researchers are developing various types of biocompatible nanomaterials. Currently, typical types of nanoparticles used in clinical practice include liposomes, lipid nanoparticles, polymers, protein-based and metal-based nanoparticles. [27,28].

Nevertheless, despite the many benefits offered by the use of nanoparticles in medicine, there are major challenges and limitations

1.2.3. Limitations of Nanomedicine

The first is the physiological barrier. Nanoparticles used in anticancer therapy face multiple physiological barriers before reaching the desired tumor cells. Through systemic administration, nanoparticles travel through the microvessel wall, extracellular matrix, and plasma membrane, and each barrier interferes with the delivery of nanoparticles [29]. The EPR effect is often present in tumors, but the efficiency of nanoparticle accumulation is not as high because there are regions in the tumor microenvironment with low or no permeability [30]. When nanoparticles reach the interstitial space, transport difficulties arise due to the low convective transport driving force in solid tumors [31,32,33].

Second, there is the distribution problem. Although advances in the field of nanotechnology continue to advance, less than 1% of the injected nanoparticles accumulate in tumors according to a meta-analysis [34]. As the result, it appears that the treatment strategy for malignant tumors has not been optimized yet. The reason for this low efficiency may be due to several physiological reasons of tumor structure [35]. Administered nanoparticles are often eliminated in large amounts by blood circulation prior to reaching the tumor microenvironment [36]. There may be various reasons, but the most common is that it is removed by MPS through opsonization by blood proteins, and the study of how

nanoparticles can diffuse out of the circulation remains a big issue [37]. Tumor tissue is different froms normal tissue. Abnormal vasculature in tumor tissue, overexpression of various biomarkers and high-density ECM are some of the key features found in tumor tissues [38]. These abnormal tumor tissue characteristics are one of the main factors that make nanoparticle delivery inefficient [39]. The ECM of tumors is composed of a cross-linked network of collagen and elastin fibers, proteoglycans and hyaluronic acid, and the highly overexpressed ECM of these tumors acts as a negative factor in the diffusion of nanoparticles [40,41,42]. In addition, compared to the high interstitial fluid pressure (IFP) through excessive cell division of tumor cells, and the significantly higher permeability of the vascular system compared to normal cells, the absence of the lymphatic system makes the penetration of nanoparticles more difficult [42,43,44]. This results in lowering the intratumoral fractionation efficiency of nanoparticles.

1.3. Ultrasound Drug Delivery in Nanomedicine

1.3.1. The Role of Ultrasound in Drug Delivery

To overcome these shortcomings of nanoparticles, additional technologies are required to facilitate drug delivery by helping nanoparticles penetrate the tumor. Various studies are being conducted to improve the penetration of nanoparticles due to external factors, but

among them, ultrasound-assisted delivery improves the accumulation and absorption of nanoparticles by cells and simultaneously enables drug release at the target site [45,46]. It can overcome the disadvantages of existing nanoparticles. In addition, if the drug targeting is improved by ultrasound, the dose of the drug required for the existing anticancer treatment can be lowered, which will lower the associated toxicity in the human body [47,48,49].

Ultrasound has been used clinically for imaging and diagnostic purposes for a long time [50,51]. However, the research and development of ultrasound in nanotechnology has brought a lot of progress in the field of non-invasive treatment technologies [52,53]. Ultrasound has proven its effectiveness in various fields, including cataract, tissue amputation and fracture treatment as well as various carcinomas [54]. In particular, the use of ultrasound in drug delivery has been studied recently in that ultrasound can be directed to trigger drug release at the desired site [55]. The use of ultrasound, in combination with the nanoparticle-based drug delivery systems, can offer solutions to various existing problems in cancer treatment [56,57]. It is possible to overcome the physiological barriers to drug delivery of nanoparticles and the challenges in the controlled release of drugs brought about by the insufficient absorption and accumulation of particles at the tumor, improvingthe not only

efficacy but also reducing side effects of drugs [58,59].

1.3.2. Types of Ultrasonic Drug Delivery Mechanisms

Although various biophysical effects of ultrasound can aid in drug delivery, I would like to introduce three major roles of ultrasound that were investigated in doctoral program: sonoporation, cavitation, and reactive oxygen species (ROS) generation.

First, sonoporation is a phenomenon in which the pore size of the cell membrane increases as physical pressure is applied to the cell membrane [60]. The pores created by sonoporation allow drugs or drug-loaded nanoparticles to enter the cell more easily [61].

Second, sonoporation can also be induced through cavitation. Cavitation is a process initiated as the ultrasonic energy causes expansion and shrinkage of small gas microbubbles, resulting in development, vibration, and decomposition [62]. There are two types of such microbubbles, endogenous and extrinsic [63]. In the case of intrinsic microbubbles, they occur in the cytoplasm, but in the case of extrinsic microbubbles, they are manufactured by surfactant, bubbles, phospholipids, or serum albumin with synthetic gas and are injected externally [64]. Both types of microbubbles can readily absorb ultrasound energy when the cavitation threshold is achieved to induce high-frequency oscillations, which generate jet/shock waves to perturb

the cell membrane [64,65,66]. This improves the permeability of the cell membrane while creating a phenomenon that makes the nanoparticles more accessible [67,68].

Third is ROS generation. The generation of ROS induced by acoustic cavitation of ultrasonic waves is a chemical effect, and the instantaneous temperature and pressure generated by the interaction of ultrasonic waves with cells or microbubbles can cause local temperature to rise up to thousands of K and hundreds of atmospheric pressures [68,69,70]. These extreme temperatures and pressures decompose water and form H_2O_2, which can trigger downstream chain reaction leading to production of free radicals. [71,72]. When this happens, these radicals induce lipid peroxidation on polyunsaturated phospholipids present in the plasma membrane, destroying the cell membrane structure, change the properties of the cell membrane with fluidity, and ultimately cause cell damage [73,74,75].

1.3.3. The future of cancer treatment through ultrasound drug delivery. In fact, although ultrasound technology has already been implemented in clinical practice, ultrasound technology for therapeutic application has not been as actively evaluated. However, recently, the use of ultrasound used with microbubbles has been approved by the FDA for diagnostic purposes, and various substances used in clinical practice have emerged

[76,77,78]. Contrast agents such as Sonovue, Definity, and Optison, and substances that release drugs by ultrasound such as ThermoDox have also been developed [79]. Research and development on cancer treatment using ultrasound is constantly in progress.

1.4. Conclusion

We have conducted various research and development of different substances, focusing primarily on those that can be used in actual clinical practice. During the doctoral period, various types of nanoparticles that can be applied to cancer treatment along with ultrasound exposure, such as liposomes, polymers, microbubbles, carbon bases, iron oxides, and porphyrins, were studied. The potential of these various nanoparticles, in combination with ultrasound, and their feasibility in clinical translation, was evaluated and confirmed.

1.5. Statistical Analysis

Data are expressed as mean ± standard deviation from at least 3 independent experiments. For in vitro experiments, statistical analysis of two groups was calculated with an unpaired two-tailed Student's t-test. For in vivo animal test, one-way ANOVA was used for comparison between groups to determine the significance of the difference in tumor volume. Statistical significance was established as $p < 0.05$.

References

[1] Heng, H. H.; Stevens, J. B.; Bremer, S. W.; Ye, K. J.; Liu, G.; Ye, C. J., The evolutionary mechanism of cancer. Journal of cellular biochemistry 2010, 109 (6), 1072-1084.

[2] Farber, E.; Cameron, R., The sequential analysis of cancer development. Advances in cancer research 1980, 31, 125-226.

[3] Yoshida BA, Sokoloff MM, Welch DR, Rinker-Schaeffer CW (2000) Metastasis-suppressor genes: a review and perspective on an emerging field. J Natl Cancer Inst, 92: 1717-1730.

[4] Patel, A., Benign vs malignant tumors. JAMA oncology 2020, 6 (9), 1488-1488.

[5] Siegel, R. L.; Miller, K. D.; Fuchs, H. E.; Jemal, A., Cancer statistics, 2021. CA: a cancer journal for clinicians 2021, 71 (1), 7-33. [2] Farber, E.; Cameron, R., The sequential analysis of cancer development. Advances in cancer research 1980, 31, 125-226.

[6] Mendoza, T. R.; Wang, X. S.; Cleeland, C. S.; Morrissey, M.; Johnson, B. A.; Wendt, J. K.; Huber, S. L., The rapid assessment of fatigue severity in cancer patients: use of the Brief Fatigue Inventory. Cancer 1999, 85 (5), 1186-1196.

[7] Sudhakar, A., History of cancer, ancient and modern treatment methods. Journal of cancer science & therapy 2009, 1 (2), 1.

[8] DeVita VT Jr, Chu E. A history of cancer chemotherapy. Cancer Res. 2008 Nov 1;68(21):8643-53.

[9] Lindley, C.; McCune, J. S.; Thomason, T. E.; Lauder, D.; Sauls, A.; Adkins, S.; Sawyer, W. T., Perception of chemotherapy side

effects cancer versus noncancer patients. Cancer practice 1999, 7 (2), 59-65.

[10] Amjad, M. T.; Chidharla, A.; Kasi, A., Cancer Chemotherapy. In StatPearls [Internet], StatPearls Publishing: 2021.

[11] Van den Boogaard, W. M.; Komninos, D. S.; Vermeij, W. P., Chemotherapy Side-Effects: Not All DNA Damage Is Equal. Cancers 2022, 14 (3), 627.

[12] Cho, K.; Wang, X.; Nie, S.; Shin, D. M., Therapeutic nanoparticles for drug delivery in cancer. Clinical cancer research 2008, 14 (5), 1310-1316. [13] Farber, E.; Cameron, R., The sequential analysis of cancer development. Advances in cancer research 1980, 31, 125-226.

[13] Haley, B.; Frenkel, E. In Nanoparticles for drug delivery in cancer treatment, Urologic Oncology: Seminars and original investigations, Elsevier: 2008; pp 57-64.

[14] Farber, E.; Cameron, R., The sequential analysis of cancer development. Advances in cancer research 1980, 31, 125-226.

[14] Dang, Y.; Guan, J., Nanoparticle-based drug delivery systems for cancer therapy. Smart Materials in Medicine 2020, 1, 10-19. [15] Farber, E.; Cameron, R., The sequential analysis of cancer development. Advances in cancer research 1980, 31, 125-226.

[15] Farjadian, F.; Ghasemi, A.; Gohari, O.; Roointan, A.; Karimi, M.; Hamblin, M. R., Nanopharmaceuticals and nanomedicines currently on the market: challenges and opportunities. Nanomedicine 2019, 14 (1), 93-126. [17] Farber, E.; Cameron, R., The sequential analysis of cancer development. Advances in cancer research 1980, 31, 125-226.

[16] Kim, B. Y.; Rutka, J. T.; Chan, W. C., Nanomedicine. New England Journal of Medicine 2010, 363 (25), 2434-2443. [19] Farber, E.; Cameron, R., The sequential analysis of cancer development. Advances in cancer research 1980, 31, 125-226.

[17] Freitas Jr, R. A., What is nanomedicine? Nanomedicine: Nanotechnology, Biology and Medicine 2005, 1 (1), 2-9.

[18] Parveen, S.; Sahoo, S. K., Nanomedicine. Clinical pharmacokinetics 2006, 45 (10), 965-988.

[19] Singh, R.; Lillard Jr, J. W., Nanoparticle-based targeted drug delivery. Experimental and molecular pathology 2009, 86 (3), 215-223.

[20] Cukierman, E.; Khan, D. R., The benefits and challenges associated with the use of drug delivery systems in cancer therapy. Biochemical pharmacology 2010, 80 (5), 762-770. [24] Farber, E.; Cameron, R., The sequential analysis of cancer development. Advances in cancer research 1980, 31, 125-226.

[21] Jain, K. K., An overview of drug delivery systems. Drug delivery systems 2020, 1-54. [26] Farber, E.; Cameron, R., The sequential analysis of cancer development. Advances in cancer research 1980, 31, 125-226.

[22] Karmali, P. P.; Simberg, D., Interactions of nanoparticles with plasma proteins: implication on clearance and toxicity of drug delivery systems. Expert opinion on drug delivery 2011, 8 (3), 343-357.

[23] Gill, S.; Löbenberg, R.; Ku, T.; Azarmi, S.; Roa, W.; Prenner, E. J., Nanoparticles: characteristics, mechanisms of action, and toxicity in pulmonary drug delivery—a review. Journal of Biomedical Nanotechnology 2007, 3 (2), 107-119.

[24] Fahmy, T. M.; Fong, P. M.; Goyal, A.; Saltzman, W. M., Targeted for drug delivery. Materials Today 2005, 8 (8), 18-26.

[25] Singh, R.; Lillard Jr, J. W., Nanoparticle-based targeted drug delivery. Experimental and molecular pathology 2009, 86 (3), 215-223.

[26] Guo, S.; Huang, L., Nanoparticles containing insoluble drug for cancer therapy. Biotechnology advances 2014, 32 (4), 778-788.

[27] Zhu, Y.; Liao, L., Applications of nanoparticles for anticancer drug delivery: a review. Journal of nanoscience and nanotechnology 2015, 15 (7), 4753-4773.

[28] Shi, J.; Kantoff, P. W.; Wooster, R.; Farokhzad, O. C., Cancer nanomedicine: progress, challenges and opportunities. Nature reviews cancer 2017, 17 (1), 20-37.

[29] Dang, Y.; Guan, J., Nanoparticle-based drug delivery systems for cancer therapy. Smart Materials in Medicine 2020, 1, 10-19.

[30] Shi, J.; Kantoff, P. W.; Wooster, R.; Farokhzad, O. C., Cancer nanomedicine: progress, challenges and opportunities. Nature reviews cancer 2017, 17 (1), 20-37.

[31] Von Roemeling, C.; Jiang, W.; Chan, C. K.; Weissman, I. L.; Kim, B. Y., Breaking down the barriers to precision cancer nanomedicine. Trends in biotechnology 2017, 35 (2), 159-171.

[32] Ferrari, M., Frontiers in cancer nanomedicine: directing mass transport through biological barriers. Trends in biotechnology 2010, 28 (4), 181-188.

[33] Adiseshaiah, P. P.; Crist, R. M.; Hook, S. S.; McNeil, S. E., Nanomedicine strategies to overcome the pathophysiological barriers of

pancreatic cancer. Nature reviews Clinical oncology 2016, 13 (12), 750-765.

[34] Blanco, E.; Shen, H.; Ferrari, M., Principles of nanoparticle design for overcoming biological barriers to drug delivery. Nature biotechnology 2015, 33 (9), 941-951.

[35] Mitchell, M. J.; Billingsley, M. M.; Haley, R. M.; Wechsler, M. E.; Peppas, N. A.; Langer, R., Engineering precision nanoparticles for drug delivery. Nature Reviews Drug Discovery 2021, 20 (2), 101-124.

[36] Yoo, J.-W.; Chambers, E.; Mitragotri, S., Factors that control the circulation time of nanoparticles in blood: challenges, solutions and future prospects. Current pharmaceutical design 2010, 16 (21), 2298-2307.

[37] Kingsley, J. D.; Dou, H.; Morehead, J.; Rabinow, B.; Gendelman, H. E.; Destache, C. J., Nanotechnology: a focus on nanoparticles as a drug delivery system. Journal of Neuroimmune Pharmacology 2006, 1 (3), 340-350.

[38] Eble, J. A.; Niland, S., The extracellular matrix in tumor progression and metastasis. Clinical & experimental metastasis 2019, 36 (3), 171-198.

[39] Overchuk, M.; Zheng, G., Overcoming obstacles in the tumor microenvironment: Recent advancements in nanoparticle delivery for cancer theranostics. Biomaterials 2018, 156, 217-237.

[40] Subrahmanyam, N.; Ghandehari, H., Harnessing Extracellular Matrix Biology for Tumor Drug Delivery. Journal of Personalized Medicine 2021, 11 (2), 88.

[41] Raavé, R.; van Kuppevelt, T. H.; Daamen, W. F.,

Chemotherapeutic drug delivery by tumoral extracellular matrix targeting. Journal of Controlled Release 2018, 274, 1-8.

[42] Henke, E.; Nandigama, R.; Ergün, S., Extracellular matrix in the tumor microenvironment and its impact on cancer therapy. Frontiers in molecular biosciences 2020, 160.

[43] Zhang, Y. R.; Lin, R.; Li, H. J.; He, W. l.; Du, J. Z.; Wang, J., Strategies to improve tumor penetration of nanomedicines through nanoparticle design. Wiley Interdisciplinary Reviews: Nanomedicine and Nanobiotechnology 2019, 11 (1), e1519.

[44] Miao, L.; Huang, L., Exploring the tumor microenvironment with nanoparticles. Nanotechnology-Based Precision Tools for the Detection and Treatment of Cancer 2015, 193-226.

[45] Larina, I. V.; Evers, B. M.; Ashitkov, T. V.; Bartels, C.; Larin, K. V.; Esenaliev, R. O., Enhancement of drug delivery in tumors by using interaction of nanoparticles with ultrasound radiation. Technology in cancer research & treatment 2005, 4 (2), 217-226.

[46] Papa, A.-L.; Korin, N.; Kanapathipillai, M.; Mammoto, A.; Mammoto, T.; Jiang, A.; Mannix, R.; Uzun, O.; Johnson, C.; Bhatta, D., Ultrasound-sensitive nanoparticle aggregates for targeted drug delivery. Biomaterials 2017, 139, 187-194.

[47] Entzian, K.; Aigner, A., Drug Delivery by Ultrasound-Responsive Nanocarriers for Cancer Treatment. Pharmaceutics 2021, 13 (8), 1135.

[48] Chowdhury, S. M.; Lee, T.; Willmann, J. K., Ultrasound-guided drug delivery in cancer. Ultrasonography 2017, 36 (3), 171.

[49] Ren, W.-W.; Xu, S.-H.; Sun, L.-P.; Zhang, K., Ultrasound-Based Drug Delivery System. Current Medicinal Chemistry 2022.

[50] Harvey, C. J.; Pilcher, J. M.; Eckersley, R. J.; Blomley, M. J.; Cosgrove, D. O., Advances in ultrasound. Clinical radiology 2002, 57 (3), 157-177.

[51] Newman, P. G.; Rozycki, G. S., The history of ultrasound. Surgical clinics of north America 1998, 78 (2), 179-195.

[52] Beik, J.; Mehdizadeh, A.; Shakeri-Zadeh, A., Ultrasound in cancer treatment through nanotechnology. Journal of Biomedical Physics & Engineering 2016, 6 (3), 123.

[53] Tang, M.; Lei, L.; Guo, S.; Huang, W., Recent progress in nanotechnology for cancer therapy. Chin J Cancer 2010, 29 (9), 775-80.

[54] Jain, A.; Tiwari, A.; Verma, A.; Jain, S. K., Ultrasound-based triggered drug delivery to tumors. Drug delivery and translational research 2018, 8 (1), 150-164.

[55] Sennoga, C. A.; Kanbar, E.; Auboire, L.; Dujardin, P.-A.; Fouan, D.; Escoffre, J.-M.; Bouakaz, A., Microbubble-mediated ultrasound drug-delivery and therapeutic monitoring. Expert opinion on drug delivery 2017, 14 (9), 1031-1043.

[56] Zhou, L.-Q.; Li, P.; Cui, X.-W.; Dietrich, C. F., Ultrasound nanotheranostics in fighting cancer: Advances and prospects. Cancer letters 2020, 470, 204-219.

[57] Elkhodiry, M. A.; Momah, C. C.; Suwaidi, S. R.; Gadalla, D.; Martins, A. M.; Vitor, R. F.; Husseini, G. A., Synergistic nanomedicine: passive, active, and ultrasound-triggered drug delivery in cancer treatment. Journal of nanoscience and nanotechnology 2016, 16 (1), 1-18.

[58] Jain, A.; Tiwari, A.; Verma, A.; Jain, S. K., Ultrasound-based

triggered drug delivery to tumors. Drug delivery and translational research 2018, 8 (1), 150-164.

[59] Canavese, G.; Ancona, A.; Racca, L.; Canta, M.; Dumontel, B.; Barbaresco, F.; Limongi, T.; Cauda, V., Nanoparticle-assisted ultrasound: A special focus on sonodynamic therapy against cancer. Chemical Engineering Journal 2018, 340, 155-172.

[60] Lentacker, I.; De Cock, I.; Deckers, R.; De Smedt, S.; Moonen, C., Understanding ultrasound induced sonoporation: definitions and underlying mechanisms. Advanced drug delivery reviews 2014, 72, 49-64.

[61] Wu, J.; Pepe, J.; Rincón, M., Sonoporation, anti-cancer drug and antibody delivery using ultrasound. Ultrasonics 2006, 44, e21-e25.

[62] Wu, J.; Nyborg, W. L., Ultrasound, cavitation bubbles and their interaction with cells. Advanced drug delivery reviews 2008, 60 (10), 1103-1116.

[63] Turánek, J.; Miller, A. D.; Kauerová, Z.; Lukáč, R.; Mašek, J.; Koudelka, Š.; Raška, M., Lipid-based nanoparticles and microbubbles–multifunctional lipid-based biocompatible particles for in vivo imaging and theranostics. Advances in Bioengineering 2015, 79-116.

[64] Tharkar, P.; Varanasi, R.; Wong, W. S. F.; Jin, C. T.; Chrzanowski, W., Nano-enhanced drug delivery and therapeutic ultrasound for cancer treatment and beyond. Frontiers in Bioengineering and Biotechnology 2019, 324.

[65] Hernot, S.; Klibanov, A. L., Microbubbles in ultrasound-triggered drug and gene delivery. Advanced drug delivery reviews 2008, 60 (10), 1153-1166.

[66] PRENTICE, Paul, et al. Membrane disruption by optically controlled microbubble cavitation. Nature physics, 2005, 1.2: 107-110.

[67] Wang, S.; Guo, X.; Xiu, W.; Liu, Y.; Ren, L.; Xiao, H.; Yang, F.; Gao, Y.; Xu, C.; Wang, L., Accelerating thrombolysis using a precision and clot-penetrating drug delivery strategy by nanoparticle-shelled microbubbles. Science advances 2020, 6 (31), eaaz8204.

[68] Fu, J.; Li, T.; Zhu, Y.; Hao, Y., Ultrasound-activated oxygen and ROS generation nanosystem systematically modulates tumor microenvironment and sensitizes sonodynamic therapy for hypoxic solid tumors. Advanced Functional Materials 2019, 29 (51), 1906195.

[69] Duco, W.; Grosso, V.; Zaccari, D.; Soltermann, A. T., Generation of ROS mediated by mechanical waves (ultrasound) and its possible applications. Methods 2016, 109, 141-148.

[70] McHale, A. P.; Callan, J. F.; Nomikou, N.; Fowley, C.; Callan, B., Sonodynamic therapy: concept, mechanism and application to cancer treatment. Therapeutic Ultrasound 2016, 429-450.

[71] Tachibana, K.; Feril Jr, L. B.; Ikeda-Dantsuji, Y., Sonodynamic therapy. Ultrasonics 2008, 48 (4), 253-259.

[72] Rosenthal, I.; Sostaric, J. Z.; Riesz, P., Sonodynamic therapy—a review of the synergistic effects of drugs and ultrasound. Ultrasonics sonochemistry 2004, 11 (6), 349-363.

[73] Van der Paal, J.; Neyts, E. C.; Verlackt, C. C.; Bogaerts, A., Effect of lipid peroxidation on membrane permeability of cancer and normal cells subjected to oxidative stress. Chemical science 2016, 7 (1), 489-498.

[74] 1.Cheeseman, K., Mechanisms and effects of lipid peroxidation.

Molecular Aspects of Medicine 1993, 14 (3), 191-197.

[75] Farmer, E. E.; Mueller, M. J., ROS-mediated lipid peroxidation and RES-activated signaling. Annual review of plant biology 2013, 64, 429-450.

[76] Nissen, S. E.; Yock, P., Intravascular ultrasound: novel pathophysiological insights and current clinical applications. Circulation 2001, 103 (4), 604-616.

[77] Sigrist, R. M.; Liau, J.; El Kaffas, A.; Chammas, M. C.; Willmann, J. K., Ultrasound elastography: review of techniques and clinical applications. Theranostics 2017, 7 (5), 1303.

[78] Elhelf, I. S.; Albahar, H.; Shah, U.; Oto, A.; Cressman, E.; Almekkawy, M., High intensity focused ultrasound: the fundamentals, clinical applications and research trends. Diagnostic and interventional imaging 2018, 99 (6), 349-359.

[79] Tharkar, P.; Varanasi, R.; Wong, W. S. F.; Jin, C. T.; Chrzanowski, W., Nano-enhanced drug delivery and therapeutic ultrasound for cancer treatment and beyond. Frontiers in Bioengineering and Biotechnology 2019, 324.

Chapter 2
Organic Nanoparticles

Parts of this chapter apear in:

D Kim, SS Lee, H Moon, SY Park, and HJ Lee, Published in ***Pharmaceuticals.*** 2021,14.6

D Kim, SS Lee, WY Yoo, H Moon, A Cho, SY Park, YS Kim, HR Kim, and HJ Lee, Published in ***Pharmaceuticals***. 2020,13,235

D Kim, J Han, SY Park, H Kim, JH Park and HJ Lee, Published in ***Materials*** 2020, 13, 1099

D Kim, W Han, JH Chang and HJ Lee, Published in ***Pharmaceutics*** 2021, 13, 1636

2.1. PD-L1 Targeting Immune-Microbubble Complex

2.1.1. Introduction

The advent of cancer immunotherapy has shifted the cancer-treatment paradigm. Since the goal of immunotherapy is to empower the body's immune system to kill cancer cells [1], it practically does not involve toxic materials or surgery against body mechanisms, thereby minimizing side effects [2,3]. Among potential cancer immunotherapies, methods such as application of specific antibodies, improving antigen presentation, immune checkpoint blockade therapies, and therapies against the tumor microenvironment (TME) are currently being evaluated in clinical trials. Furthermore, combinations of such therapies to improve efficacy are also being evaluated [3,4,5,6,7].

Tumor cells utilize their physiological methods to evade immune response for their survival. On the surface of the tumor cells, programmed death ligand 1 (PD-L1) is normally upregulated, allowing them to interact with the programmed death 1 (PD-1) on the surface of the T cells that induce suppression of immune response upon the PD-L1/PD-1 binding. During this interaction, CD80 [8,9], a member of the immunoglobulin superfamily that provides important antigen-nonspecific costimulatory signals for maximum immune responses, is

also involved [10], recruiting the Src homology 2 domain-containing protein tyrosine family phosphatases (SHPs). The recruitment of SHPs cause TCR reverse mechanisms of phosphorylation signals so that T cells become incapable of releasing granzymes and perforins regardless of the recognition of the major histocompatibility complex (MHC) I [11]. These include stimulation of regulatory T cells, promotion of T cell apoptosis, and prevention of the activation of effector T cells [12].

Although the blockade of PD-L1 has shown some clinical promises, there are still issues that need to be addressed with this approach. First, therapeutic antibodies against the PD-L1 are rarely used alone because the therapeutic effects are not as significant [13,14]. As such, checkpoint inhibitors are often used in combination with chemotherapeutic agents to maximize the therapeutic potential [15,16,17], which can elicit potential chemo-related side effects [18]. Furthermore, despite the concept of boosting one's immune system, the application of PD-L1 inhibitors are not without side effects themselves [19]. An increasing amount of reports on the immune-related adverse effects (irAEs) and hypersensitivity are now becoming available [20]. It has been reported that approximately 10 to 20 percent of patients treated with PD-L1 inhibitors have shown irAEs [21,22]. In addition, instances of fetal hypersensitivity have also been reported upon the administration of PD-L1 monoclonal antibodies into

preclinical animal models, inducing irreversible damage and death [23]. As such, there is a strong need for the development of agents and/or methods that can minimize the xenogeneic toxicities while maximizing therapeutic efficacy to be met.

The combination of checkpoint inhibitors with focused ultrasound (FUS) is being actively investigated to complement cancer immunotherapy [23,24]. High-intensity FUS, either by itself or in combination with microbubbles, has been used to ablate local tumors by generating thermal effects at the focal region [23]. In addition, the FUS-mediated mechanical fractionation of tumors physically alters the tumor microenvironment, enhancing the release of chemokines or cytokines from the tumors which leads to priming of the dendritic cells against the released tumor antigens and also increased infiltration of immune cells into the system [25,26,27]. To the added benefit, ultrasound-assisted cavitation of microbubbles can temporarily increase the size of vascular fenestrations, allowing enhanced extravasation of therapeutic agents into the interstitial space for desired effects [28,29].

To capitalize on these features and to circumvent irAEs, we have developed a new type of microbubble (MB) delivery system called the immune-microbubble complex (IMC), in which phospholipid microbubbles are covalently labeled with PD-L1 antibodies. This way,

the targeting and therapeutic efficacy of PD-L1 are maintained, while the potential immunogenic responses are alleviated by making it difficult for the immune cells to recognize the antibody through polyethylene glycol "stealth" mechanisms and partial blockage of the Fc region due to the antibody-MB conjugation. Besides, the application of ultrasound will ensure that (1) targeted tumors are partially/fully fragmented by mechanical forces to improve antigen presentation, (2) cavitation by the IMCs themselves will enhance extravasation into the tumor region, and (3) only upon the ultrasound exposure will the MB "burst open", allowing the antibodies to become free and interact with their receptors. In this paper, we were able to minimize antibody-related fatalities in the mice cohorts and maximized PD-L1 monotherapy using the combination of IMC and therapeutic ultrasound.

2.1.2. Materials and Methods

2.1.2.1. Preparation of the Lipid Microbubbles

Microbubbles (MB) were synthesized based on the phospholipid thin-film hydration method. 1,2-distearoyl-sn-glycero-3-phosphocholine(DSPC) and 1,2-distearoyl-sn-glycero-3-phospho-ethanolamine-N-[succinyl(polyethylene glycol)-2000] (DSPE-PEG2k-NHS, both purchased from Avanti Polar Lipids, Alabaster, AL, USA) were dissolved in chloroform at 9:1 6:4, 3:7, 7:3, and 5:5 molar ratios.

Subsequently, chloroform was evaporated with a rotary evaporator (to form a thin phospholipid film). This phospholipid film at a concentration of 0.5 mg/mL was hydrated using 0.01M PBS over the phase transition temperature of DSPC and was dispersed using a bath sonicator. Once completely dissolved, the headspace of empty vials was filled with sulfur hexafluoride gas (SF6) for 45 seconds, capped, and was agitated by VialmixTM (Definity, North Billerica, MA, USA) for 45 seconds to generate MBs. MBs were manually counted under a light microscope to approximate their number.

2.1.2.2. Preparation and Characterization of the IMC

To conjugate microbubbles with antibodies, 1.5×10^9 microbubbles were mixed with 20, 40, 80, 100, and 200 μg of the anti-PD-L1 antibody (BioXcell, Lebanon, NH, USA) for 30 min at room temperature. The unreacted anti-PD-L1 antibody was separated from the IMC by gradient centrifugation at 3000 rpm for 10 min. To confirm the antibody conjugation on the microbubbles, 1 mg of FITC-tagged IgG antibodies were incubated with as-prepared IMC for 60 min at 4 °C. The secondary antibody-conjugated IMC solution was purified by centrifugation for 5 min at 3000 rpm. The supernatant was collected, and the amount of unreacted antibody was measured using the Bradford assay (Thermo Fisher Scientific, Waltham, MA, USA) under the manufacturer's

guidelines. The size distribution and zeta potential of the microbubbles and IMC were measured using a Malvern Zetasizer Nano (Malvern Instrument Ltd., Worcestershire, UK).

2.1.2.3. Stability Test of MB and IMC

Microbubbles with different molar ratios of DSPC and DSPE-PEG2K-NHS (9:1, 6:4, 3:7, 7:3, and 5:5, respectively) were used to optimize their stability. After their synthesis, the microbubbles and IMC with different phospholipid ratios were diluted 100-fold with PBS and were counted manually under a light microscope. Measurements were made at 0, 3, 6, and 24 h post microbubble synthesis.

Once the optimal phospholipid ratio for microbubble synthesis was obtained, the long-term stability of prepared microbubbles and the IMC were evaluated by monitoring them for up to 7 days at room temperature and 4 °C. The number of microbubbles and IMC were counted every 24 h manually under the light microscope.

2.1.2.4. Confocal Imaging

For confocal microscope imaging, the IMC was conjugated with FITC-tagged antibody by adding 50 μg of the antibody to 1 mg/mL of IMC solution and incubating the mixture on a shaker for an hour at room temperature. Subsequently, the IMC-FITC antibody conjugate was centrifuged at 3000 rpm for 5 min to remove unbound antibodies and the

samples were placed on a glass slide for microscopy. The fluorescent images of the IMC were obtained using LSM710 (Zeiss, Germany) at a magnification of 1000×, using excitation and emission filters at 490/520 nm, respectively.

2.1.2.5. Animal Studies

All in vivo protocols were verified according to the guidelines of the Seoul National University Bundang Hospital (Approval Number BA1811-260/079-01). 6- to 8-week-old immunocompetent and immunodeficient female BALB/c nude mice were purchased from Orient Bio (Seoul, Korea) for toxicity and efficacy studies, respectively. The mice were acclimatized for a week before the start of the respective experiments and were maintained at standard conditions in specific pathogen-free (SPF) environments: 25 ± 2 °C temperature, 50 ± 10% relative humidity, and 12h light/12h dark cycle. All mice were fed with sterilized standard mouse chow and water ad libitum.

The experimental groups for the acute toxicity study were designated as follows: (i) PD-L1 antibody (100 μg/intraperitoneal (IP) injection), (ii) PD-L1 antibody (200 μg/IP), (iii) PD-L1 antibody (100 μg/intravenous (IV) injection), (iv) PD-L1 antibody (200 μg/IV), (v) IMC (100 μg/IV), and (vi) IMC (200 μg/IV). Each group received a single bolus injection of 200 μL of the treatment protocols every three days, five times. The

conditions and weights of mice were monitored for 15 days following the injection.

For the efficacy studies, 1×10^6 of CT26-wt cells suspended in Matrigel (Corning, MA, USA) were injected into the right flank region of the nude mice. Tumor sizes were monitored bi-weekly with a digital caliper and the volumes were calculated using the modified ellipsoid formula: $\text{width}^2 \times \text{length} \times 0.5$. Once the tumor volume reached to 50~70 mm^3, the mice were randomly sorted for treatment. The experimental groups were defined as follows: (i) Isotype control, (ii) anti-PD-L1 antibody (200 μg antibody concentration), (iii) IMC (200 μg), (iv) FUS only, (v) anti-PD-L1 antibody (200 μg) + FUS, and (vi) IMC (200 μg) + FUS (n = 5 per group). Each group received treatments every three days, three times. A pre-clinical FUS system (VIFU 2000®, Alpinion Medical Systems, Seoul, Korea) was used for all ultrasound treatments, with the treatment protocols adapted from our previous work [41]. For this study, the FUS conditions were the following: 1.1 MHz frequency, 100 Watts, 100 Hz pulse repetition frequency, 5% duty cycle, 5 s ultrasound exposure per spot, and 2 mm spot distance. The mice were monitored for a week following their respective treatments, and their weights were also recorded at days 0, 3, 6, 9, 12, and 15.

2.1.2.6. Preparation of Immunohistochemistry

24 h after respective treatments, tumors were excised and first fixed in 5 L of formalin for 44 min. Subsequently, they were placed in an ethyl alcohol solution for 30 min before being transferred onto another ethyl alcohol solution at a higher concentration. This transfer was repeated 6 times. Following ethyl alcohol fixation, the samples were then placed in xylene solution at a low concentration for 45 min before being transferred onto another xylene solution at a higher concentration for a total of three times. Finally, the samples were then embedded in paraffin wax. The sample processing was performed using Leica Peloris (Buffalo Grove, IL, USA). The embedded tumor samples were cut into 3 μm slices with Leica RM2235 (Buffalo Grove, IL, USA) and incubated in hydrogen peroxide blocks for 10 min. The tumor-bound PD-L1 antibodies were then detected using the UltraVision LP Large Volume Detection System (Thermo Fisher, San Jose, CA, USA) according to the manufacturer's guidelines.

2.1.3. Results

2.1.3.1. Characterization of MBs and IMC

The MBs and IMCs were synthesized based on the phospholipid thin-film hydration method. To maximize the yield and stability of MB, we first examined combinations of different phospholipid molecules at

various molar ratios (Figure 1). Based on the experimental data, we found that the 9:1 1,2-distearoyl-sn-glycero-3-phosphocholine(DSPC) to 2-distearoyl-sn-glycero-3-phospho-ethanol-amine-N-[succinyl(polyethylene glycol)-2000] (DSPE-PEG2K-NHS) molar ratio resulted in the maximum MB production. The yield for the 9:1 ratio was $1.05^{5} \times 10^{10}$ MBs, while $8.3^{5} \times 10^{9}$, $6.0^{1} \times 10^{9}$, $1.5^{1} \times 10^{9}$, and 2.1×10^{8} MBs were formed for 7:3, 6:4, 5:5, and 3:7 molar ratios of DSPC to DSPE-PEG2K-NHS, respectively. Furthermore, the 24hr stability was highest for the 9:1 ratio as well, with $3.5^{2} \times 10^{9}$ MBs remaining after 24 hr compared to 7:3, 6:4, 5:5, and 3:7 ratios that had 2.8×10^{8}, 3.2×10^{7}, 2.9×10^{5}, and 2.1×10^{5} MBs remaining, respectively. As such, the 9:1 molar ratio of DSPC to DSPE-PEG2K-NHS was used throughout this study. Using the dynamic light scattering techniques, the average size of the MBs at the 9:1 DSPC:DSPE-PEG2K-NHS ratio was measured to be 1.19 ± 0.245 μm, with the zeta potential of -3 ± 1.21 mV.

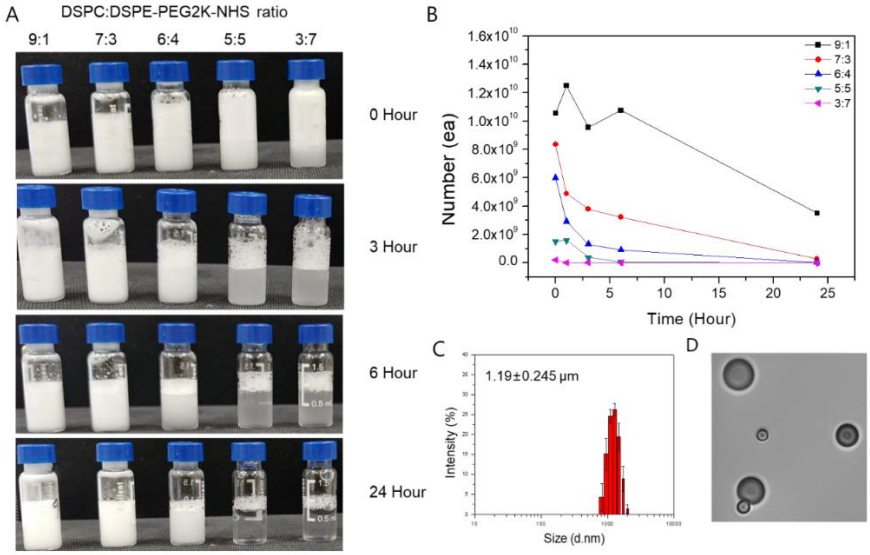

Figure 2.1.1. The yield, size, and stability of microbubbles (MBs) with different molar ratios of the phospholipids. (A) Synthesized MBs with various molar ratios of DSPC:DSPE-PEG2K-NHS. MBs with a higher DSPC ratio retain their structure for up to 24 hr, while a higher ratio of DSPE-PEG2K leads to MB instability. (B) MBs were counted under the light microscope. Similar to the visual inspection, MBs with 9:1 DSPC:DSPE-PEG2K ratio had the highest count at the time of synthesis and 24 hr post-synthesis. (C) The average size of the synthesized MBs with 9:1 DSPC:DSPE-PEG2K ratio was 1.19 ± 0.245 μm. (D) A picture of the MBs was taken under the light microscope.

Next, to produce IMC, the PD-L1 antibodies were conjugated onto MBs by exploiting the NHS functional group on the MB surface. The average size of IMCs was 1.06 ± 0.312 μm with zeta potential values of −2 ± 0.75 mV, suggesting that the synthesized IMCs have comparable physical characteristics to the parent MBs. The conjugation efficiency was also evaluated using the Bradford assay by calculating the number of antibodies that remain in the supernatant post conjugation. Because 100-fold molar excess of NHS was present, the conjugation efficiency of antibodies was near 100%. The stability of IMC after antibody conjugation was then evaluated. At 4 °C, both the MBs and IMCs remained relatively stable, with over 70% of them remaining intact after three days (Figure 2). Up to 50% of the initial amount of MBs and IMCs remained viable after 200 hr as well, suggesting the structural stability at lower temperatures. However, the stability of both MBs and IMCs had decreased dramatically at room temperature, with only 50% of MBs and IMCs remaining intact after 40 h, and close to none after 72 h.

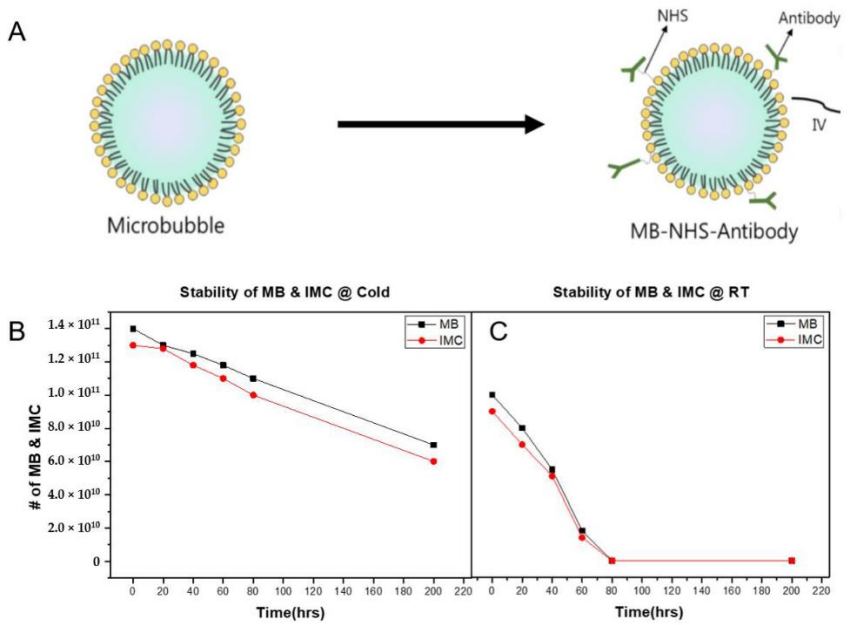

Figure 2.1.2. Synthesis of the immune-microbubble complex (IMC) and their stability. (A) The schematics of conjugating antibodies onto the surface of MBs using amine-NHS crosslinking. (B) The stability of the MBs and IMCs at 4 °C over 200 h. For both MBs and IMCs, up to 50% of the initial amount remained viable. (C) The stability of the MBs and IMCs decreased significantly at room temperature conditions, suggesting that higher temperature was associated with their decay.

2.1.3.2. Confocal Image of IMC

To confirm the antibody conjugation and visualize the IMCs, fluorescein isothiocyanate (FITC)-conjugated antibodies were conjugated onto the surface of MBs, similar to the protocol for conjugation of the anti-PD-L1 antibody. The fluorescence-labeled antibody-MB complex was examined with an LSM710 confocal microscope at ×1000 magnification. A strong FITC fluorescence, corresponding to the borders of the MBs in differential interference contrast images, was observed, confirming that the antibodies could be successfully conjugated onto the surface of the MBs (Figure 2.1.3).

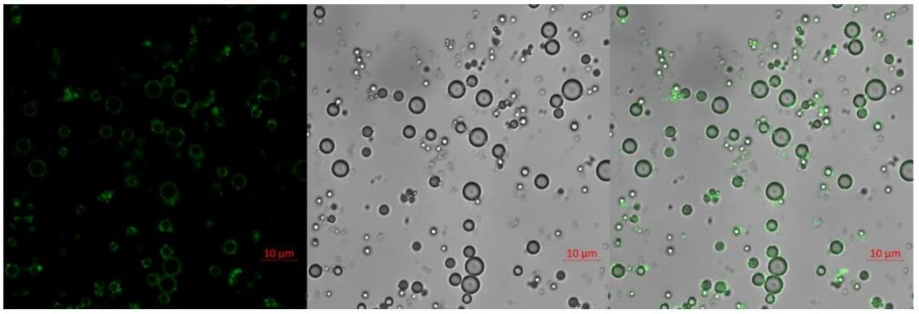

Figure 2.1.3. Confocal images of FITC-labeled IMC. Scale bar: 10 µm.

2.1.3.3. Improved Toxicological Profiles of IMC over the PD-L1 Antibodies In Vivo

According to the report from Mall et al. [23], repeated administration of PD-L1 monoclonal antibodies induced severe hypersensitivity reactions in orthotopic 4T1 murine mammary carcinoma models. During our experiments, we also discovered that injecting high doses of xenogeneic PD-L1 antibodies in BALB/c mice carrying subcutaneous CT26 carcinoma led to unexpected deaths. We hypothesized that these sudden, unexpected deaths were potentially associated with irAEs, and first tried to establish whether the administration of antibodies were indeed the cause of the mortalities. We prepared two cohorts of mice, one bearing CT26 colon carcinoma and the other not. We have also compared two different routes of administration commonly observed in drug treatment, intraperitoneal (IP) and intravenous (IV). Two doses (100 and 200μg of antibodies per injection, equivalent to approximately 4 and 8 mg/kg) were administered in bolus every three days, five times. It was observed that the cohort without tumors had a higher overall survival rate than those with tumors (44/60 for tumor-bearing cohort vs 56/60 for the control group at day 15) (Figure 2.1.4). Unsurprisingly, the IV route had a lower survival rate than the IP route as 26/40 mice survived the treatment regimen by day 15 in the IV and 37/40 in the IP group. We

speculated that because the direct entry into the circulation from the IV route has higher bioavailability than the IP route, a rapid systemic immune response against the xenogeneic antibody can be triggered, causing sudden deaths. Furthermore, similar to Mall et al.'s speculations, the high inflammatory nature of certain tumors induces accumulation of immune cells, thereby promoting a strong immune response against the PD-L1 antibody.

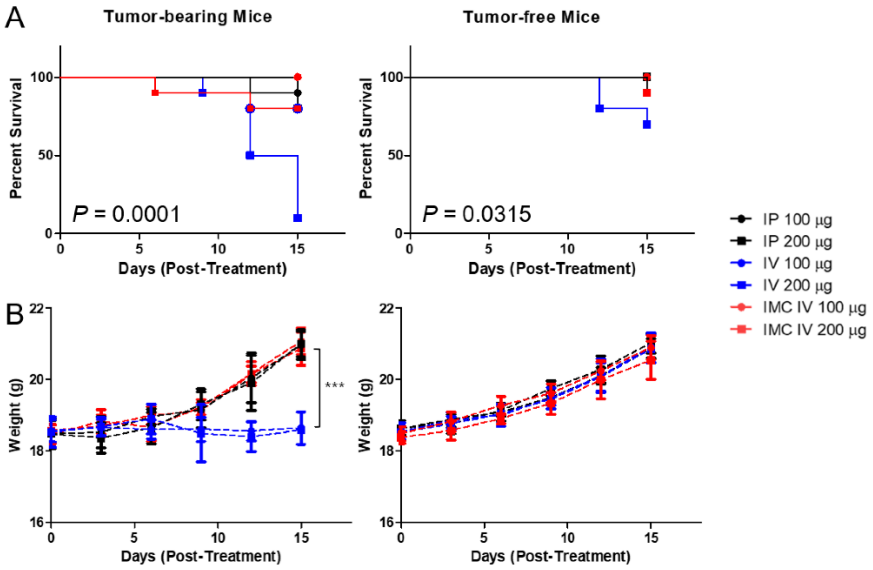

Figure 2.1.4. The survival analysis of anti-PD-L1 antibody administered CT26-wt tumor-bearing mice and the evaluation of the effects of the dose and different routes of administration. (A) The intravenous injection of PD-L1 antibodies at higher doses (200 µg) in tumor-bearing and tumor-free mice showed increased adverse effects, as 90% and 30% of the mice died within two weeks after injection, respectively. (B) The tumor-bearing mice that were injected with the PD-L1 antibodies intravenously at both high and low doses showed reduced weight gain, which may suggest potential adverse effects induced by these antibodies. All the other mice in both the tumor-bearing and tumor-free groups showed a steady increase in the average body weight over the two weeks. IP—intraperitoneal injection; IV—intravenous injection; Values are mean ± SD (n = 10 per group). *** $p \leq 0.001$.

To overcome the irAEs, we have designed IMC, in which PD-L1 antibodies are conjugated onto microbubbles to enhance circulation and to alleviate problems related to toxicity. Polyethylene glycol chains on the MB surface provides the “stealth” mechanism, further preventing the macrophages from recognizing and mustering an immune response against them. When the IMCs were administered intravenously into the mice cohorts at the same concentrations, the toxicities of the antibodies decreased dramatically, as 18/20 (10/10 for 100 μg and 8/10 for 200 μg injected group) of the tumor-bearing and 19/20 of the control mice (10/10 for 100 μg and 9/10 for 200 μg injected group) survived the repeated dose schedules without noticeable signs or symptoms, compared to the cohorts receiving the unmodified PD-L1 antibodies, with survival rates of 9/20 (8/10 for 100 μg and 1/10 for 200 μg) for the tumor-bearing and 17/20 (10/10 for 100 μg and 7/10 for 200 μg) for the control group (n = 10 per group). This pattern was evident in the weight changes of the mice as well. For the groups that received the PD-L1 antibody intraperitoneally or IMC through the IV route, their body weights gradually increased over the 15 days regardless of tumor-bearing or not. Nevertheless, the mice bearing tumors that had received intravenous injections of the PD-L1 not only had higher mortality but also a significant decrease in the weight gains as well. Based on the

experimental data, the survival rate was lowest in the tumor-bearing mice that received PD-L1 antibodies intravenously, while those receiving IMCs had significantly improved.

2.1.3.4. Inhibition of Tumor Growth by the IMC-FUS Combination Therapy

Next, the therapeutic efficacy of the PD-L1 antibody was evaluated. To determine the appropriate dosing schedule and the route of administration, CT26-wt colorectal cancer mouse models were prepared. Different amounts of the PD-L1 antibodies (200 and 100 μg) as well as the route of administration (IP vs IV) were compared. Based on the preliminary data, we found that 200 μg of antibodies injected intravenously had the strongest tumor suppression (data not shown). Furthermore, because five complete treatments over fifteen days were lethal to the tumor-bearing mice receiving intravenous anti-PD-L1 antibody injections, we have hypothesized that the mice would only be able to tolerate up to three treatments without showing significant weight changes based upon the survival analysis. Based on these premises, we prepared another set of CT26 tumor-bearing mice to evaluate the therapeutic efficacy of the combinatorial therapy using FUS and IMC (Figure 2.1.5). A total of six experimental groups were prepared: (i) the negative control group injected with saline, (ii) US only, (iii) PD-L1

antibody only, (iv) IMC only, (v) PD-L1 antibody + FUS, and (vi) IMC + FUS. There was no statistical difference between the tumor volumes of the control group, US-treated group, and those that received IMC only (890.1 ± 116.7, 827.5 ± 124.7, and 732.5 ± 64.2 mm^3, respectively). The PD-L1 antibodies were somewhat effective in retarding the tumor growth (556.5 ± 74.6 mm^3) when compared to the control group. Maximum therapeutic efficacy was observed for the groups that received a combination of PD-L1 antibody (480.5 ± 58.1 mm^3) or IMC with FUS treatment (309.7 ± 56.4 mm^3). The latter was especially efficient in suppressing the tumor growth as the IMC-FUS combination treatments were significantly better than the combination of PD-L1 antibody with FUS.

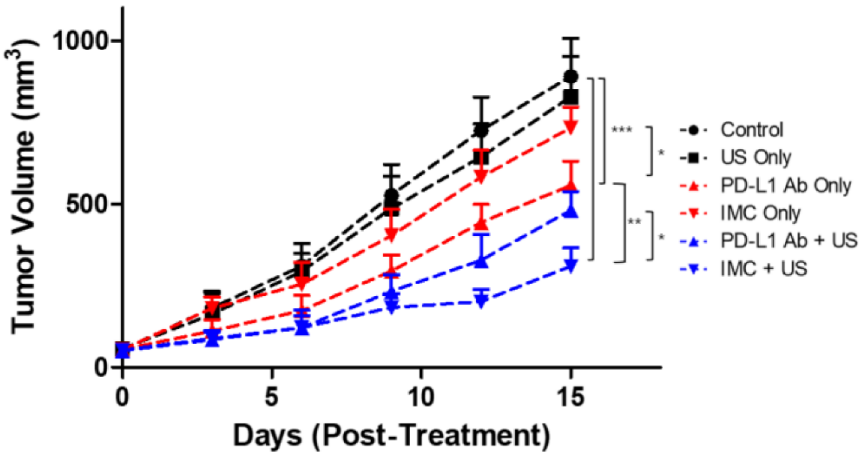

Figure 2.1.5. The therapeutic efficacy of PD-L1 targeting protocols against CT26 colon tumors. The control, ultrasound (US) only, and IMC only groups did not show any regression of the tumor after treatment protocols were employed. As expected, the administration of PD-L1 antibody was effective in retarding the tumor growth. The therapeutic effects were maximized with the combination of IMC with focused ultrasound treatment, from which the synergistic effects of both the enhanced localization of the PD-L1 antibody and the cavitation induced by the focused ultrasound can be expected. Values are mean $\pm$ SD (n = 5). * p $\leq$ 0.05, ** p $\leq$ 0.01, *** p $\leq$ 0.001.

2.1.3.5. Immunohistochemical Staining of the Tumor Confirms Enhanced Localization of PD-L1 Antibodies

The localization of the PD-L1 antibodies at the tumor site upon the different treatment protocols were evaluated with immunohistochemistry methods. Similar to the efficacy studies, a total of six experimental groups were prepared: (i) negative control receiving an intravenous injection of the generic IgG antibody, (ii) PD-L1 antibody, (iii) FUS only, (iv) IMC only, (v) PD-L1 antibody + FUS, and (vi) IMC + FUS. 24 h after each cohort received their respective treatment protocols, the mice were euthanized, and the tumors were collected for immunohistochemical staining. An enhanced localization of the PD-L1 antibody was observed in the group that had received IMC and was treated with FUS protocols (Figure 2.1.6), while the other groups showed relatively lower levels of the PD-L1 antibody bound onto the tumor surface.

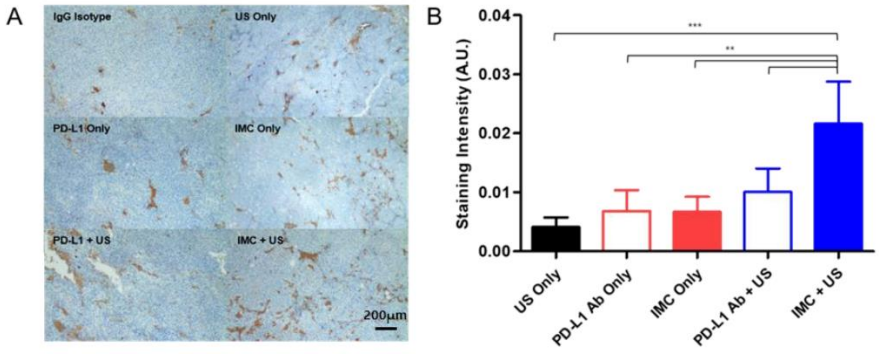

Figure 2.1.6. Immunohistochemical evaluation of PD-L1 antibody in different treatment groups. (A) Representative pictures for each treatment group after PD-L1 antibody staining are presented. (B) The intensity of PD-L1 antibody staining from these pictures were analyzed using ImageJ. The staining intensity of the IgG isotype was subtracted from each group to account for the non-specific binding and background signals. Values are mean ± SD (n = minimum 3 for each group). ** $p \leq 0.01$, *** $p \leq 0.001$.

2.1.4. Discussion

As third-generation cancer therapeutic agents, immune checkpoint inhibitors that are involved in T-cell regulation such as PD-L1 antibodies have been successfully validated in preclinical models and are currently used in clinical settings against different types of cancers. To reduce the immunogenicity, therapeutic antibodies in clinical applications are humanized to remove the potential immunological responses [30]. Nevertheless, despite the efforts to minimize the toxicity, humanized monoclonal antibodies may still induce potential and serious adverse immune-related complications [31,32]. We observed similar immunogenic responses as we were developing a syngeneic mouse model bearing CT26 colon cancer cells to evaluate immune checkpoint inhibitor therapies using rat-derived anti-mouse PD-L1 antibodies.

Dose-limiting toxicities remain as one of the biggest challenges associated with drug delivery regardless of the type of molecule being used [33,34]. As Mall et al. reported, repeated intraperitoneal injections of the PD-L1 antibodies to the mice bearing orthotopic 4T1 murine mammary carcinoma induced fatal hypersensitivity reactions [23]. Our experimental data also showed that higher doses of antibody injection induced fatality regardless of the route of administration (Figure 2.1.4). When the repeated dose was increased to 400 μg per injection, the

fraction of mice surviving decreased even more (survival of 8/10 for those injected with 200 μg antibody → 7/10 for those injected with 400 μg antibody in the tumor-bearing mice cohort, $p = 0.6004$ and 10/10 for mice for those injected with 200 μg antibody → 8/10 for those injected with 400 μg antibody in the tumor-free mice cohort, $p = 0.146$; data not shown). The intravenous injections of the PD-L1 antibodies were even more lethal, as 9/10 of the tumor-bearing mice receiving 200 μg antibody per injection had died within two weeks after injection, with significant reductions in weight gains.

To alleviate the associated adverse effects, the presentation of active pharmaceutical ingredients in carriers such as liposomes has become a standard practice to enhance the pharmacokinetic/dynamic profiles in vivo. Doxil (liposomal doxorubicin) and Abraxane (albumin-bound paclitaxel) are two examples of such nanoformulations used in clinics that have greatly increased the therapeutic index of the parent drugs by extending their circulatory half-life and reducing the associated immunotoxicities [35,36,37]. As such, we hypothesized that by presenting the therapeutic PD-L1 antibodies in a nanoformulation, we could expect similar improvements in the therapeutic index and avoid the immune adverse effects. IMCs have not only met these criteria to minimize adverse effects, but they also introduce an additional

dimension to improve the therapeutic efficacy—the concept of cavitation-mediated drug delivery.

During the last decade, the use of ultrasound with MBs to enhance local drug delivery has been well-studied in the preclinical and clinical settings [38,39] against brain diseases [40], breast cancer [41], and pancreatic cancer [42]. At the focal point, the converged ultrasound beams cause cavitation of the injected MBs, which temporarily disrupt the endothelial linings and increase drug extravasation into the interstitial space for enhanced therapeutic effects [39]. Likewise, when IMCs were combined with the ultrasound treatment against CT26 tumors, the anti-cancer effects were maximized (Figure 2.1.5). On the other hand, IMCs by themselves did not have strong anti-cancer effects as the tumor growth was comparable to that of the PBS-injected (control) group, suggesting that an additional trigger is essential for the IMCs to become effective. Based on experimental evidence, we propose the following mechanism of action for IMCs and the IMC + FUS combination therapy (Figure 2.1.7): (1) IMCs, unlike the parent PD-L1 antibody, is PEGylated and much larger in size, which enhances their half-life and prevents potential immune responses. (2) IMCs are stable at room temperature for at least 24 h (Figure 2.1.2), so their structure would remain relatively intact in circulation and prevent the conjugated PD-L1 antibody from binding

onto the PD-L1 expressed on the surface of CT26 tumors. (3) Upon the focused ultrasound treatment, IMCs undergo cavitation to increase extravasation, and eventually break down to expose the individual antibodies which then bind to the surface of PD-L1-expressing tumors. Subsequently, CD8 + T cells can recognize and remove the tumor cells.

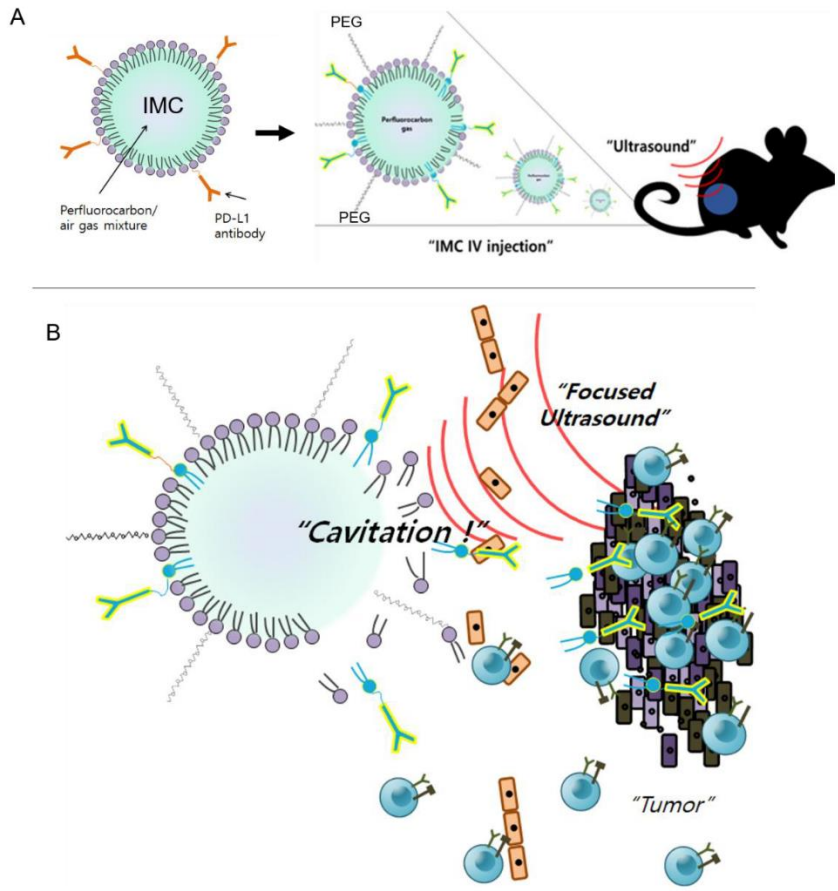

Figure 2.1.7. The proposed mechanism of action for IMC and the combination therapy. (A) IMCs are injected intravenously into the tumor-bearing mice. Because they are PEGylated and larger in size, they are less likely to induce immune responses compared to the individual antibodies. (B) IMCs are stimulated with ultrasound, which causes acoustic cavitation as well as their breakdown, allowing the PD-L1 antibodies to better access the tumor. The blocking of the surface PD-L1 on the tumors allows cytotoxic T cells to recognize the tumor cells and destroy them.

The role of FUS in the tumor microenvironment remains to be elucidated for this study. FUS treatment, by itself or in combination with MBs, causes mechanical fractionation of the tumor tissues at the focal point and triggers the release of tumor antigens to the microenvironment [43]. Enhanced tumor antigen release potentiates dendritic cell maturation, which in turn triggers priming of the T cells and immunological responses against the tumor cells [44,45]. While we speculate that similar mechanisms are responsible for the results obtained in this study, we were not able to validate the results with immunological evaluations. In the near future, we plan to follow up on this study by confirming the changes in cytokine expressions, T cell infiltrations, as well as potential tumor rechallenged experiments.

2.1.5. Conclusion

In this work, PD-L1 antibody-conjugated microbubbles—termed IMCs—were used in combination with focused ultrasound to treat CT26-wt tumor-bearing colon cancer mouse models. Not only were the IMCs able to alleviate adverse immune responses and fatalities associated with systemic administration of xenogeneic antibodies, but they also enhanced therapeutic efficacy when combined with ultrasound treatment. While the exact immunomodulatory mechanisms remain to be validated, the development of IMCs can serve as a unique way to improve the

therapeutic index for antibodies used in clinics today.

References

[1] Disis, M. L. In Mechanism of action of immunotherapy, Seminars in oncology, Elsevier: 2014; pp S3-S13.

[2] O'Donnell, J. S.; Hoefsmit, E. P.; Smyth, M. J.; Blank, C. U.; Teng, M. W., The promise of neoadjuvant immunotherapy and surgery for cancer treatment. Clinical Cancer Research 2019, 25 (19), 5743-5751.

[3] Couzin-Frankel, J., Breakthrough of the year 2013. Cancer Immunother Sci 2013, 342 (6165), 1432-1433.

[4] Chowdhury, P.; Chamoto, K.; Honjo, T., Combination therapy strategies for improving PD-1 blockade efficacy: a new era in cancer immunotherapy. Journal of internal medicine 2018, 283 (2), 110-120.

[5] Kim, D.; Lee, S. S.; Moon, H.; Park, S. Y.; Lee, H. J., PD-L1 Targeting Immune-Microbubble Complex Enhances Therapeutic Index in Murine Colon Cancer Models. Pharmaceuticals 2020, 14 (1), 6.

[6] Devaud, C.; John, L. B.; Westwood, J. A.; Darcy, P. K.; Kershaw, M. H., Immune modulation of the tumor microenvironment for enhancing cancer immunotherapy. Oncoimmunology 2013, 2 (8), e25961.

[7] Nam, J.; Son, S.; Park, K. S.; Zou, W.; Shea, L. D.; Moon, J. J., Cancer nanomedicine for combination cancer immunotherapy. Nature Reviews Materials 2019, 4 (6), 398-414.

[8] Peach, R. J.; Bajorath, J.; Naemura, J.; Leytze, G.; Greene, J.; Aruffo, A.; Linsley, P. S., Both Extracellular Immunoglobin-like Domains of CD80 Contain Residues Critical for Binding T Cell Surface Receptors CTLA-4 and CD28 (*). Journal of Biological Chemistry 1995, 270 (36), 21181-21187.

[9] Chen, D. S.; Mellman, I., Oncology meets immunology: the cancer-immunity cycle. immunity 2013, 39 (1), 1-10.

[10] Xu, C.; Zhang, Y.; Rolfe, P. A.; Hernández, V. M.; Guzman, W.; Kradjian, G.; Marelli, B.; Qin, G.; Qi, J.; Wang, H., Combination therapy with NHS-muIL12 and avelumab (anti-PD-L1) enhances antitumor efficacy in preclinical cancer models. Clinical Cancer Research 2017, 23 (19), 5869-5880.

[11] Ribas, A., Releasing the brakes on cancer immunotherapy. N Engl J Med 2015, 373 (16), 1490-1492.

[12] Ostrand-Rosenberg, S.; Horn, L. A.; Haile, S. T., The programmed death-1 immune-suppressive pathway: barrier to antitumor immunity. The Journal of Immunology 2014, 193 (8), 3835-3841.

[13] Song, W.; Shen, L.; Wang, Y.; Liu, Q.; Goodwin, T. J.; Li, J.; Dorosheva, O.; Liu, T.; Liu, R.; Huang, L., Synergistic and low adverse effect cancer immunotherapy by immunogenic chemotherapy and locally expressed PD-L1 trap. Nature communications 2018, 9 (1), 1-11.

[14] Feng, M.; Xiong, G.; Cao, Z.; Yang, G.; Zheng, S.; Song, X.; You, L.; Zheng, L.; Zhang, T.; Zhao, Y., PD-1/PD-L1 and immunotherapy for pancreatic cancer. Cancer letters 2017, 407, 57-65.

[15] LaRocca, C. J.; Warner, S. G., Oncolytic viruses and checkpoint inhibitors: combination therapy in clinical trials. Clinical and translational medicine 2018, 7 (1), 1-13.

[16] Patel, S. A.; Minn, A. J., Combination cancer therapy with immune checkpoint blockade: mechanisms and strategies. Immunity 2018, 48 (3), 417-433..

[17] Tang, J.; Yu, J. X.; Hubbard-Lucey, V. M.; Neftelinov, S. T.; Hodge, J. P.; Lin, Y., Trial watch: the clinical trial landscape for PD1/PDL1 immune checkpoint inhibitors. Nature reviews Drug discovery 2018, 17 (12), 854-856.

[18] Lindley, C.; McCune, J. S.; Thomason, T. E.; Lauder, D.; Sauls, A.; Adkins, S.; Sawyer, W. T., Perception of chemotherapy side effects cancer versus noncancer patients. Cancer practice 1999, 7 (2), 59-65.

[19] Scotté, F.; Ratta, R.; Beuzeboc, P., Side effects of immunotherapy: a constant challenge for oncologists. Current Opinion in Oncology 2019, 31 (4), 280-285.

[20] Macy, E., Immune-related adverse drug reactions and immunologically mediated drug hypersensitivity. Immunology and Allergy Clinics 2020, 40 (4), 635-647.

[21] Brahmer, J. R.; Lacchetti, C.; Schneider, B. J.; Atkins, M. B.; Brassil, K. J.; Caterino, J. M.; Chau, I.; Ernstoff, M. S.; Gardner, J. M.; Ginex, P., Management of immune-related adverse events in patients treated with immune checkpoint inhibitor therapy: American Society of Clinical Oncology Clinical Practice Guideline. Journal of clinical oncology: official journal of the American Society of Clinical Oncology 2018, 36 (17), 1714.

[22] Baldo, B., Adverse events to monoclonal antibodies used for cancer therapy: focus on hypersensitivity responses. Oncoimmunology 2013, 2 (10), e26333.

[23] Kim, D.; Lee, S. S.; Moon, H.; Park, S. Y.; Lee, H. J., PD-L1 Targeting Immune-Microbubble Complex Enhances Therapeutic Index in Murine Colon Cancer Models. Pharmaceuticals 2020, 14 (1), 6.

[24] Wu, F.; Wang, Z.-B.; Lu, P.; Xu, Z.-L.; Chen, W.-Z.; Zhu, H.; Jin, C.-B., Activated anti-tumor immunity in cancer patients after high intensity focused ultrasound ablation. Ultrasound in medicine & biology 2004, 30 (9), 1217-1222.

[25] Wu, F., High intensity focused ultrasound ablation and antitumor immune response. The Journal of the Acoustical Society of America 2013, 134 (2), 1695-1701..

[26] Curley, C. T.; Stevens, A. D.; Mathew, A. S.; Stasiak, K.; Garrison, W. J.; Miller, G. W.; Sheybani, N. D.; Engelhard, V. H.; Bullock, T. N.; Price, R. J., Immunomodulation of intracranial melanoma in response to blood-tumor barrier opening with focused ultrasound. Theranostics 2020, 10 (19), 8821.

[27] Liu, F.; Hu, Z.; Qiu, L.; Hui, C.; Li, C.; Zhong, P.; Zhang, J., Boosting high-intensity focused ultrasound-induced anti-tumor immunity using a sparse-scan strategy that can more effectively promote dendritic cell maturation. Journal of translational medicine 2010, 8 (1), 1-12.

[28] Lin, C.-Y.; Liu, T.-M.; Chen, C.-Y.; Huang, Y.-L.; Huang, W.-K.; Sun, C.-K.; Chang, F.-H.; Lin, W.-L., Quantitative and qualitative investigation into the impact of focused ultrasound with microbubbles on the triggered release of nanoparticles from vasculature in mouse tumors. Journal of Controlled Release 2010, 146 (3), 291-298.

[29] Gao, Y.; Gao, S.; Zhao, B.; Zhao, Y.; Hua, X.; Tan, K.; Liu, Z., Vascular effects of microbubble-enhanced, pulsed, focused ultrasound on liver blood perfusion. Ultrasound in medicine & biology 2012, 38 (1), 91-98.

[30] Stern, M.; Herrmann, R., Overview of monoclonal antibodies in

cancer therapy: present and promise. Critical reviews in oncology/hematology 2005, 54 (1), 11-29.

[31] Brennan, F. R.; Morton, L. D.; Spindeldreher, S.; Kiessling, A.; Allenspach, R.; Hey, A.; Müller, P.; Frings, W.; Sims, J. In Safety and immunotoxicity assessment of immunomodulatory monoclonal antibodies, MAbs, Taylor & Francis: 2010; pp 233-255.

[32] Harding, F. A.; Stickler, M. M.; Razo, J.; DuBridge, R. In The immunogenicity of humanized and fully human antibodies: residual immunogenicity resides in the CDR regions, MAbs, Taylor & Francis: 2010; pp 256-265.

[33] Milling, L.; Zhang, Y.; Irvine, D. J., Delivering safer immunotherapies for cancer. Advanced drug delivery reviews 2017, 114, 79-101. [34] Blanco, E.; Shen, H.; Ferrari, M., Principles of nanoparticle design for overcoming biological barriers to drug delivery. Nature biotechnology 2015, 33 (9), 941-951.

[34] Le Tourneau, C.; Lee, J. J.; Siu, L. L., Dose escalation methods in phase I cancer clinical trials. JNCI: Journal of the National Cancer Institute 2009, 101 (10), 708-720.

[35] Dobrovolskaia, M. A.; Shurin, M.; Shvedova, A. A., Current understanding of interactions between nanoparticles and the immune system. Toxicology and applied pharmacology 2016, 299, 78-89.

[36] Barenholz, Y. C., Doxil®—the first FDA-approved nano-drug: lessons learned. Journal of controlled release 2012, 160 (2), 117-134. [38] Eble, J. A.; Niland, S., The extracellular matrix in tumor progression and metastasis. Clinical & experimental metastasis 2019, 36 (3), 171-198.

[37] Ma, P.; Mumper, R. J., Paclitaxel nano-delivery systems: a comprehensive review. Journal of nanomedicine & nanotechnology

2013, 4 (2), 1000164.

[38] Pitt, W. G.; Husseini, G. A.; Staples, B. J., Ultrasonic drug delivery–a general review. Expert opinion on drug delivery 2004, 1 (1), 37-56.

[39] Chowdhury, S. M.; Lee, T.; Willmann, J. K., Ultrasound-guided drug delivery in cancer. Ultrasonography 2017, 36 (3), 171. [40] Zhang, Y. R.; Lin, R.; Li, H. J.; He, W. l.; Du, J. Z.; Wang, J., Strategies to improve tumor penetration of nanomedicines through nanoparticle design. Wiley Interdisciplinary Reviews: Nanomedicine and Nanobiotechnology 2019, 11 (1), e1519.

[40] E Konofagou, E.; Tunga, Y.-S.; Choia, J.; Deffieuxa, T.; Baseria, B.; Vlachosa, F., Ultrasound-induced blood-brain barrier opening. Current pharmaceutical biotechnology 2012, 13 (7), 1332-1345.

[41] Kim, D.; Lee, S. S.; Yoo, W. Y.; Moon, H.; Cho, A.; Park, S. Y.; Kim, Y.-S.; Kim, H. R.; Lee, H. J., Combination therapy with doxorubicin-loaded reduced albumin nanoparticles and focused ultrasound in mouse breast cancer xenografts. Pharmaceuticals 2020, 13 (9), 235.

[42] Li, T.; Wang, Y.-N.; Khokhlova, T. D.; D'Andrea, S.; Starr, F.; Chen, H.; McCune, J. S.; Risler, L. J.; Mashadi-Hossein, A.; Hingorani, S. R., Pulsed high-intensity focused ultrasound enhances delivery of doxorubicin in a preclinical model of pancreatic cancer. Cancer research 2015, 75 (18), 3738-3746.

[43] Eranki, A.; Farr, N.; Partanen, A.; Sharma, K. V.; Rossi, C. T.; Rosenberg, A. Z.; Kim, A.; Oetgen, M.; Celik, H.; Woods, D., Mechanical fractionation of tissues using microsecond-long HIFU pulses on a clinical MR-HIFU system. International Journal of Hyperthermia

2018, 34 (8), 1213-1224.

[44] Shi, G.; Zhong, M.; Ye, F.; Zhang, X., Low-frequency HIFU induced cancer immunotherapy: tempting challenges and potential opportunities. Cancer Biology & Medicine 2019, 16 (4), 714.

[45] Eranki, A.; Srinivasan, P.; Ries, M.; Kim, A.; Lazarski, C. A.; Rossi, C. T.; Khokhlova, T. D.; Wilson, E.; Knoblach, S. M.; Sharma, K. V., High-intensity focused ultrasound (HIFU) triggers immune sensitization of refractory murine neuroblastoma to checkpoint inhibitor therapy. Clinical Cancer Research 2020, 26 (5), 1152-1161.

2.2. Combination Therapy with Doxorubicin-Loaded Reduced Albumin Nanoparticles and Focused Ultrasound

2.2.1. Introduction

Breast cancer remains one of the most common cancers in women. It is the second most common cancer among American women, with 13% of the entire female population facing the risk of cancer development some time in their lives [1]. The receptor status of breast cancers is used in clinics to identify the subtypes and subsequent treatment plans [2]. For example, epidermal growth factor 2 (ERBB2/HER2) is a transmembrane receptor tyrosine kinase that is overexpressed in approximately 20% of all breast cancer patients. ERBB2-targeted therapies such as anti-ERBB2 antibodies (such as trastuzumab or pertuzumab) or tyrosine kinase inhibitors (such as lapatinib and neratinib) have been successfully used against these types of breast cancers [2,3]. Nevertheless, for patients that are diagnosed with triple-negative subtypes—those that do not express genes for estrogen, progesterone, and ERBB2 receptors—the anticipated outcome and overall survival (OS) remains much lower (OS of 10–13 months vs. 5 years for ERBB2+) due to the lack of tumor-specific markers and their aggressive nature [2,4]. The standard of care for triple-

negative breast cancer is neoadjuvant chemotherapy, in which drugs such as doxorubicin (DOX) are administered prior to the surgical removal of the tumor [2,5,6]. However, these cytotoxic drugs fail to discriminate between normal and cancerous cells, preventing the use of a large dose due to potential systemic toxicity.

Nanoparticle formulations such as liposomal doxorubicin (Doxil) and albumin-bound paclitaxel (Abraxane) have been developed to overcome such issues. In particular, Abraxane has gained great interest because it was the first commercialized nanoformulation that utilized fully biocompatible, nontoxic, and nonimmunogenic serum proteins for enhancing the therapeutic index. As such, since the advent of albumin nanoparticles, different groups have investigated various methods of albumin nanoparticle formulation [7]. Of such methods, the desolvation method had gained wide popularity due to the simplicity in production with predictable outcomes [8,9]. During the desolvation process, albumins are crosslinked with agents such as glutaraldehyde (GTA) to yield uniform, spherical nanoparticles with negative surface charges. In addition to using GTA as a crosslinker, carbodiimides [10] and thiolated albumins that form additional disulfide crosslinking [11] have been also evaluated. Nevertheless, the presence of open-armed crosslinkers such as the free aldehyde group present on GTA may elicit potential toxicity

or non-specific interactions, preventing the full release of the therapeutic payload. Therefore, we have developed a modified albumin nanoparticle with a reduced surface, which still maintains the important qualities associated with albumin nanoparticles as a vehicle while minimizing active functional groups to eliminate the potential complications described above.

Based on a meta-analysis, less than 0.7% of the administered nanoparticle dose is found to be delivered to the tumor of interest [12]. Therefore, not only is developing a biocompatible drug delivery platform that can selectively release the cargo at the target of interest important, but implementing a method to improve the drug and nanoparticle accumulation at the target to further complement the enhanced permeability and retention (EPR) effect is just as important. To address this issue, the use of focused ultrasound as a method to enhance drug delivery has gained great interest in recent years. This technique has been used to temporarily disrupt the blood–brain barrier (BBB), creating vascular fenestrations for small molecules to extravasate and enter the central nervous system (CNS) [13,14]. In addition, this concept of creating temporary openings has been applied to internal tumors with poor vascularization and high interstitial pressure, allowing the better accumulation of drugs and nanoparticles of interest at the target

[15,16,17].

In this study, we developed acid-sensitive DOX-loaded albumin nanoparticle formulations combined with focused ultrasound treatment for preferential accumulation at the target of interest and competent drug release. Unlike conventional desolvation-based albumin nanoparticles, our reduced albumin nanoparticles fully release the therapeutic cargo at acidic pH as found in the tumor microenvironment and intracellular compartments such as the lysosome. By enhancing the EPR effect, we were also able to increase the accumulation of nanoparticles at the tumor site, which resulted in an improved therapeutic index.

2.2.2. Results

2.2.2.1. Schematics of Albumin Nanoparticles Synthesis

A summary of albumin nanoparticle synthesis is described in Figure 1 based on the method proposed by Langer et al [18]. Human serum albumin (HSA) is first dissolved in water, then ethanol is added to form albumin nanoparticles. Once the nanoparticles form, crosslinkers such as GTA are used to crosslink nanoparticles into stable forms (Figure 2.2.1A). While DOX is added directly to the nanoparticles in the original method (Figure 2.2.1B), we had reduced the albumin nanoparticles first with sodium borohydride before the addition of DOX to ensure that the unreacted aldehydes are converted into unreactive alcohols (Figure

2.2.1C). Such a step was necessary to prevent covalent bonding between DOX and nanoparticles and to facilitate improved drug release.

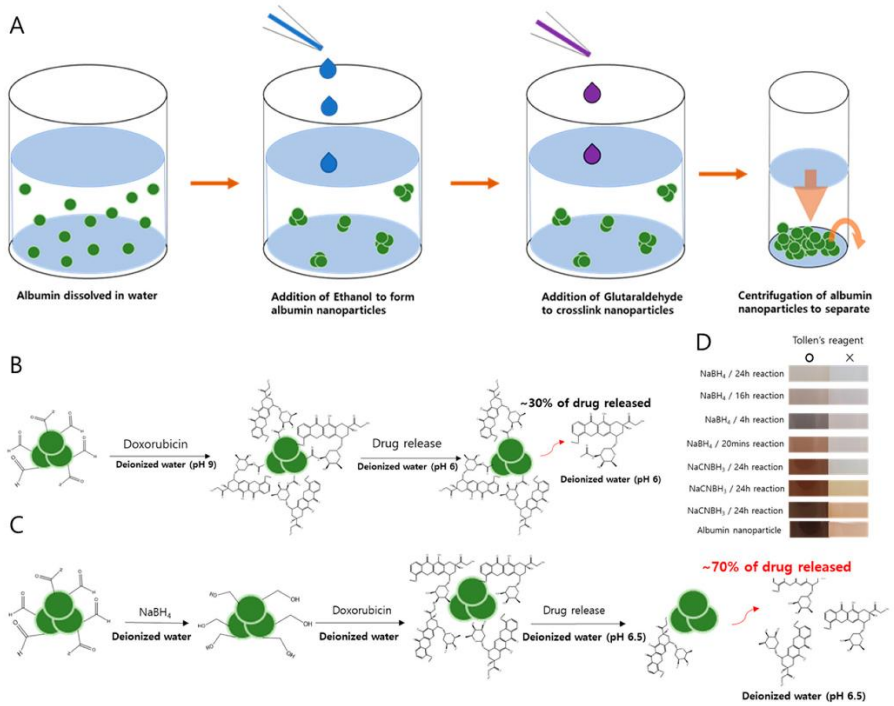

Figure 2.2.1. The synthesis and reduction protocols for albumin nanoparticles. (A) The desolvation method proposed by Langer et al. [18] is modified in the synthesis of albumin nanoparticles. (B) Speculated reaction of aldehyde–doxorubicin (DOX). (C) Schematic diagram of the interaction between reduced albumin nanoparticles (rAlb-NPs) and DOX after reducing aldehydes to alcohol. (D) Detection of aldehydes was performed by the Tollens' test to confirm the removal of unreacted aldehyde from the surface of the nanoparticles.

2.2.2.2. Characterization of the Albumin Nanoparticles

The albumin nanoparticles (Alb-NPs) based on the desolvation method and reduced albumin nanoparticles (rAlb-NPs) were characterized according to size and zeta potential (Table 2.2.1). For size and zeta potential measurements, the dynamic light scattering technique was used (Malvern Zetasizer Nano, Malvern Instrument Ltd., Malvern, UK). There were no significant differences between the sizes and the total yields of the nanoparticle formulations, with the mean diameter of the Alb-NPs being 146 ± 37.5 nm and that of the rAlb-NPs being 142 ± 31.1 nm. The sizes and the shapes of the nanoparticles were also evaluated with SEM and TEM images (Figure 2.2.2), which showed a group of spherical nanoparticles that were well-dispersed across the medium. However, it was observed that the zeta potential values of the Alb-NPs were more extreme than those of rAlb-NPs, with each having voltages of −51.3 ± 2.1 and −24.4 ± 2.8 mV, respectively. We speculated that the functional groups on the surface of the Alb-NPs contributed to the negative charges, and the subsequent reduction of the surface functional groups led to increased zeta potential of reduced albumin nanoparticles. In addition, the stability of the nanoparticles was monitored for up to 6 months. At designated times, aliquots of the nanoparticles were removed from 4 °C storage, and their size and zeta

potential were measured using the DLS technique. The sizes and zeta potentials of the nanoparticles remained consistent, suggesting their excellent stability in solution (Table 2.2.2). Furthermore, the rAlb-NPs were checked for purity using inductively coupled plasma atomic transmission spectroscopy (ICP-AES), where chemical elements such as boron could be detected. According to the ICP data, 31.17 ppm of boron was detected per 60 mg/mL of rAlb-NPs, which would be considered as negligible and non-toxic to the human body [19].

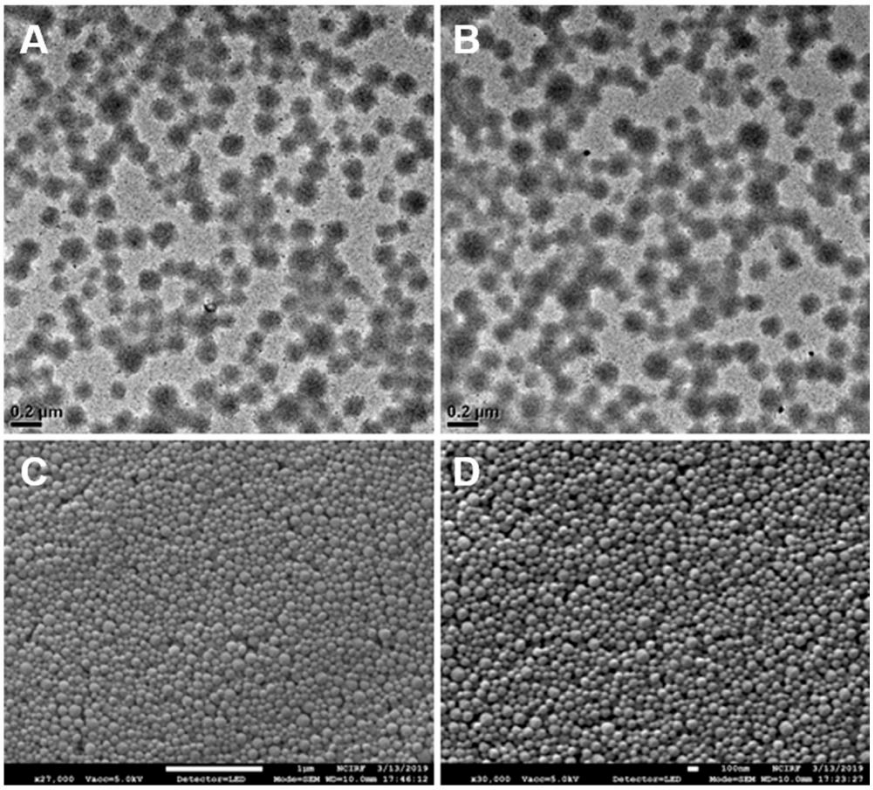

Figure 2.2.2. Images of Alb-NPs and rAlb-NPs obtained by electron microscopy. Based on the analysis of the images, the two nanoparticles had similar spherical morphology and size. (A) TEM images of rAlb-NPs. (B) TEM images of Alb-NPs. (C) SEM images of rAlb-NPs. (D) SEM images of Alb-NPs.

Nanoparticles	Mean Size (Mean ± SD, nm)	Zeta Potential (mV)
Alb-NPs	146 ± 37.5	−51.3 ± 2.1
rAlb-NPs	142 ± 31.1	−24.4 ± 2.8
cDOX	151 ± 21.5	−27.5 ± 1.1
sDOX	144 ± 28.2	−21.6 ± 1.6
rDOX	146 ± 31.8	−14.7 ± 0.8

Table 2.2.1. The average size and the zeta potential values of albumin nanoparticles (Alb-NPs, rAlb-NPs, sDOX, rDOX, and cDOX) (n = 3).

Nanoparticles	Days	Mean Size (Mean ± SD, nm)	Zeta Potential (mV)
Alb-NPs	1	146.8 ± 40.1	−50.1 ± 3.75
	3	142.9 ± 38.7	−51.4 ± 4.17
	7	137.3 ± 30.4	−46.7 ± 3.27
	14	151.7 ± 28.0	−49.5 ± 5.81
	30	148.1 ± 31.7	−47.9 ± 2.37
	90	145.8 ± 38.1	−50.5 ± 3.04
	180	150.7 ± 41.4	−48.1 ± 2.90
rAlb-NPs	1	142.6 ± 45.8	−27.2 ± 3.75
	3	148.6 ± 37.8	−28.6 ± 5.85
	7	148.2 ± 29.4	−26.3 ± 3.10
	14	145.9 ± 34.1	−21.8 ± 2.94
	30	141.8 ± 33.8	−31.7 ± 4.51
	90	148.1 ± 30.4	−27.2 ± 4.48
	180	146.4 ± 32.1	−28.1 ± 3.41

Table 2.2.2. The stability of albumin nanoparticles at 4 °C over time evaluated by changes in their size and zeta potential (n = 3).

The three types of DOX-loaded Alb-NPs were then characterized. According to the DLS measurements, the mean diameters of the DOX-loaded Alb-NPs were 151 ± 21.5 nm for cDOX, 144 ± 28.2 nm for sDOX, and 146 ± 31.8 nm for rDOX (Table 2.2.1). Based on the data, the presence of doxorubicin on the surface of the nanoparticles did not affect the overall size of the Alb-NPs. Nevertheless, the zeta potential of sDOX (from Alb-NPs) was smaller (−21.6 ± 1.6 mV) than that of rDOX (from rAlb-NPs, −14.7 ± 0.8 mV), which corresponds to the zeta potential measurements of the parent albumin nanoparticles.

2.2.2.3. Loading and Release Kinetics of cDOX, sDOX, and rDOX

Next, the loading and release kinetics of DOX-loaded albumin nanoparticles were evaluated. For cDOX, the "encapsulation" efficiency was calculated differently because DOX was added to the nanoparticles during the desolvation process. A DOX/human serum albumin (HSA) ratio of 1:10 (wt/wt) was used throughout the entire process because higher DOX concentrations (1:1, 1:3, and 1:5 DOX to HSA ratios) caused the zeta potential values to approach 0 mV, inducing aggregation of the nanoparticles. Accordingly, the loading efficiency of DOX on cDOX, sDOX, and rDOX was 67.1 ± 5.87%, 95.2 ± 5.21%, and 95.1 ± 3.51% at the 1:10 ratio, respectively, when the supernatants were analyzed using HPLC (Table 2.2.3).

Nanoparticles	Ratio (*w*/*w*)	Loading Efficiency (%)	Extraction @ pH 1 (%)
cDOX	10:1	67.1 ± 5.87	21.74 ± 5.12
	5:1	Aggregation	Aggregation
	3:1	Aggregation	Aggregation
sDOX	10:1	95.2 ± 5.21	50.1 ± 3.75
	5:1	93.4 ± 3.73	51.4 ± 5.17
	3:1	94.7 ± 4.71	46.7 ± 5.27
rDOX	10:1	95.1 ± 3.51	97.4 ± 4.27
	5:1	Aggregation	Aggregation
	3:1	Aggregation	Aggregation

Table 2.2.3. The loading efficiency and extraction of DOX on/from albumin nanoparticles (n = 3).

We also studied the release kinetics for the drug payloads from the albumin nanoparticles under acidic conditions and the stimulus of ultrasound. We speculated that with increased protons in the environment, the release of DOX would be favored as the pH became more acidic (e.g., in the tumor microenvironment) and the electrostatic interaction between the drug and the nanoparticle became reversed to the point where almost all the DOX would be released in extremely acidic environments. Therefore, the profiles of DOX release from the nanoparticles were evaluated at multiple pHs. Surprisingly, we observed that for cDOX and sDOX, a maximum of 40% of the loaded drug was released regardless of how acidic the environment was, while approximately 60% of the drug remained bound to the nanoparticles (Figure 2.2.3). Nonetheless, the release kinetics were much better for rDOX, with more than 93% of the drug being released after 24 h. We then tried to extract the DOX bound to the nanoparticles by decreasing the pH of the release media to 1. Nevertheless, only a slight increase in DOX was detected after extraction (Table 2.2.3). We speculated that the presence of free aldehyde arms from the GTA crosslinker and non-specific binding pockets of the albumin could induce non-specific binding with the amine group present on DOX molecules, inducing a strong, irreversible linkage. To further develop this

hypothesis, we used Tollens' reagent to evaluate the presence of active aldehydes on the albumin nanoparticles. According to the colorimetric analysis, we were able to observe that the unreduced Alb-NPs had a strong presence of reactive aldehydes on their surface, while using stronger reducing agents (sodium borohydride instead of sodium cyanoborohydride for a longer period) led to a near-complete elimination of the aldehyde groups on the nanoparticles without strongly affecting their properties (Figure 2.2.1D).

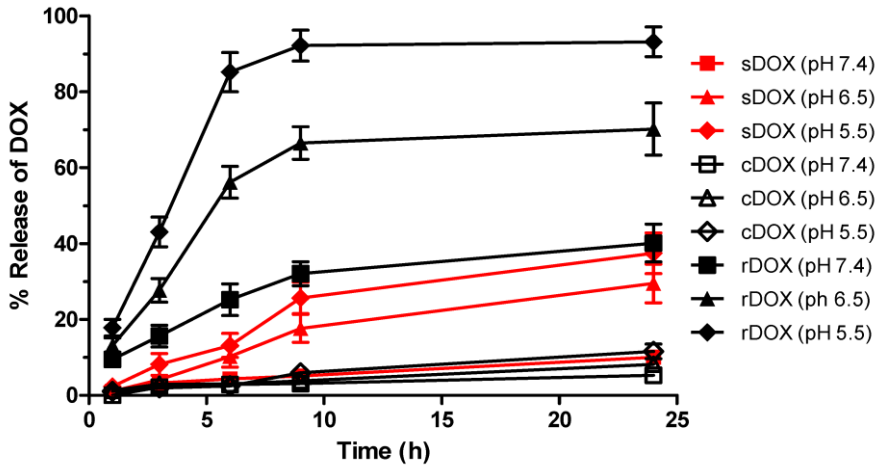

Figure 2.2.3. The pH-dependent release of DOX from albumin nanoparticles. rDOX with minimal non-specific interactions had improved release kinetics compared to cDOX or sDOX, affirming the results from DOX extraction. Values are mean ± SD (n = 3).

2.2.2.4. In Vitro Cell Viability Study and Confocal Microscopy

The cytotoxic effects of albumin nanoparticles and DOX-loaded nanoparticles were first evaluated in vitro using the Raw264.7 murine macrophage cell line and MDA-MB-231 human breast cancer cells. First, the effects of bare albumin nanoparticles on the cell viability of Raw264.7 cells were examined by incubating different concentrations of Alb-NPs and rAlb-NPs with the cells. It was observed that both Alb-NPs and rAlb-NPs did not have a significant effect on Raw264.7 (Figure 4A) and MDA-MB-231 (Figure 2.2.4B) cell viability and morphology when up to 500 μg/mL (HSA concentration) of the nanoparticles were tested. Furthermore, the cytotoxic effects of DOX-loaded sDOX, cDOX, and rDOX were compared with those of the free drug, and the IC50 values were obtained. At 24 h post-incubation, the IC50 values of DOX, sDOX, cDOX, and rDOX were 5.24 ± 0.67, 20.36 ± 3.73, 54.04 ± 7.87, and 5.69 ± 0.85 μg/mL (DOX concentration), respectively, while at 48 h and 72 h post-incubation, the IC50 values were 0.96 ± 0.09, 2.79 ± 0.41, 6.66 ± 0.93, and 1.17 ± 0.11 μg/mL at 48 h and 0.40 ± 0.03, 0.56 ± 0.06, 1.84 ± 0.19, and 0.34 ± 0.02 μg/mL at 72 h for DOX, sDOX, cDOX, and rDOX, respectively (Figure 2.2.4C). Based on the data, while the IC50 value at 24 h post-incubation was lowest for the free drug, rDOX had the lowest

IC50 values at 72 h, suggesting that by allowing sufficient release, the nanoparticle formulations can enhance the therapeutic effect induced by the parent drug. Furthermore, based on the poor release data and IC50 values observed for cDOX, it was excluded from further studies.

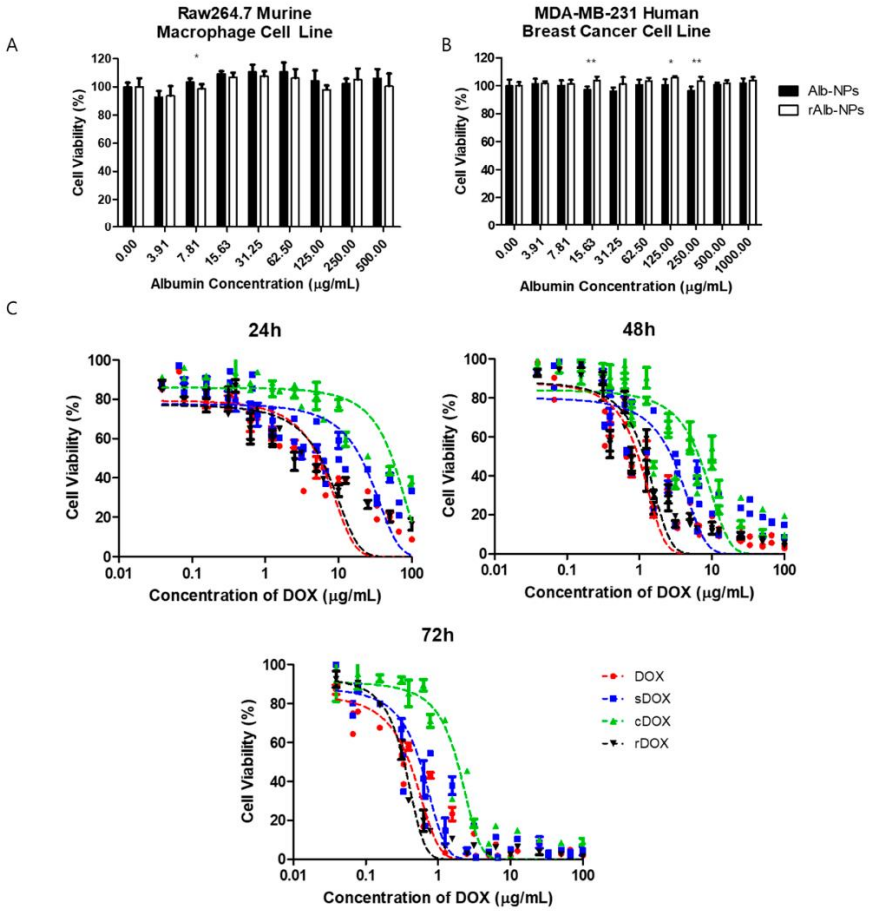

Figure 2.2.4. Cytotoxicity of albumin nanoparticles and drug-loaded albumin nanoparticles in vitro. First, the cytotoxicity of the vehicles (Alb-NPs and rAlb-NPs) were evaluated using (A) Raw264.7 murine macrophage cells and (B) MDA-MB-231 human breast cancer cells at different nanoparticle concentrations. (C) The cytotoxicity of DOX, sDOX, cDOX, and rDOX at various time points was compared, and the IC50 values were calculated. Values are mean ± SD (n = 6). * $p \leq 0.05$, ** $p \leq 0.01$.

Next, we had prepared slides for examination with confocal microscopy. MDA-MB-231 cells were incubated with Cy5.5-labeled Alb-NPs, DOX, sDOX, and rDOX for up to 24 h. Because the presence of DOX distorted cell morphology and viability, we decided to evaluate the endocytosis of the drug and the nanoparticles at 2 h after incubation, before DOX initiated the necrotic effects. Based on the confocal pictures taken, the bare albumin nanoparticles were able to localize within the tumor cells (Figure 2.2.5). Unlike that of the free drug, the distribution of DOX within the cell was not localized at the nucleus at the 2 h time point but rather distributed through the cell cytoplasm, which is consistent with the drug release data showing that 24 h was required for DOX to be fully released from the albumin nanoparticles. The exact mechanism behind the endocytosis of the albumin nanoparticles into the cells remains to be elucidated.

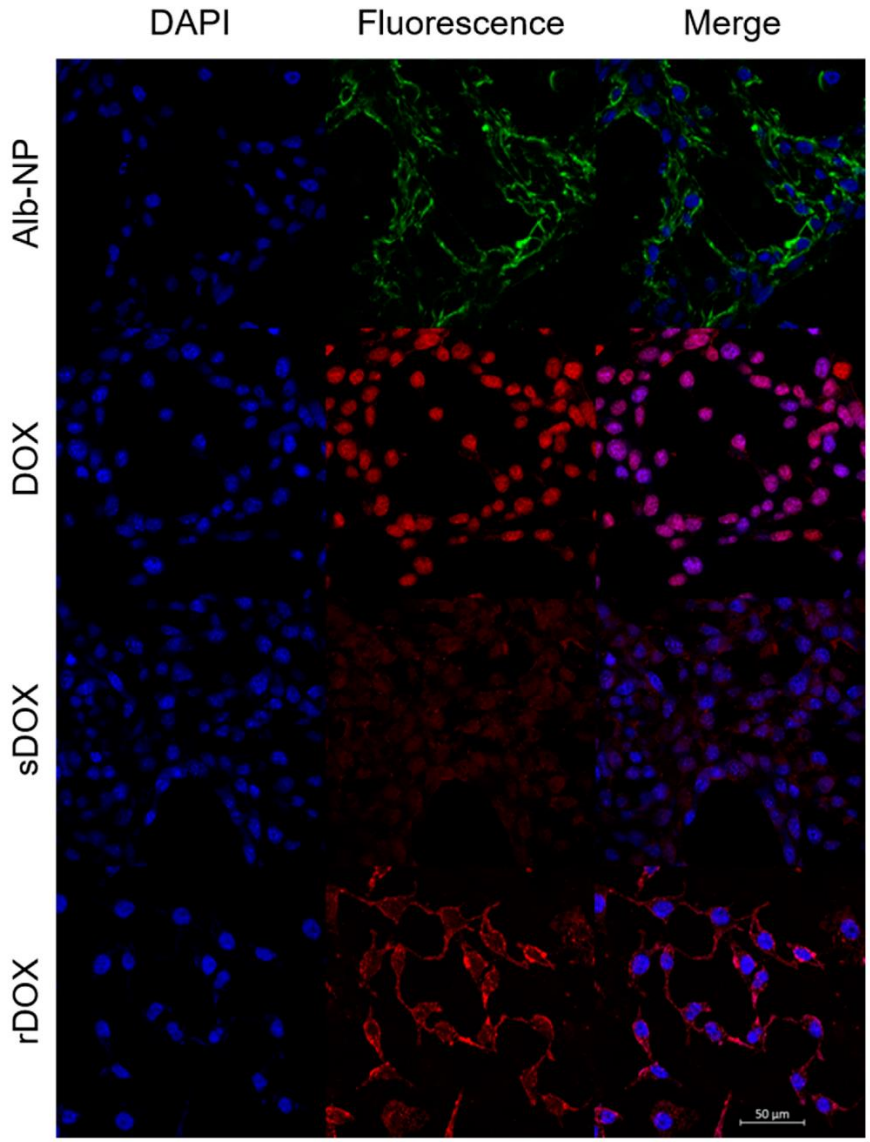

Figure 2.2.5. Confocal images of MDA-MB-231 cells treated with different albumin nanoparticles. Images were taken two hours after initial incubation to maximize the internalization of the nanoparticles while minimizing the cytotoxic effects of DOX on cell morphology. Scale bar: 50 µm.

2.2.2.5. Evaluation of Ultrasound Treatment and Biodistribution

To establish the localization of nanoparticles at the tumor site and the effects of ultrasound on enhanced drug delivery, we prepared Cy5.5-labeled Alb-NPs and rAlb-NPs to be administered intravenously into the subcutaneous xenograft mouse models. We first attempted to establish the ultrasound treatment conditions by evaluating the amount of Cy5.5-labeled albumin nanoparticles accumulated at the treated tumors. Four experimental groups, including the negative control group receiving saline, mice receiving Cy5.5-Alb-NPs, mice receiving Cy5.5-Alb-NPs with ultrasound exposure, and those receiving Cy5.5-Alb-NPs with microbubbles and ultrasound treatment were prepared (n = 3 per experimental group). At 24 h after injection, the mice were sacrificed and the tumors were isolated for In Vivo Imaging System (IVIS) Spectrum analysis. The group of mice that received the nanoparticles with complete ultrasound treatment (ultrasound + microbubbles) had significantly higher fluorescence from the tumors compared to those that received only the nanoparticles or nanoparticles with ultrasound only (Figure 2.2.6A). Intrigued by this result, we then assessed the effects of ultrasound treatment on the general biodistribution. The same experimental groups were prepared using new sets of mice (n = 3 per experimental group), and various organs including the heart, kidneys,

lungs, liver, and spleen and the implanted tumor were collected. Organ-based analysis revealed that the injected nanoparticles had localized mostly in the liver, while some fluorescence was observed in the spleens, kidneys, and the tumors as well (Figure 2.2.6B). Similar to in the previous experiments, enhanced accumulation of fluorescence signals was observed in the tumors of the mice that received the complete ultrasound treatment.

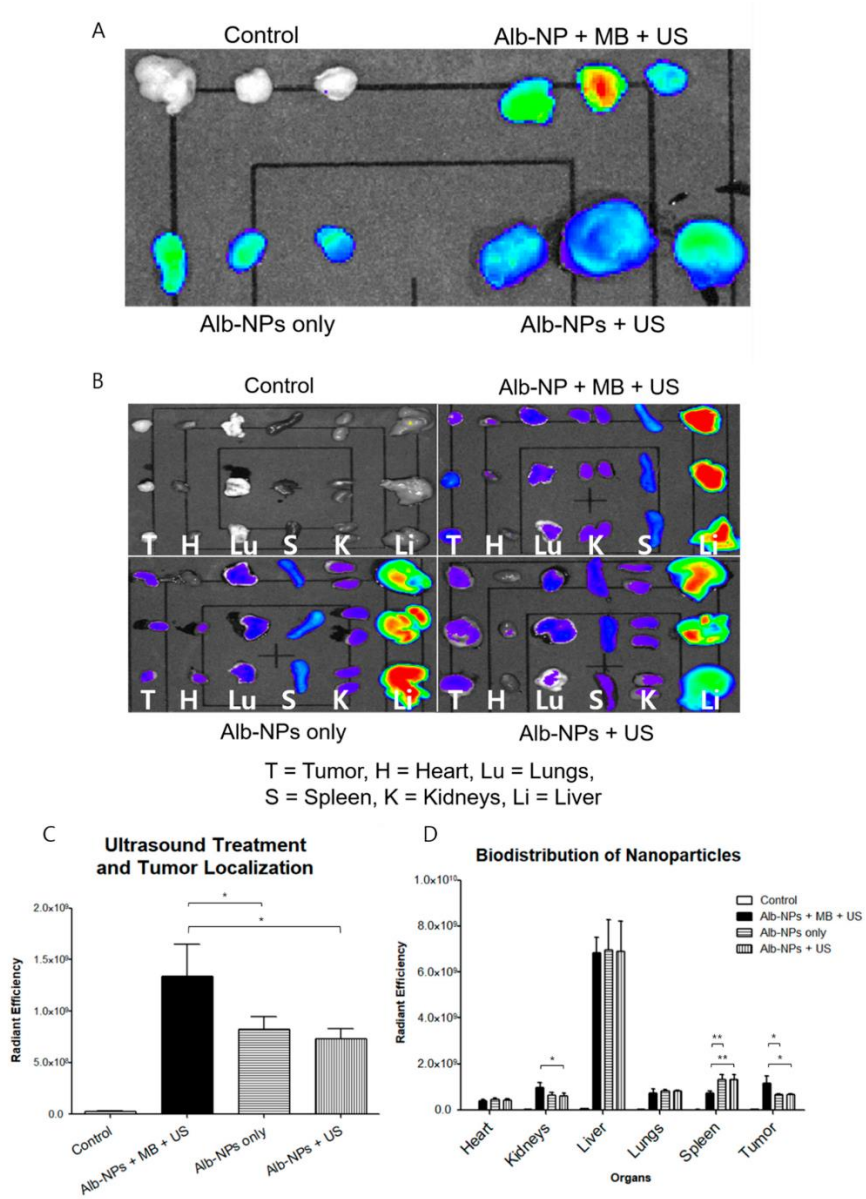

Figure 2.2.6. Biodistribution profiles of albumin nanoparticles in murine tumor models. (A) The effects of ultrasound treatment on the enhancement of albumin nanoparticle localization at the tumor were evaluated with the In Vivo Imaging System (IVIS) Spectrum 24 h after intravenous injection. (B) The

biodistribution of albumin nanoparticles across major organs (the heart, kidneys, liver, lungs, spleen, and tumor) was evaluated with the IVIS Spectrum 24 h after intravenous injection. (C,D) represent the calculated fluorescence data from the respective organs. Values are mean ± SD (n = 3), * $p \leq 0.05$, ** $p \leq 0.01$.

2.2.2.6. In Vivo Efficacy and Safety Study

Lastly, we prepared a set of experiments to evaluate the therapeutic index of the DOX-loaded albumin nanoparticles. Eight experimental groups bearing MDA-MB-231 breast cancer models were prepared as described in the Materials and Methods section: (i) negative control injected with saline, (ii) ultrasound treatment only, (iii) DOX (2 mg/kg), (iv) sDOX only (2 mg/kg), (v) rDOX only (2 mg/kg), (vi) DOX + US, (vii) Sdox + US, and (viii) rDOX + US. A dose of 2 mg/kg of DOX was used for all therapeutic protocols unless described otherwise. First, the ultrasound treatment (focused ultrasound + microbubble) itself did not have a significant effect on the tumor growth, as the tumor growth in both the control group and the ultrasound only group was unchanged (Figure 2.2.7A). Furthermore, while all formulations that contained DOX had significantly retarded the tumor growth, rDOX was the most effective. Specifically, when rDOX was complemented with focused ultrasound, the therapeutic efficacy was maximized. It is also worth noting that all the protocols, including those that included DOX, did not induce significant changes in the weights of the mice (Figure 2.2.7B).

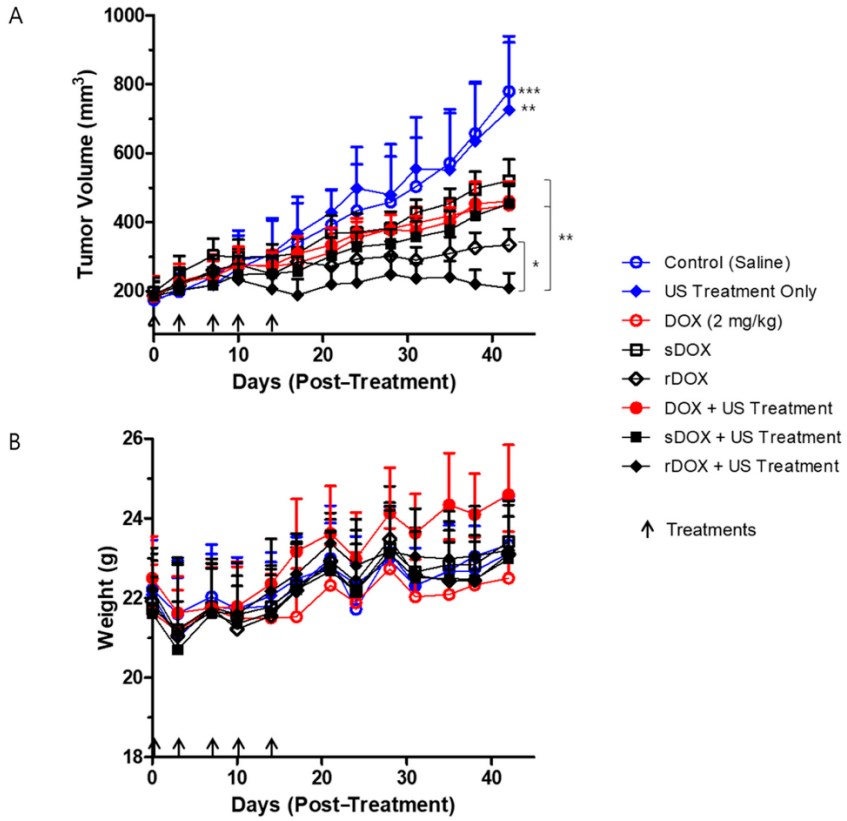

Figure 2.2.7. Efficacy of treatment protocols against tumor growth, and the changes in body weight. (A) Significant differences between the control groups (groups that received saline and ultrasound treatment only) and the treatment groups (DOX/DOX + Ultrasound (US), sDOX/sDOX+US, rDOX/rDOX + US), DOX/sDOX and rDOX groups, and rDOX and rDOX+US were observed. A concentration equivalent of 2 mg/kg DOX was used per treatment. (B) No significant changes in the body weights of the different groups were observed during the entire experiment. Values are mean ± SD (n = 5). * $p \leq 0.05$, ** $p \leq 0.01$, *** $p \leq 0.001$.

In addition to monitoring the mice's weights during the efficacy studies, we also tried to assess the safety by performing different experiments to evaluate single-dose acute toxicity, dose–response survival, body weight, and organ weights. Based on the in vitro cytotoxicity and the in vivo efficacy data, rAlb-NPs, free DOX, and rDOX formulations were compared. First, when different concentrations of the three formulations were examined, the LD50 of the rAlb-NPs was over 400 mg/kg (HSA concentration), as none of the mice had died or showed a significant clinical symptom. On the other hand, the LD50 for DOX and rDOX were 15 and 87.5 mg/kg (DOX concentration), respectively, suggesting that the nanoformulation had significantly improved the toxicity profiles compared to that of the free drug (Figure 2.2.8A). Similarly, the groups that were intravenously administered a single dose of more than 20 mg/kg of free DOX, or 100 mg/kg of rDOX (DOX concentration) had died within a week of receiving the treatment protocols (Figure 8B), while those that received less than that amount had survived for more than two weeks without significant changes in their body weights (Figure 2.2.8C). Lastly, the approximated maximum tolerated doses for DOX (10 mg/kg) and rDOX (75 mg/kg) administered and the major organs from these experimental mice (the liver, lungs, spleen, kidneys, and heart) were collected for analysis. The weights of

the livers and hearts of the mice that received 10 mg/kg DOX were significantly larger than those of the control mice, while the weights of the hearts in the mouse cohort that received rDOX were significantly lower than those that received DOX injection as well (Figure 2.2.8D).

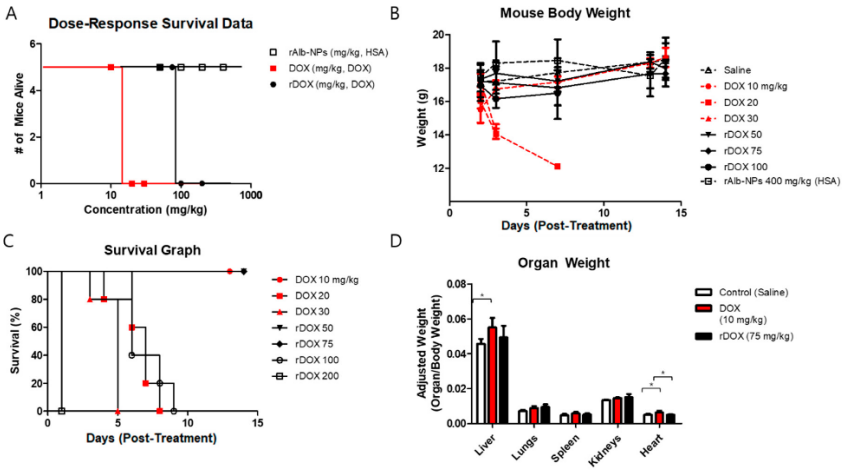

Figure 2.2.8. Assessment of safety profiles of albumin nanoparticles and DOX-loaded albumin nanoparticles. (A) Dose–response survival was obtained by using different concentrations of the rAlb-NPs, DOX, and rDOX. The LD50 for DOX was approximately 15 mg/kg, and that for rDOX was 87.5 mg/kg. The LD50 for rAlb-NPs could not be defined because no mice had died up to 400 mg/kg (human serum albumin concentration). (B) The mouse group that received less than the LD50 values consistently gained weight, while those receiving significant doses had a dramatic reduction in body weights. (C) The mouse group that received significant doses of the treatment protocol had died within a week of acute injection. (D) The analysis of organ weights showed that there was a significant difference in the heart, an organ known to be affected by DOX. Additionally, the livers of those that received 10 mg/kg DOX weighed more than those of the control mice. Values are mean ± SD (n = 5). * $p \leq 0.05$.

2.2.3. Discussion

Many chemotherapies that are used in clinics today are flawed due to the potential toxicity associated with them. Anthracyclines such as doxorubicin that intercalate between the DNA base pairs and prevent DNA replication are extremely efficient in exerting cytotoxic effects against cancerous cells, but they are indiscriminative and damage normal cells as well [20,21]. The known side-effects of doxorubicin include dose-dependent cardiac toxicity from dilated cardiomyopathy, which can lead to congestive heart failures [21,22,23]. Accordingly, various efforts have been combined to address two central aims in drug-mediated therapies: maximizing drug specificity by enhancing the amount of drug exposure only at the target of interest and minimizing drug toxicity by reducing the amounts of drugs that reach non-targeted regions (i.e., normal cells) and elicit non-specific damage. Nanoparticle formulations based on organic materials such as phospholipids, polymers, or proteins have been used in the past, but many of these formulations were based on weak interactions between the constituents, leaving their stability to be questioned [24,25]. Those that use covalent crosslinking to enhance the stability of the nanoparticles have been also researched, but the extent to which crosslinkers could have potential non-specific interactions have not been considered. The amine groups present on DOX have been often

utilized as a target for stable crosslinking onto nanoformulations [26,27,28]. However, while this covalent bonding would be useful for stability, the efficacy and toxicity profiles of the drug would then need to be re-evaluated completely because the molecular characteristics would change dramatically.

To address these challenges, we present a novel combination of albumin-based nanoparticle formulations with focused ultrasound treatment to greatly improve both efficacy and toxicity profiles. Such nanoformulations are first reacted with sodium borohydride to reduce active aldehyde groups on the surface to alcohols, minimizing their potential toxicity and reactivity. As the active aldehyde groups are eliminated, the amine group on DOX will not react covalently with the particles' surface, ensuring that the loaded DOX is bound on the reduced nanoparticles mainly by the reversible electrostatic forces, unlike for the regular albumin nanoparticles. Such a reduction step could therefore allow the improved controlled release of the therapeutic payload upon specific triggers such as acidic pH without altering the structure of the contents themselves involved in the breakdown of covalent bonds. The release of DOX from the albumin nanoparticles, especially from the reduced ones, was therefore maximized when the pH of the environment was acidic—as found in tumor microenvironments, where the pH is

reported to be <6.5 [29]—but not in regions with physiological conditions, as described in Figure 3. The data from confocal microscopy also support this hypothesis, as it was observed that stronger fluorescence signals were observed with rDOX at 2 h post-incubation than with sDOX, which we speculate to be induced by the improved release of the drug. Cardiotoxicity, including changes in myocardial structure and function to severe cardiomyopathy, is a major side-effect associated with the administration of DOX at high doses. One of the clinical symptoms associated with such heart conditions is cardiac enlargement, which can cause heart failure. Based on our organ-based toxicity data, cardiac enlargement was observed in the mice with one-time administration of 10 mg/kg of free DOX, but not in the mice that received 75 mg/kg DOX loaded on albumin nanoparticle formulations. In addition, the rAlb-NP vehicle itself did not cause any significant changes in the survival, overall body mass, individual organs, or observable behavioral patterns at up to 400 mg/kg, suggesting that the albumin nanoparticles themselves are not toxic.

We also employed focused ultrasound to enhance the accumulation of nanoparticles where the local release of DOX would be facilitated. The use of ultrasound to improve local drug delivery is a relatively well-established technique that is currently being applied in numerous

preclinical and clinical models, including brain, breast, and pancreatic cancers. By temporarily disrupting the endothelial linings by microbubble-assisted cavitation, focused ultrasound can further augment the enhanced permeability and retention effects and increase the number of nanoparticles available locally, as observed from the IVIS Spectrum-based fluorescence data. Combining both the enhanced localization and improved control of DOX release, we observed a significant improvement in the anti-cancer activities when rDOX was used in combination with focused ultrasound, compared to standalone DOX therapies or rDOX therapies. However, unlike rDOX vs. Rdox + US, we did not observe a statistically significant increase in anti-cancer effects for DOX vs. DOX+US or sDOX vs. sDOX + US. We hypothesized two potential explanations for the observed phenomena based on experimental evidence: (1) Ultrasound-mediated drug delivery is most effective against tumors with low permeability [30,31]. Because DOX molecules themselves were effective (i.e., able to reach the tumor to elicit anti-cancer effects) in the mouse models used in this study, introducing ultrasound treatment to enhance permeability was not as effective as in other models such as pancreatic cancer models [15] reported in the literature. (2) Nanoparticles are much bigger than the drug molecules themselves; therefore, using ultrasound to introduce extra fenestrations

in the vasculature for extravasation into the tumor interstitial space would be much more beneficial for the nanoparticles than the drugs, as observed in rDOX vs. rDOX + US. Nevertheless, because sDOX has poor release profiles when compared to rDOX, not all sDOX molecules that reach the tumor microenvironment may fully release their payload, reducing their therapeutic efficacy. Nevertheless, the tremendous increase in the therapeutic efficacy and toxicity profiles presented by rDOX and its synergistic effects with focused ultrasound shows promise for the next generation of drug delivery platforms using fully biocompatible albumin-based nanoparticles in combination with an external stimulus. Further studies on optimizing the therapeutic conditions, including the drug dose, schedule, ultrasound parameters, drug combinations, and potential resistance, are required to maximize such potential and introduction into clinical settings.

2.2.4. Materials and Methods

2.2.4.1. Reagents and Equipment

Human serum albumin (HSA) was acquired from SK Chemicals (SK Chemicals, Seongnam, Korea). Doxorubicin (DOX) was acquired from Boryung Pharmaceutical (Boryung Pharmaceutical, Seoul, Korea). Sodium borohydride ($NaBH_4$), sodium cyanoborohydride ($NaCNBH_3$), silver nitrate solution, and glutaraldehyde (GTA) were purchased from Sigma Aldrich (St. Louis, MO, USA). SonoVue® microbubbles (MB) were acquired from Bracco (Bracco, Italy). Zolazepam (Zoletil®) was obtained from Virbac (Virbac, Carros, France), and xylazine hydrochloride (Rompun 2%) was acquired from Bayer (Bayer Korea, Seoul, Korea). The 1260 Infinity II LC system was acquired from Agilent Technologies (Agilent Technologies, Santa Clara, CA, USA). The VIFU 2000® was acquired from Alpinion Medical Systems (Alpinion Medical Systems Co., Ltd., Seoul, Korea).

2.2.4.2. Preparation of Albumin Nanoparticles

Human serum albumin nanoparticles (Alb-NPs) were synthesized based on a modified desolvation protocol [18]. One gram of HSA was added to 340 mL of distilled water, and 2000 μL of 1 M sodium hydroxide (NaOH) was added dropwise to adjust the pH. To induce the agglomeration of HSA, ethanol was added dropwise under stirring

conditions (500 rpm) at room temperature until turbidity of the solution was obtained. Excess 8% GTA solution (1000 μL) was added to the HSA aggregates and reacted for 24 h under stirring conditions to ensure complete crosslinking. After crosslinking was completed, the solution was centrifugated at 15,000 rpm for 15 min at 4 °C, and the pellet was re-dispersed with distilled water three times to remove unbound chemicals and then kept in a refrigerator until further use.

2.2.4.3. Preparation of Reduced Alb-NPs (rAlb-NPs)

One hundred micrograms of Alb-NPs was added to 20 mL of ethanol, and 100 μL of reducing agent (sodium borohydride and sodium cyanoborohydride, respectively) was added under stirring (500 rpm) overnight. The pH was adjusted to 7.5~8.5 with 1 M sodium hydroxide. The solution was centrifugated at 15,000 rpm for 15 min at 4 °C, and the pellet was re-dispersed with distilled water three times to remove unbound chemicals and then kept in a refrigerator until further use. In addition, the rAlb-NPs were checked for purity using the ICP-AES methodology.

2.2.4.4. Characterization of the Alb-NPs and rAlb-NPs

The hydrodynamic size, polydispersity, and zeta potential of the prepared nanoparticles were measured using the dynamic light scattering (DLS) method (Zetasizer Nano ZS90; Malvern Instruments, Malvern,

UK). The detection of free aldehyde in both groups was performed using Tollens' reagent according to the manufacturer's protocol. In short, 0.3 M NaOH solution was added dropwise to 0.3 M silver nitrate solution until a silver precipitate formed, to which 3 M ammonia solution was added dropwise until the solution's color became transparent. Ten milliliters of the prepared Tollens' reagent was added to 10 mL of 1 mg/mL of Alb-NPs or rAlb-NPs (reduced by $NaBH_4$ or $NaCNBH_3$) and reacted for 6 or 24 h, and the change in color was observed. The detection of boron was evaluated using ICP-AES at the National Center for Inter-University Facilities (Seoul National University, Korea). The morphology and size of the nanoparticles were further studied with transmission electron microscopy (TEM) and scanning electron microscopy (SEM) for further analysis at the National Center for Inter-University Facilities, Seoul National University (South Korea). Last, the stability of the nanoparticles was analyzed by characterizing the stored nanoparticles every month.

2.2.4.5. Preparation of DOX-Loaded Albumin Nanoparticles

We have evaluated three different methods of loading DOX onto the albumin nanoparticles. The first method involved encapsulating DOX before ethanol addition during the desolvation process. DOX was added in weight ratios of 1:3, 1:5, and 1:10 of DOX to HSA. The HSA–DOX

mixture was stirred for an hour; then, ethanol was added dropwise until the mixture turned turbid. GTA (8%) was added, and the reaction was performed for 24 h under stirring conditions (500 rpm). After the crosslinking of the HSA and DOX mixture was completed, the solution was centrifuged at 15,000 rpm for 15 min at 4 °C and the pellet was re-dispersed with distilled water three times to remove unbound chemicals. The supernatants from each wash were collected and analyzed with HPLC to calculate the loading efficiency for DOX. The albumin nanoparticles encapsulating DOX were termed cDOX.

The second and the third methods of loading DOX involved first synthesizing albumin nanoparticles based on the desolvation and reduction methods outlined previously and then coating the Alb-NPs with DOX. A 90 mg amount of the albumin nanoparticles in 5 mL of solution (prepared according to Section 4.2 and Section 4.3) was reacted with DOX at different weight ratios (w/w% of 1:1, 1:2, 1:3, 1:5, and 1:10 DOX/albumin nanoparticles) for 24 h at room temperature in the dark under stirring conditions (500 rpm). The DOX–albumin nanoparticle mixtures were topped up to 10 mL using deionized water and adjusted to pH 8.5 to prevent aggregation during the reaction. The solution was centrifugated at 18,000 rpm for 15 min at 4 °C, and the pellet was re-dispersed with distilled water three times to remove unbound chemicals.

The supernatants from each wash were collected and analyzed with HPLC to calculate the loading efficiency for DOX. The albumin nanoparticles coated with DOX were termed sDOX and rDOX (reduced).

2.2.4.6. In Vitro Kinetics of DOX Release from Albumin Nanoparticles

cDOX, sDOX, and rDOX were added at 50 mg/mL into membrane dialysis bags (cutoff Molecular Weight (MW), 2000), which were transferred into beakers containing 50 mL of buffer solutions prepared at various pHs (pH 7.4, 6.5, and 5.5). The solutions were incubated at 37 °C while under mechanical stirring. At each time point (1, 3, 6, 9, and 24 h after addition), 1 mL aliquots of the solutions were transferred to 1.5 mL Eppendorf tubes and centrifuged at 15,000 rpm for 30 min at 4 °C to separate the released DOX from the nanoparticles. The amount of DOX released from the nanoparticles was measured by analyzing the supernatants with HPLC at 260 nm to quantify the amount of DOX released.

2.2.4.6. Cell Culture

Human triple-negative breast cancer cell line MDA-MB-231 and murine macrophage cell line Raw264.7 cells were acquired from the American Type Culture Collection (ATCC) and were cultured in Dulbecco's Modified Eagle Medium (DMEM) supplemented with 10% heat-inactivated fetal bovine serum (FBS), 100 IU/mL penicillin, 100

mg/mL streptomycin, and 2 mM L-glutamine. Cultures were maintained in a humidified atmosphere with 5% CO2 at 37 °C and routinely tested for mycoplasma contamination. Cells were sub-cultured once they reached 80% confluency, determined by the trypan blue dye exclusion method.

2.2.4.7. Cell Viability Assay

The CellTiter 96® AQueous One Solution Cell Proliferation Assay (MTS) was used to assess the effects of nanoparticles on cell viability. MDA-MB-231 and Raw264.7 cells were seeded on 96-well plates at a density of 5×10^3 cells per well and incubated overnight. First, the effects of bare albumin nanoparticles on cell viability were evaluated by adding various concentrations of Alb-NPs and rAlb-NPs to both Raw264.7 and MDA-MB-231 cells. In addition, the cytotoxic effects of the drugs were examined by adding DOX, cDOX, sDOX, and rDOX into cells and incubating for up to 72 h. Cells were removed from the incubator at designated time points, and their viability was evaluated against the phosphate-buffered saline (PBS) controls using the MTS solution to derive approximate IC50 values.

2.2.4.8. Confocal Laser Scanning Microscopy

MDA-MB-231 cells were seeded on 8-well chamber slides (Nunc™ Lab-Tek™ II Chamber Slide™ System, Thermo Fisher Scientific,

Waltham, MA, USA) at a density of 3×10^4 cells per well and incubated overnight. Albumin nanoparticles encapsulating Cy5.5-NHS ester dye (Lumiprobe, Hallandale Beach, FL, USA) were prepared by adding the fluorophore instead of DOX during the desolvation process described in Section 4.2 (Cy5.5-Alb-NPs). On the next day, the cells were treated with various concentrations of Cy5.5-labeled and DOX-loaded albumin nanoparticles and were further incubated for a varying period. Once incubation was completed, the cells were fixed for 15 min with 4% formaldehyde and counter-stained with 4′,6-diamidino-2-phenylindole dyes (DAPI, Thermo Fisher Scientific, Waltham, MA, USA). During the fixation and staining processes, the cells were washed with fresh PBS. The images were acquired using a confocal microscope (Carl Zeiss, Inc., Oberkochen, Germany), using the excitation/emission wavelengths of 358/461, 470/595, and 684/710 nm for DAPI, DOX, and Cy5.5, respectively.

2.2.4.9. In Vivo Study

Immunocompetent female BALB/c mice and immunodeficient BALB/c nude mice that were 6–8 weeks old were purchased from Orient Bio (Seoul, Korea) for the toxicity and efficacy studies, respectively. The mice were acclimated for a week before the start of the study and were maintained at standard conditions in specific pathogen-free (SPF)

environments: 25 ± 2 °C temperature, 50 ± 10% relative humidity, and 12 h light/12 h dark. All mice were fed with sterilized standard mouse chow and water ad libitum. After the acclimatization periods, 1 × 106 MDA-MB-231 cells suspended in Matrigel (Corning, Tewksbury, MA, USA) were injected into the right flank regions of the nude mice. Once the tumor volume had reached ~150 mm^3, the mice were randomly sorted for the treatment. The tumor sizes were monitored with a digital caliper, and the volumes were calculated according to the formula $width^2$ × length × 0.5. All the in vivo protocols (Approval Number: BA1906-275/046-01) were verified according to the guidelines of the Seoul National University Bundang Hospital.

2.2.4.10. Ultrasound Treatment Protocols

A focused ultrasound system (VIFU 2000®, Alpinion Medical Systems, Seoul, Korea) was used for focused ultrasound (FUS) treatments: a 1.1 MHz single-element, spherically focused transducer with a central circular opening of 40 mm in diameter, creating a focal zone of 1.3 × 1.3 × 9.2 mm with a center frequency of 1.1 MHz at −6 dB, was controlled with a 3D target position system and ultrasound guidance to precisely deliver therapeutic ultrasound to the target. A degassing chamber was used to ensure that gas levels in the system were kept to a minimum (≤ 4 ppm) during the treatment. After injecting the mice with therapeutic

formulations (drug + microbubbles), pulsed FUS beams with the acoustic parameters of a 1.1 MHz frequency, 20 watts of power, a 40 Hz pulse repetition frequency, a 5% duty cycle, 5 s of ultrasound exposure per spot, and a 2 mm spot distance were applied at the tumor.

2.2.4.11. Biodistribution and IVIS Spectrum

Albumin nanoparticles encapsulating Cy5.5 dyes (Cy5.5-Alb-NPs) were prepared according to the protocol described in Section 4.9. Four experimental groups—(i) negative control injected with saline, (ii) Cy5.5-Alb-NPs, (iii) Cy5.5-rAlb-NPs, and (iv) Cy5.5-Alb-NPs + MB + FUS—were prepared. For the treatments, 200 μL amounts were injected intravenously into the MDA-MB-231 tumor-bearing mice. After 24 h, the mice were sacrificed and the Cy5.5 fluorescence signals from the tumors were analyzed using the In Vivo Imaging System (PerkinElmer, Waltham, MA, USA).

2.2.4.12. Experimental Groups and Protocols for Efficacy Study

The experimental groups for the efficacy study were defined as follows: (i) negative control injected with saline, (ii) DOX (2 mg/kg), (iii) sDOX only (2 mg/kg), (iv) rDOX only (2 mg/kg), (v) MB + FUS, (vi) sDOX + MB + FUS, and (vii) rDOX + MB + FUS. Before the treatment, intraperitoneal general anesthesia was administered using a mixture of 30 mg/kg Zoletil and 10 mg/kg Rompun 2%. All experimental groups

received their treatments intravenously, and those that concurrently received ultrasound treatment were additionally administered with 200 μL of SonoVue (1×10^8 MB/mL) immediately after the injection of the respective treatments. Each group received five treatments on Days 3, 7, 10, 14, and 17, and the tumor sizes were monitored biweekly for up to 4 weeks after the final treatment.

2.2.4.13. Experimental Groups and Protocols for Toxicity Study

The experimental groups for the acute toxicity study were defined as follows: (i) negative control injected with saline, (ii) DOX (10 mg/kg), (iii) DOX (20 mg/kg), (iii) DOX (30 mg/kg), (iv) rDOX (50 mg/kg DOX), (v) rDOX (75 mg/kg), (vi) rDOX (100 mg/kg), and (vii) rDOX (200 mg/kg). Each group received a single intravenous injection of 200 μL of the respective treatment. The mice were monitored for two weeks following the injection, and their weights and conditions were recorded at Days 2, 3, 7, 13, and 14 post-injection. At Day 14, the surviving mice were sacrificed, and their organs—liver, lungs, spleen, kidneys, and heart—were collected for further analysis.

2.2.5. Conclusion

In this work, human serum albumin was crosslinked using GTA to form uniform, spherical nanoparticles with unique abilities to load DOX, a widely used anticancer drug. In addition, we further modified this nanoformulation by using reducing agents to remove unreacted aldehydes from the surface, minimizing the potential toxicity associated with non-specific interactions enhancing the controlled release of the drug payload upon the external trigger. Furthermore, focused ultrasound was applied to enhance the accumulation of nanoparticles at the targeted local tumor, allowing DOX-dependent cancer cell death and superior tumor inhibitory effects compared to those achieved with the free drug or DOX-loaded, non-reduced albumin nanoparticle formulations. Additionally, we were able to observe a higher safety margin, highlighted by a much-improved maximum tolerated dose and reduced cardiac stress. Accordingly, the development of albumin-based nanoparticles holds great potential for anticancer therapy, and we believe further optimization of the platform could lead their way into clinical settings.

References

[1] Siegel, R.L.; Miller, K.D.; Jemal, A. Cancer statistics. CA Cancer J. Clin. 2020, 70, 7–30.

[2] Waks, A.G.; Winer, E.P. Breast Cancer Treatment: A Review. JAMA 2019, 321, 288–300.

[3] Iqbal, N.; Iqbal, N. Human Epidermal Growth Factor Receptor 2 (HER2) in Cancers: Overexpression and Therapeutic Implications. Mol. Biol. Int. 2014, 2014, 852748.

[4] Zeichner, S.B.; Terawaki, H.; Gogineni, K. A Review of Systemic Treatment in Metastatic Triple-Negative Breast Cancer. Breast Cancer (Auckl.) 2016, 10, 25–36.

[5] Cardoso, F.; Bedard, P.L.; Winer, E.P.; Pagani, O.; Senkus-Konefka, E.; Fallowfield, L.J.; Kyriakides, S.; Costa, A.; Cufer, T.; Albain, K.S.; et al. International guidelines for management of metastatic breast cancer: Combination vs sequential single-agent chemotherapy. J. Natl. Cancer Inst. 2009, 101, 1174–1181.

[6] Joensuu, H.; Holli, K.; Heikkinen, M.; Suonio, E.; Aro, A.R.; Hietanen, P.; Huovinen, R. Combination chemotherapy versus single-agent therapy as first- and second-line treatment in metastatic breast cancer: A prospective randomized trial. J. Clin. Oncol. 1998, 16, 3720–3730.

[7] An, F.F.; Zhang, X.H. Strategies for Preparing Albumin-based Nanoparticles for Multifunctional Bioimaging and Drug Delivery. Theranostics 2017, 7, 3667–3689.

[8] Storp, B.; Engel, A.; Boeker, A.; Ploeger, M.; Langer, K. Albumin nanoparticles with predictable size by desolvation procedure. J.

Microencapsul. 2012, 29, 138–146.

[9] Moon, H.; Kim, H.; Sim, C.; Lee, M.; Chang, J.H.; Lee, H.J.; Kim, H. Non-Invasive Tumor Therapy with Indocyanine Green and Paclitaxel Doubly Loaded Nanoparticles Using Photoacoustic Imaging. Sci. Adv. Mater. 2017, 9, 1177–1186.

[10] Jahanban-Esfahlan, A.; Dastmalchi, S.; Davaran, S. A simple improved desolvation method for the rapid preparation of albumin nanoparticles. Int. J. Biol. Macromol. 2016, 91, 703–709.

[11] Lee, H.; Jang, Y.; Park, S.; Jang, H.; Park, E.J.; Kim, H.J.; Kim, H. Development and evaluation of a CEACAM6-targeting theranostic nanomedicine for photoacoustic-based diagnosis and chemotherapy of metastatic cancer. Theranostics 2018, 8, 4247–4261.

[12] Wilhelm, S.; Tavares, A.J.; Dai, Q.; Ohta, S.; Audet, J.; Dvorak, H.F.; Chan, W.C.W. Analysis of nanoparticle delivery to tumours. Nat. Rev. Mater. 2016, 1, 16014.

[13] Burgess, A.; Hynynen, K. Microbubble-Assisted Ultrasound for Drug Delivery in the Brain and Central Nervous System. Adv. Exp. Med. Biol. 2016, 880, 293–308.

[14] Arvanitis, C.D.; Askoxylakis, V.; Guo, Y.; Datta, M.; Kloepper, J.; Ferraro, G.B.; Bernabeu, M.O.; Fukumura, D.; McDannold, N.; Jain, R.K. Mechanisms of enhanced drug delivery in brain metastases with focused ultrasound-induced blood-tumor barrier disruption. Proc. Natl. Acad. Sci. USA 2018, 115, E8717–E8726.

[15] Li, T.; Wang, Y.N.; Khokhlova, T.D.; D'Andrea, S.; Starr, F.; Chen, H.; McCune, J.S.; Risler, L.J.; Mashadi-Hossein, A.; Hingorani, S.R.; et al. Pulsed High-Intensity Focused Ultrasound Enhances Delivery of Doxorubicin in a Preclinical Model of Pancreatic Cancer. Cancer Res.

2015, 75, 3738–3746.

[16] Burke, C.W.; Hsiang, Y.H.; Alexander, E.T.; Kilbanov, A.L.; Price, R.J. Covalently linking poly(lactic-co-glycolic acid) nanoparticles to microbubbles before intravenous injection improves their ultrasound-targeted delivery to skeletal muscle. Small 2011, 7, 1227–1235.

[17] Lyon, P.C.; Gray, M.D.; Mannaris, C.; Folkes, L.K.; Stratford, M.; Campo, L.; Chung, D.Y.F.; Scott, S.; Anderson, M.; Goldin, R.; et al. Safety and feasibility of ultrasound-triggered targeted drug delivery of doxorubicin from thermosensitive liposomes in liver tumours (TARDOX): A single-centre, open-label, phase 1 trial. Lancet Oncol. 2018, 19, 1027–1039.

[18] Langer, K.; Balthasar, S.; Vogel, V.; Dinauer, N.; von Briesen, H.; Schubert, D. Optimization of the preparation process for human serum albumin (HSA) nanoparticles. Int. J. Pharm. 2003, 257, 169–180.

[19] Moseman, R.F. Chemical disposition of boron in animals and humans. Environ. Health Perspect. 1994, 102, 113–117.

[20] Carvalho, C.; Santos, R.X.; Cardoso, S.; Correia, S.; Oliveira, P.J.; Santos, M.S.; Moreira, P.I. Doxorubicin: The good, the bad and the ugly effect. Curr. Med. Chem. 2009, 16, 3267–3285.

[21] Mo, Steven, et al. "Ultrasound- Kalyanaraman, B.; Joseph, J.; Kalivendi, S.; Wang, S.; Konorev, E.; Kotamraju, S. Doxorubicin-induced apoptosis: Implications in cardiotoxicity. Mol. Cell. Biochem. 2002, 234–235, 119–124.

[22] Friedman, M.A.; Bozdech, M.J.; Billingham, M.E.; Rider, A.K. Doxorubicin cardiotoxicity. Serial endomyocardial biopsies and systolic time intervals. JAMA 1978, 240, 1603–1606.

[23] Yang, F.; Teves, S.S.; Kemp, C.J.; Henikoff, S. Doxorubicin, DNA torsion, and chromatin dynamics. Biochim. Biophys. Acta 2014, 1845, 84–89.

[24] Lu, Y.; Zhang, E.; Yang, J.; Cao, Z. Strategies to improve micelle stability for drug delivery. Nano Res. 2018, 11, 4985–4998.

[25] Doane, T.; Burda, C. Nanoparticle mediated non-covalent drug delivery. Adv. Drug Deliv. Rev. 2013, 65, 607–621.

[26] Zhang, Y.; Yang, C.; Wang, W.; Liu, J.; Liu, Q.; Huang, F.; Chu, L.; Gao, H.; Li, C.; Kong, D.; et al. Co-delivery of doxorubicin and curcumin by pH-sensitive prodrug nanoparticle for combination therapy of cancer. Sci. Rep. 2016, 6, 21225.

[27] Li, S.; Amat, D.; Peng, Z.; Vanni, S.; Raskin, S.; De Angulo, G.; Othman, A.M.; Graham, R.M.; Leblanc, R.M. Transferrin conjugated nontoxic carbon dots for doxorubicin delivery to target pediatric brain tumor cells. Nanoscale 2016, 8, 16662–16669.

[28] Zhang, X.; Li, L.; Li, C.; Zheng, H.; Song, H.; Xiong, F.; Qiu, T.; Yang, J. Cisplatin-crosslinked glutathione-sensitive micelles loaded with doxorubicin for combination and targeted therapy of tumors. Carbohydr. Polym. 2017, 155, 407–415.

[29] Fortuni, B.; Inose, T.; Ricci, M.; Fujita, Y.; Van Zundert, I.; Masuhara, A.; Fron, E.; Mizuno, H.; Latterini, L.; Rocha, S.; et al. Polymeric Engineering of Nanoparticles for Highly Efficient Multifunctional Drug Delivery Systems. Sci. Rep. 2019, 9, 2666.

[30] Jain, Ankit, et al. "Ultrasound-based triggered drug delivery to tumors." Drug delivery and translational research 8.1 (2018): 150-164.

[31] Tharkar, Priyanka, et al. "Nano-enhanced drug delivery and

therapeutic ultrasound for cancer treatment and beyond." Frontiers in Bioengineering and Biotechnology (2019): 324.

2.3. Antitumor Efficacy of Focused Ultrasound-MFL Nanoparticles Combination Therapy

2.3.1. Introduction

Breast cancer still remains one of the common cancers in women, being ranked as the second-highest cancer in terms of occurrence. Despite its rate of high incidence, breast cancer patients' 5-year survival rate is not the worst among cancers [1,2]. Although many efforts are spent in prevention and early diagnosis, patients often undergo mastectomy to remove one or both of their breasts and/or are treated with chemotherapeutic agents [3,4,5]. Classical chemotherapy relies on the systemic circulation and accumulation of cytotoxic chemical agents, which may not only reduce tumor growth but also damage normal cells as well [6,7]. Docetaxel, one of the most common drugs used against breast cancer, is normally administered in doses of 10–15 mg/kg in mice. Such a dosage is quite high when compared to other chemotherapeutics and therefore is known to cause detrimental side effects [8,9,10,11,12]. Therefore, researchers over the last few decades have been working on drug delivery techniques, including but not limited to production of vehicles that can carry and protect the therapeutic cargo and then subsequently release it at the target area to maximize drug efficacy while minimizing damage onto normal cells [13,14,15]. In this regard, the new

method to synthesize liposomal nanoparticles, known as membrane fusogenic liposomes (MFLs), was invented [16,17,18]. Not only they are bio-compatible, they are subjected to the enhanced permeability and retention (EPR) effect and also can be tailored to fit desired characteristics. The main strength of MFLs is that they can be used to deliver both hydrophobic and hydrophilic compounds to cellular membranes and cytosol through fusion of the liposomal surface with the cellular membranes. Similar to conventional liposomes, MFLs are biocompatible and allow minimization of the drug dosage. Furthermore, the size of MFLs can be tailored to be around 100 nm, which allows these nanoparticles to migrate to the target site via the EPR effect in diseases such as solid tumors and atherosclerosis. In addition, rather than entering the cell through the endosome–lysosome pathway, MFLs may fuse with the cellular membrane and maintain binding to the membrane for long period preventing from endocytosys, thereby efficiently delivering hydrophilic agents to target sites, and yielding a therapeutic effect. Finally, functional modification can be applied to the lipids that constitute MFLs for the further targeting effect, including but not limited to conjugation of targeting moieties such as antibodies or peptides [17,18].

Along with advances in these drug delivery techniques, the use of

ultrasound in drug delivery has been recently spotlighted [19]. Ultrasound can be applied as an external trigger to enhance drug delivery by the sonoporation effect [20,21]. Sonoporation is driven by the cavitation of microbubbles triggered by the ultrasound exposure. The repeated expansion and shrinkage of microbubbles, a phenomenon known as stable cavitation, creates microstreams that stress nearby cell membranes to induce disruption on vasculature. In addition, stronger ultrasound exposures eventually lead microbubbles to burst open. Known as inertial cavitation, this phenomenon creates pores of 100–300 nm on the cell membrane as the microbubble explodes and microjets and shock waves are generated [22]. This cavitation mechanism enhances drug delivery to the target area by improving uptake of drugs and drug vesicles [23,24]. In addition to normal ultrasound, focused ultrasound (FUS) has been proposed as another potential therapy option due to its unique ability to treat a specific region in the body without damaging nearby or intervening tissues and while also providing real-time monitoring of therapy [25].

In this study, we used a combination of FUS with MFLs containing a significantly lower amount of docetaxel and evaluated anti-cancer efficacy of this combination therapy in the MDA-MB-231 xenograft mouse model (Figure 2.3.1). MFLs loaded with 2 mg/kg of docetaxel

were successfully prepared and characterized based on different features, including cell cytotoxicity and stability. Furthermore, their effectiveness as anti-cancer agents was tested in combination with FUS.

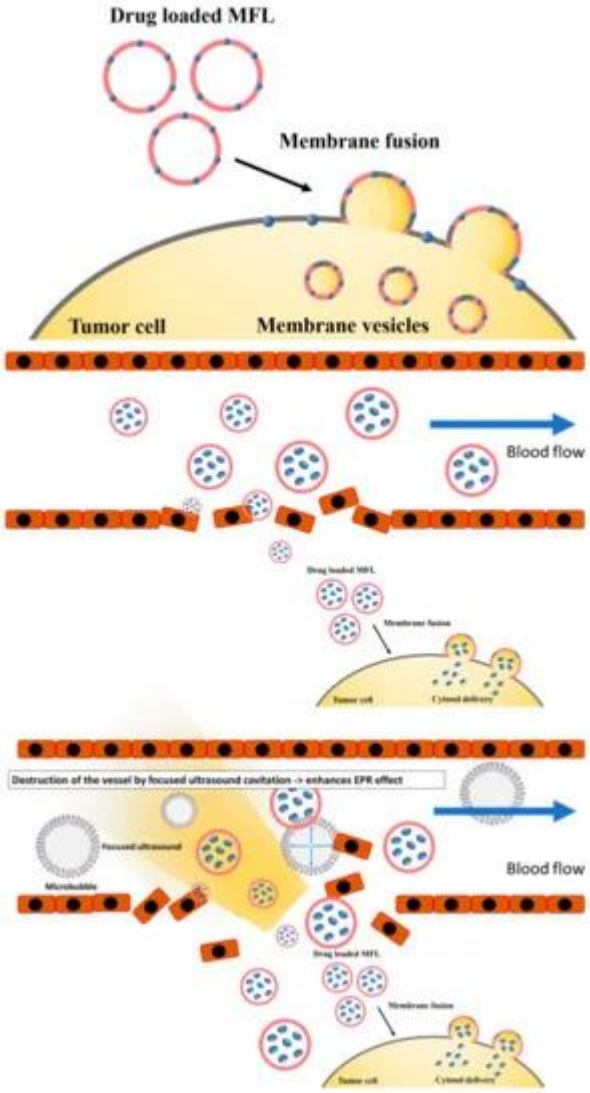

Figure 2.3.1. Graphical representation of membrane fusogenic liposomes (MFLs) and MFL-focused ultrasound.

2.3.2. Materials and Method

2.3.2.1. Materials

The 1,2-dimyristoyl-sn-glycero-3-phosphocholine (DMPC), 1,2-dioleoyl-3-trimethylammonium-propane (DOTAP), and 1,2-distearoyl-sn-glycero-3-phosphoethanolamine-N-[methoxy(polyethylene glycol)-2000] were received from Avanti Polar Lipids (Avanti Polar Lipids Inc., Alabaster, AL, USA). Acetonitrile, chloroform, and methanol were received from Sigma Aldrich (Sigma Aldrich, St. Louis, MO, USA). The Zetasizer Nano ZS90 was received from Malvern Instruments (Malvern Instruments Ltd., Malvern, UK), and the 1260 Infinity II LC system was received from Agilent Technologies (Agilent Technologies Inc., Santa Clara, CA, USA). Docetaxel was received from MedChemExpress (MedChemExpress LLC, Monmouth Junction, NJ, USA). The VIFU 2000® was received from Alpinion Medical systems (Alpinion Medical Systems Co., Ltd., Seoul, Korea). SonoVue® was bought from Bracco (Bracco Imaging, Milan, Italy).

2.3.2.2. Preparation of Docetaxel-Loaded MFLs

Liposomal formulations were prepared from 1,2-dimyristoyl-sn-glycero-3-phosphocholine (DMPC, Avanti Polar Lipids), 1,2-dioleoyl-3-trimethylammonium-propane (DOTAP, Avanti Polar Lipids), 1,2-distearoyl-sn-glycero-3-phosphoethanolamine-N-

[methoxy(polyethylene glycol)-2000] (DSPE-mPEG(2000), Avanti Polar Lipids), and docetaxel (Medchem express) using a film hydration/extrusion method according to the previous reports [17,18]. The molar ratios of DMPC, DOTAP, and DSPE-mPEG(2000) used for membrane fusogenic liposomes (MFLs) and non-fusogenic liposomes (NFLs) were 76.15:20:3.85 and 80:20:0, respectively. For liposomes loaded with fluorescent dye, 1,1´-dioctadecyl-3,3,3´,3´-tetramethylindocarbocyanine perchlorate (DiI, Invitrogen) was used. DiI-incorporated lipid film was prepared with 516.3 μg DMPC, 139.7 μg DOTAP, 108.0 μg DSPE-mPEG(2000) (for MFLs) or with 542.4 μg DMPC, 139.7 μg DOTAP (for NFLs), and 18.8 μg of DiI by dissolving them in organic solvents and then completely drying them overnight. The next day, the lipid film was hydrated using phosphate-buffered saline and then extruded through 100 nm membrane pores. For liposomes loaded with docetaxel, docetaxel was incorporated into the membrane of the liposomes using the hydration protocol. The docetaxel-incorporated lipid film was prepared with 516.3 μg DMPC, 139.7 μg DOTAP, 108.0 μg DSPE-mPEG(2000), and 40.39 μg of docetaxel by dissolving them in organic solvent and then completely drying them overnight. Lipid film was hydrated using phosphate-buffered saline and then extruded through 100 nm membrane pores. Docetaxel-loaded MFLs were stored at 4 °C

until further use.

2.3.2.3. Characterization of MFLs

Hydrodynamic size, polydispersity, and zeta potential of prepared liposomes were measured using the dynamic light scattering (DLS) method (Zetasizer Nano ZS90; Malvern Instruments, Malvern, UK). In order to obtain the final concentration of docetaxel in liposomes, docetaxel concentrations were measured by high performance liquid chromatography (HPLC) (1260 Infinity II LC system; Agilent Technologies, Santa Clara, CA, USA). A total of 100 μL of the docetaxel-loaded MFL solution was prepared and lyophilized (Modulspin 31; Hanil Science Medical, Korea). Then, it was suspended with 1 mL of methanol and sonicated for 10 min using a bath sonicator. After centrifugation at 15,000 rpm for 15 min, 500 μL of the supernatant was collected, and docetaxel remaining in the supernatant was analyzed by HPLC. The chromatographic conditions were as follows: Chromatographic separation was performed on a reversed phase C18 column. The compositions of the mobile phase were Acetonitrile/water (65:35, v/v) at a flow rate of 1 mL/min. Detection was taken at the wavelength of 230 nm. Encapsulation efficiency was calculated as the ratio of the amount of docetaxel into liposomes to the initial amount of drug. To test the stability of loaded cargos, the absorbance and fluorescence of DiI-loaded

MFLs were measured using a UV–Vis spectrophotometer and spectrofluorometer (Molecular Devices, San Jose, CA, USA) (λex = 530 nm and λem = 570 nm in fluorescence measurements). DiI-loaded MFL solution was filtered by centrifugal filter units (100 K MWCO, Millipore, MA, USA) to remove the leakage of DiI from the liposome at each time point. Fluorescence quantification was normalized by absorbance of lipids, and the remaining amounts of DiI were calculated.

2.3.2.4. Cell Culture

Human triple negative breast cancer cell line MDA-MB 231 cells were cultured in RPMI-1640 cell culture medium supplemented with 10% heat inactivated fetal bovine serum (FBS), 100 IU/mL penicillin, 100 mg/mL streptomycin, and 2 mM L-glutamine. Cultures were maintained in a humidified atmosphere with 5% CO_2 at 37 °C. Cells were sub-cultured twice a week, with a seeding density of about 2×10^3 cells/mL. Cell viability was determined by the trypan blue dye exclusion method.

2.3.2.5. In Vitro Fluorescence Cellular Imaging

To observe membrane fusogenicity of liposomes, 2×10^4 cells of MDA-MB-231 cells were treated with medium containing 280 μM of MFLs and NFLs loaded with fluorescent DiI for 15 min and further incubated for 30 min to 6 h at 37 °C. Cells were washed with PBS three times, stained with Hoechst 33342, and imaged using confocal

microscopy (Nikon Instrument Inc., Tokyo, Japan).

2.3.2.6. Cell Viability-Assay

Cellular viability was examined using the MTT assay method. MDA-MB-231 cells were seeded to 96-well plates at a density of 2×10^3 cells per well and left overnight in the incubator. The next day, these cells were treated with free docetaxel, MFLs, and docetaxel-loaded MFLs and were incubated for 48 h. Cells were then removed from the incubator, and their viability was evaluated using the MTT solution according to the manufacturer's instruction.

2.3.2.7. In Vivo Study

The antitumor activity was evaluated using the MDA-MB-231 tumor-bearing BALB/C nude mouse model, which was established by a subcutaneous inoculation with the MDA-MB-231 cell suspension (1×10^6 cells per mouse) into the right flank region of 4-week BALB/C nude female mice. After the tumor volume reached ~150 mm^3, the mice were randomly sorted for treatment. Before the therapy, we examined MB + FUS to confirm that MB + FUS alone did not have anti-cancer effect. The experimental groups were defined as follows: (i) negative control, (ii) docetaxel only (2 mg/kg), (iii) docetaxel-loaded (DTX)-MFLs only (2 mg/kg), (iv) DTX-MFLs + MB + FUS. Sonovue MBs were injected with 1 mL per injection (1×10^8 Sonovue MBs per mL). The tumor size

was measured with a digital caliper, and volumes were calculated as width^2 × length × 0.5. The cancer therapeutic analysis was determined based on tumor sizes from the date of first injection for each groups.

2.3.2.8. Focused Ultrasound (FUS) Treatment Parameters

A pre-clinical FUS system (VIFU 2000®, Alpinion Medical systems, Seoul, Korea) was used for ultrasound treatment. The therapeutic transducer used was a 1.1 MHz single-element spherical-focused transducer with a central circular opening of 40 mm in diameter. FUS exposure was performed after reaching the degassing level of ≤ 4 ppm. Prior to FUS treatment, intraperitoneal general anesthesia was administered using a mixture of 30 mg/kg zolazepam (Zoletil®, Virbac, Carros, France) and 10 mg/kg xylazine hydrochloride (Rompun 2%, Bayer Korea, Seoul, Korea). The tumor-bearing mice were set on a heating pad, and the target tumor was positioned at the center of the therapeutic transducer's focal zone according to ultrasound guidance (E-CUBE 9®, Alpinion Medical Systems). The focal zone was 1.3 mm × 1.3 mm × 9.2 mm with a center frequency of 1.1 MHz at −6 dB. For precise targeting, the FUS system was equipped with 3D target position control (x-, y-, and z-axis). Pulsed FUS beams insonated the tumor and moved automatically at 2 mm space intervals to cover the entire tumor. The following acoustic parameters were used: frequency, 1.1 MHz; 20

Watts; pulse repetition frequency, 40 Hz; duty cycle, 5%; treatment duration, 5 s per spot; spot distance, 2 mm.

2.3.3. Results and Discussion

2.3.3.1. Characterization of MFLs

On the basis of previous reports [17,18], three types of lipids were used for synthesizing liposomes used in this study, and their physical characteristics are described in Table 2.3.1. Membrane fusogenic liposomes (MFLs) and docetaxel-loaded membrane fusogenic liposomes (DTX-MFLs) were first synthesized by the film hydration/extrusion method previously reported elsewhere, of which lipid compositions are listed in the Table 2.3.2. To measure the drug-loading efficiency, a loaded amount of docetaxel in 1 μmol of lipid was calculated from the value of the area under curve of the absorption peak of docetaxel by HPLC and the standard curve of the docetaxel concentration in methanol. As a result, it was calculated that 22.23 μg of docetaxel was loaded in 1 μmol of lipid, suggesting of moderate encapsulation efficiency (55.04%, Table 2.3.2).

Table 2.3.1. Information of lipids used for synthesizing liposomal formulations.

Full Name	Abbreviation	Lipid Chain	Transition Temperature	Structure
1,2-dimyristoyl-sn-glycerol-3-phosphocholine	DMPC	14:0	24 °C	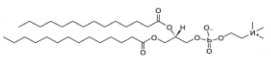
1,2-dioleoyl-3-trimethlammonium-propane	DOTAP	18:1	<5 °C	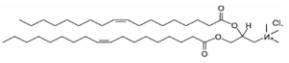
1,2-distearoyl-sn-glycerol-3-phosphoethanolamine-*N*-[methoxy(polyethylene glycol)-2000]	DSPE-mPEG(2000)	18:0	12.8 °C	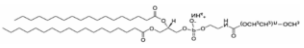

Table 2.3.2. Lipid compositions and drug-loading efficiency of liposomes.

Lipid Composition (Molar Ratio)					
Nanoparticle	**DMPC**	**DOTAP**	**DSPE-mPEG(2000)**	**Docetaxel**	**Drug Loading Efficiency (%)**
NFL	80	20	0	—	—
MFL	76.15	20	3.85	—	—
DTX-MFL	76.15	20	3.85	0.05	55.04

Next, the physical characteristics of liposomal nanoparticles were measured. Hydrodynamic size of MFLs was measured to be 127.9 ± 2.2 nm according to the dynamic light scattering (DLS) measurements, while the size of DTX-MFLs was measured to be 125.2 ± 3.9 nm (Figure 2.3.2a,b). Surface charges of the nanoparticles were also measured by zeta potential measurement in DLS. Zeta potential of MFLs and DTX-MFLs was measured to be +24.5 ± 1.3 mV and +22.3 ± 2.2 mV, respectively (Figure 2c). To test their stability, size, and polydispersity index (PDI), DTX-MFLs were monitored until 48 h after synthesis. We found that there were no significant changes in the sizes and PDI of DTX-MFLs after 48 h. (Figure 2.3.2d,e). To test the stability of loaded cargos, DiI was used as a model hydrophobic cargo. Absorbance and fluorescence of DiI-loaded MFLs were monitored until 48 h after synthesis. After 48 h, about 90% of initially loaded DiI was finally left in MFLs, and we observed no significant cargo leakage (Figure 2.3.2f).

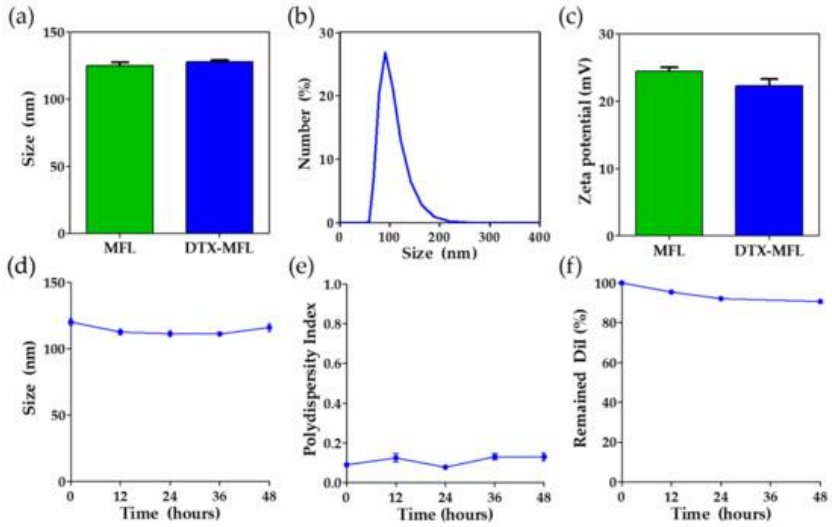

Figure 2.3.2. (a) Hydrodynamic sizes of MFLs and docetaxel-loaded (DTX)-MFLs as measured by dynamic light scattering (n = 4). (b) Distribution of hydrodynamic sizes of DTX-MFLs (n = 4). (c) Zeta potential of MFLs and DTX-MFLs (n = 6). (d) Particle size stability of DTX-MFLs up to 48 h. (e) Particle polydispersity index of DTX-MFLs up to 48 h. (f) Normalized fluorescence of remaining 1,1´-dioctadecyl-3,3,3´,3´-tetramethylindocarbocyanine perchlorate (DiI) in DiI-loaded MFLs up to 48 h. MFL and DTX-MFL denote membrane fusogenic liposomes and docetaxel-loaded membrane fusogenic liposomes. Data represent averages ± SD.

2.3.3.2. In Vitro Study

To evaluate the fusogenicity of MFLs, we first investigated whether MFLs could be transferred onto the membrane of target cells by fusion. Highly cationic non-fusogenic liposomes (NFLs) that are known to enter cells via endocytosis, the conventional pathway of nanoparticle uptake, were prepared for comparison (Table 2.3.2). MDA-MB-231 human breast cancer cells were treated with MFLs and NFLs loaded with hydrophobic fluorescent dye and DiI for 15 min and further incubated for 30 min to 6 h. As represented in Figure 2.3.3a, confocal microscopy revealed that DiI signals from the membrane of MFLs were efficiently transferred to the membrane of tumor cells. In contrast, cells treated with NFLs showed poor delivery of DiI onto the membranes, and observed DiI fluorescence was assumed to be transferred into subcellular compartments. After 1 h of incubation, cells treated with MFLs also showed delivery of DiI into the inner compartments. These results demonstrate that the liposomal membranes were successfully fused with cellular membranes, and MFLs were not attached to the outside of cellular membranes. Hydrophobic cargoes loaded in MFLs can enter the cytosol by incorporation into membranes of membrane vesicles (MVs), including exosomes and microvesicles. We speculate that the incorporation into the membrane of MVs can allow the enhanced

penetration of hydrophobic drug cargoes, since MVs are known to play a key role in intercellular migration of exogenous hydrophobic cargoes through multiple cell layers [18].

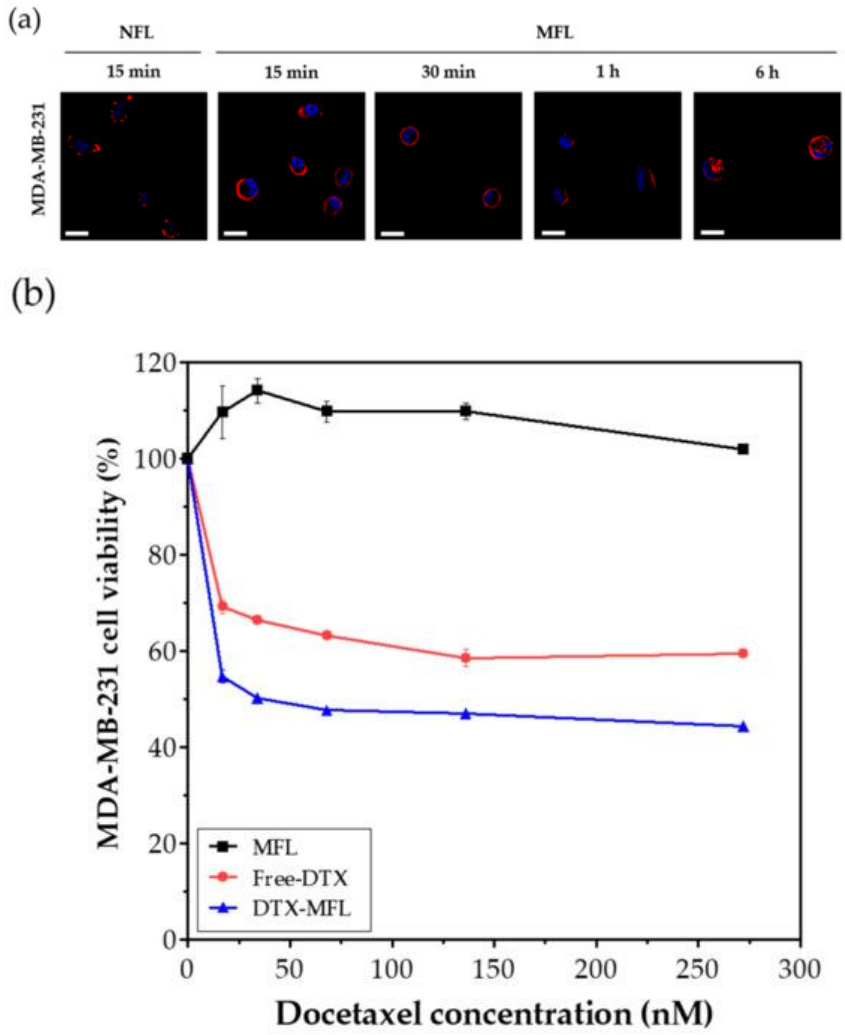

Figure 2.2.3. (a) Confocal fluorescent microscopic images of MDA-MB-231 cells treated with membrane fusogenic liposomes and non-fusogenic liposomes loaded with fluorescent dye DiI. Nuclei were stained with Hoechst (blue). Scale bars represent 20 μm. (b) Cell viability of MFLs, free-DTX, and DTX-MFLs at 24 h. MFL and NFL denote membrane fusogenic liposomes and non-fusogenic liposomes, respectively.

Next, docetaxel, MFLs, and DTX-MFLs were evaluated for their potential anti-cancer effects. Docetaxel and DTX-MFLs showed significant growth inhibition/IC50 values against MDA-MB-231 human breast cancer cell lines for up to 24 h (Figure 2.3.3b). The DTX-MFLs group seemed to reach IC50 at a concentration of 40 nM and showed slightly more anti-cancer effect on the cells than docetaxel alone, while the empty MFLs vehicles did not have any effect on cell viability. However, anti-cancer efficacy did not exceed 50% because of the low dosage of docetaxel used. These results suggest that low doses of docetaxel do not elicit sufficient anti-cancer effects; therefore, it is important to improve the drug delivery technique to design the release of drugs specifically at the tumor area.

2.3.3.3. In Vivo Study

To evaluate the enhanced combination therapy effect of DTX-MFLs and FUS, tumor volumes were measured following the intravenous injection of PBS (negative control), free docetaxel, DTX-MFLs, or a combination of DTX-MFLs with MB and FUS. BALB/C nude mice xenografted with MDA-MB-231 cells were observed until the tumor volume reached around ~150 mm^3 (N = 5 in each group). SonoVue® (Bracco, Milano, Italy) commercially available clinically employed microbubbles, were injected intravenously prior to the injection of DTX-MFLs (Figure 2.3.4b). Sonovue MBs were evaluated prior to the in vivo

therapy. The size of Sonovue MBs ranged from 1 to 10 μm, but over 90% of Sonovue MBs were in the range of 1 to 3 μm. The concentration of Sonovue MBs are around 1–5 × 10^8 per mL. Between microbubble and DTX-MFLs injections, time interval was less than a minute. After the injection, FUS application was subsequently performed within a minute. Five injection days (0, 4, 8, 12, and 16 days) were planned. We also confirmed that the MB + FUS group did not show an anti-cancer effect, so MB and FUS were therefore categorized as positive controls (Figure 2.3.4a). It was found that the DTX-MFLs + MB + FUS injected group had significant inhibition of MDA-MB-231 tumor growth ($p < 0.05$) when compared with the control and free docetaxel groups. In addition, the free docetaxel group alone at the dosage used in our study did not have anti-tumor effects, as its tumor growths were comparable to the control groups. These data confirmed that the drug dose is a critical factor in treating cancer and that the amount of metabolized and excreted drugs from circulation is too high to affect the tumor growths in vivo. On the other hand, DTX-MFLs + MB + FUS treatment groups showed that the combination of focused ultrasound with MFLs allowed efficient delivery of docetaxel to the tumor without significant side effects. The preferential anti-cancer effect of MFLs can be explained by their strong membrane fusogenic ability, which allows delivery of the therapeutic

payload at the target area while also minimizing drug loss on the way. Thus, despite using docetaxel at marginal amounts that do not affect tumor growth, DTX-MFLs were able to improve this issue so that even low doses could still exhibit a strong anti-cancer effect.

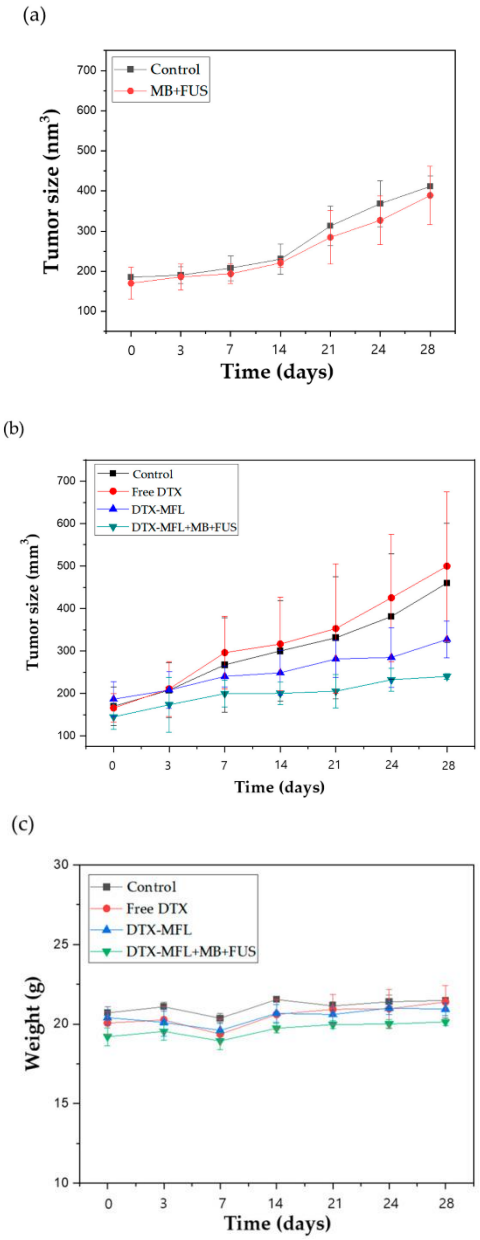

Figure 2.3.4. (a) In vivo efficacy of MB + FUS; (b) in vivo efficacy of docetaxel (free-DTX), docetaxel-loaded MFLs (DTX-MFLs), and docetaxel-loaded MFLs treated with microbubbles and focused ultrasound (DTX-MFLs + MB + FUS); (c) mouse body weight.

2.3.4 Conclusion

In summary, based on our data presented, MFLs as drug vehicles seemed to fuse well onto the cell membrane, allowing docetaxel to be delivered intracellularly to the tumor cells. Unlike free docetaxel, the DTX-MFLs' formulation was able to evade clearance and move into the tumor region for higher exposure to the target, thereby allowing strong anti-cancer effects to occur despite using docetaxel in amounts lower than conventionally administered. In addition, FUS-induced microbubble cavitation seemed to cause sonoporation of the blood vessels, enhancing the EPR effect and allowing the membrane fusogenic liposomes to penetrate the tumor area with higher efficiency. This strong anti-cancer mechanism therefore allows minimization of the side effects while greatly enhancing the drug efficacy at the same time.

References

[1] DeSantis, C.E.; Ma, J.; Goding Sauer, A.; Newman, L.A.; Jemal, A. Breast cancer statistics, 2017, racial disparity in mortality by state. CA Cancer J. Clin. 2017, 67, 439–448.

[2] Saika, K.; Sobue, T. Cancer statistics in the world. Gan to Kagaku ryoho. Cancer Chemother. 2013, 40,2475–2480.

[3] Pruthi, S.; Brandt, K.R.; Degnim, A.C.; Goetz, M.P.; Perez, E.A.; Reynolds, C.A.; Schomberg, P.J.; Dy, G.K.; Ingle, J.N. A multidisciplinary approach to the management of breast cancer, part 1: Prevention and diagnosis.Mayo Clin. Proc. 2007, 82, 999–1012.

[4] Forbes, J.F. The incidence of breast cancer: The global burden, public health considerations. Semin. Oncol.1997, 24, S20–S35.

[5] Stewart, B.W.; Kleihues, P. World Cancer Report; International Agency for Research on Cancer: Lyon, France, 2003.

[6] Jaiyesimi, I.A.; Buzdar, A.U.; Hortobagyi, G. Inflammatory breast cancer: A review. J. Clin. Oncol. 1992, 10, 1014–1024.

[7] Woo, J.C.; Yu, T.; Hurd, T.C. Breast cancer in pregnancy: A literature review. Arch. Surg. 2003, 138, 91–98.

[8] Smith, I.C.; Heys, S.D.; Hutcheon, A.W.; Miller, I.D.; Payne, S.; Gilbert, F.J.; Ah-See, A.K.; Eremin, O.; Walker, L.G.; Sarkar, T.K.; et al. Neoadjuvant chemotherapy in breast cancer: Significantly enhanced response with docetaxel. J. Clin. Oncol. 2002, 20, 1456–1466.

[9] Cortes, J.E.; Pazdur, R. Docetaxel. J. Clin. Oncol. 1995, 13, 2643–2655.

[10] Nabholtz, J.M.; Falkson, C.; Campos, D.; Szanto, J.; Martin, M.; Chan, S.; Pienkowski, T.; Zaluski, J.; Pinter, T.; Krzakowski, M. Docetaxel and doxorubicin compared with doxorubicin and cyclophosphamide as first-line chemotherapy for metastatic breast cancer: Results of a randomized, multicenter, phase III trial. J. Clin. Oncol. 2003, 21, 968–975.

[11] Keam, B.; Im, S.A.; Kim, H.J.; Oh, D.Y.; Kim, J.H.; Lee, S.H.; Chie, E.K.; Han, W.; Kim, D.W.; Moon, W.K. Prognostic impact of clinicopathologic parameters in stage II/III breast cancer treated with neoadjuvant docetaxel and doxorubicin chemotherapy: Paradoxical features of the triple negative breast cancer. BMC Cancer 2007, 7, 203.

[12] Tsai, S.M.; Lin, C.Y.;Wu, S.H.; Hou, L.A.; Ma, H.; Tsai, L.Y.; Hou, M.F. Side effects after docetaxel treatment in Taiwanese breast cancer patients with CYP3A4, CYP3A5, and ABCB1 gene polymorphisms. Clin. Chim. Acta 2009, 404, 160–165.

[13] Engels, F.K.; Mathot, R.A.; Verweij, J. Alternative drug formulations of docetaxel: A review. Anticancer Drugs 2007, 18, 95–103.

[14] Yang, M.; Ding, Y.; Zhang, L.; Qian, X.; Jiang, X.; Liu, B. Novel thermosensitive polymeric micelles for docetaxel delivery. J. Biomed. Mater. Res. A 2007, 81, 847–857.

[15] Zhang, P.; Zhang, H.; He,W.; Zhao, D.; Song, A. Luan Y Disulfide-linked amphiphilic polymer-docetaxel conjugates assembled redox-sensitive micelles for efficient antitumor drug delivery. Biomacromolecules 2016, 17, 1621–1632.

[16] Csiszár, A.; Hersch, N.; Dieluweit, S.; Biehl, R.; Merke, R.; Ho mann, B. Novel fusogenic liposomes for fluorescent cell labeling and membrane modification. Bioconjug. Chem. 2010, 21, 537–543.

[17] Lee, J.; Lee, H.; Goh, U.; Kim, J.; Jeong, M.; Lee, J.; Park, J.H. Cellular engineering with membrane fusogenic liposomes to produce functionalized extracellular vesicles. ACS Appl. Mater. Interfaces 2016, 8, 6790–6795.

[18] Lee, J.; Kim, J.; Jeong, M.; Lee, H.; Goh, U.; Kim, H.; Kim, B.; Park, J.H. Liposome-based engineering of cells to package hydrophobic compounds in membrane vesicles for tumor penetration. Nano Lett. 2015, 15,2938–2944.

[19] Kang, J.; Wu, X.; Wang, Z.; Ran, H.; Xu, C.; Wu, J.; Wang, Z.; Zhang, Y. Antitumor effect of docetaxel-loaded lipid microbubbles combined with ultrasound-targeted microbubble activation on VX2 rabbit liver tumors. J.Ultrasound Med. 2010, 29, 61–70.

[20] Moghimi, S.M.; Hunter, A.C.; Murray, J.C. Long-circulating and target-specific nanoparticles: Theory to practice. Pharmacol. Rev. 2001, 53, 283–318.

[21] Vancraeynest, D.; Havaux, X.; Pouleur, A.C.; Pasquet, A.; Gerber, B.; Beauloye, C.; Rafter, P.; Bertrand, L.; Vanoverschelde, J.L. Myocardial delivery of colloid nanoparticles using ultrasound-targeted microbubble destruction. Eur. Heart. J. 2005, 27, 237–245.

[22] Zarnitsyn, V.; Rostad, C.A.; Prausnitz, M.R. Modeling transmembrane transport through cell membrane wounds created by acoustic cavitation. Biophys. J. 2008, 95, 4124–4138.

[23] Lentacker, I.; Geers, B.; Demeester, J.; De Smedt, S.C.; Sanders, N.N. Design and evaluation of doxorubicin-containing microbubbles for ultrasound-triggered doxorubicin delivery: Cytotoxicity and mechanisms involved. Mol. Ther. 2010, 18, 101–108.

[24] Yin, T.; Wang, P.; Li, J.; Zheng, R.; Zheng, B.; Cheng, D.; Li, R.; Lai, J.; Shuai, X. Ultrasound-sensitive siRNA-loaded nanobubbles formed by hetero-assembly of polymeric micelles and liposomes and their therapeutic effect in gliomas. Biomaterials 2013, 34, 4532–4543.

[25] Bailey, M.; Khokhlova, V.A.; Sapozhnikov, O.A.; Kargl, S.G. Physical mechanisms of the therapeutic effect of ultrasound (a review). Acoust. Phys. 2003, 49, 369–388.

2.4. Sonodynamic therapy of Doxorubicin-Loaded Porphyrin-Liposome(DLPL)

2.4.1. Introduction

Although breast cancer often starts as local tumors, they may quickly spread outside the breast and become life-threatening depending on the subtype. According to data published by the American Cancer Society, breast cancer is one of the most common cancers that occur in women [1]. Breast cancer mainly occurs in middle-aged and older women [2]. Although breast cancer is one of the most studied cancers, its pathogenesis is still unknown [3]. However, there are many known risk factors that increase the chance of developing cancer relatively without causing cancer [4]. The standard of care treatment for local breast cancer is surgical excision of the lesion,[5]. For breast cancer, the efficacy of adjuvant therapy – including chemotherapy, radiation therapy, anti-hormonal therapy, and molecular targeted therapy – post surgery has been demonstrated [6,7]. These adjuvant therapies are accompanied as they can eliminate the remaining micrometastases, which could increase the overall survival and also lower the recurrence rates [8,9]. One of such adjuvant therapy options for breast cancer treatment is adjuvant chemotherapy [6,7]. Compared to other solid cancers, the use of chemotherapy in breast cancer patients can improve in survival rate

significantly [10,11]. In early breast cancer, chemotherapy alone may be sufficient as the adjuvant treatment option [12]. However, the side effects of anticancer drugs are well known, as they damage not only cancer cells but also normal cells, causing harmful effects [13]. Although some side effects induced by the chemotherapies are temporary, patients still complain of a lot of pain due to the pain and trauma during the chemotherapy regimen [13,14]. Side effects include nausea, vomiting, loss of appetite, diarrhea, oral inflammation, peripheral neurotoxicity such as numbness in the hands and feet, and permanent damage to the heart, lungs, kidneys, and reproductive organs [13,15].

To minimize this toxicity, a lot of treatment methods have been recently developed by loading anticancer drugs in liposomes or other various substances [16]. Doxil, a first-generation nanomedicine, is prepared in liposomal formulations to minimize the amount of the drug going to normal cells and is widely used in clinical practice as a drug to reduce side effects. In the case of Doxil, doxorubicin is loaded in a lipid-formed nanomaterial, and it protects anticancer drugs and maintains circulation in the human body for a long time, enabling treatment and reducing side effects [17,18,19].

Numerous materials suitable for drug delivery are currently being developed and are tested for improving the efficacy and minimizing the

side effects [16]. Along with the development in the materials side, drug delivery technology using ultrasound has also been under active investigation [20]. Cavitation is induced through ultrasound and ultrasound contrast material, and the strong pressure and high temperature created is used to destroy the drug carrier and thus cause drug release at the vicinity of cancer tissue [21,22]. However, one disadvantage of this method is attributed to the fact that the contrast agent and the drug delivering nanoparticles are strongly dependent on each other, and the results may vary each time the treatment is performed because of the poor stability of the contrast agents [23]

Therefore, many studies have been conducted to further increase the sensitivity toward ultrasound without the use of contrast agents. Among the different methods, liposomes based on porphyrin-lipids can be utilized to serve the purpose [24,25].

Using the properties of the porphyrin-lipids that make up most of the liposome, they not only generate ROS by sonosensitizer but also induces lipid peroxidation, which then subsequently cause the breakdown of the liposomal structure and drug release [25]. In particular, the double-bonded liposome in which porphyrin and lipid are combined is critical for the proposed mechanism [25,26]. Accordingly, we have developed Doxorubicin-Loaded Porphyrin Liposome (DLPL) using the porphyrin-

lipid as the core material, and measured drug release upon ultrasound irradiation. Also, we studied the in vitro and in vivo efficacy.

2.4.2. Materials and Methods

2.4.2.1. Reagents and Equipment

1,2-Distearoyl-sn-glycero-3-phosphocholine (DSPC; C18:0), [N-(carbonyl-methoxypolyethylene glycol-2000)-1,2-distearoyl-sn-glycero-3-phosphoethanolamine, sodium salt] (DSPE-mPEG2000), and 1,2-dioleoyl-sn-glycero-3-phosphoethanolamine (DOPE; C18:1) were purchased from Lipoid AG (Steinhausen, Switzerland). Doxorubicin (DOX) was purchased from Gemini Pharmaceuticals Inc. (NY, USA). Cholesterol, ammonium sulfate, hydrochloric acid, sodium hydroxide, 1-(4,5-Dimethylthiazol-2-yl)-3,5-diphenylformazan, thiazolyl blue formazan (MTT), and L-histidine were purchased from Sigma-Aldrich (MO, USA). Sucrose was purchased from CheilJedang (Seoul, Korea). Oasis HLB 3 cc Vac Cartridge (Solid-phase extraction column; SPE column) was purchased from Waters (MA, USA).Hemin was purchased from Sigma-Aldrich (MO, USA)

2.4.2.2. Preparation of Liposome and DLPL

The lipid composition of liposome, which was obtained from a pilot study, was DSPC/DSPE-PEG/cholesterol/DOPE. liposome was fabricated by ethanol injection followed by extrusion. Briefly, 1.47 mg

of DSPC, 2.62 mg g of DSPE-PEG, 2.17 mg of cholesterol, 9.73 mg of DOPE and 200 μg of porphyrin were dissolved in 1 mL of ethanol. The organic phase was gently heated to 60 °C to dissolve the lipid components. Then, the lipid-containing ethanol was injected into 4 mL of 250 mM ammonium sulfate solution at 250 rpm. Multilamellar vesicles (MLVs) were assembled and dispersed during ethanol injection and downsized by serial extrusion cycles with polycarbonate filter pore sizes ranging from 200 to 80 nm, using a LIPEX® 800 mL Thermobarrel extruder (Evonik, Canada). The temperature of the vesicles was maintained at 50 °C during the extrusion. The dispersion of extruded liposomes was exchanged with pH 6.5, 10% sucrose, and 10 mM histidine buffer using a 12–14-kDa dialysis membrane. The ammonium gradient across the liposomal membrane was generated by exchanging ammonium sulfate to the buffer. DOX was encapsulated into the intraliposomal aqueous phase using the remote loading method. DOX was added to the liposome dispersion at a ratio of 1:8 to liposomes and stirred at 37 °C for 2 h. DOX-loaded liposomes were diluted with a buffer solution so that the DOX concentration was 2 mg/mL, and stored at 2-8 °C.

2.4.2.3. Preparation of DOX-Liposome and DOX-PPR-Liposome

The lipid composition of liposome, which was obtained from a pilot

study, was DSPC/DSPE-PEG/cholesterol/DOPE. liposome was fabricated by ethanol injection followed by extrusion. Briefly, 1.50 g of DSPC, 2.66 g of DSPE-PEG, 2.20 g of cholesterol, 9.16 g of DOPE, and 0.50 g of MSPC were dissolved in 62.5 mL of ethanol. The organic phase was gently heated to 60 °C to dissolve the lipid components. Then, the lipid-containing ethanol was injected into 437.5 mL of 250 mM ammonium sulfate solution at 250 rpm. Multilamellar vesicles (MLVs) were assembled and dispersed during ethanol injection and downsized by serial extrusion cycles with polycarbonate filter pore sizes ranging from 200 to 80 nm, using a LIPEX® 800 mL Thermobarrel extruder (Evonik, Canada). The temperature of the vesicles was maintained at 50 °C during the extrusion. The dispersion of extruded liposomes was exchanged with pH 6.5, 10% sucrose, and 10 mM histidine buffer using a 12–14-kDa dialysis membrane. The ammonium gradient across the liposomal membrane was generated by exchanging ammonium sulfate to the buffer. DOX was encapsulated into the intraliposomal aqueous phase using the remote loading method. DOX was added to the liposome dispersion at a ratio of 1:8 to liposomes and stirred at 37 °C for 2 h. DOX-loaded liposomes were diluted with a buffer solution so that the DOX concentration was 2 mg/mL, and stored at 2-8 °C.

2.4.2.4. Preparation of DLL and DLPL

The lipid composition of liposome, which was obtained from a pilot study, was DSPC/DSPE-PEG/cholesterol/DOPE. liposome was fabricated by ethanol injection followed by extrusion. Briefly, 1.50 g of DSPC, 2.66 g of DSPE-PEG, 2.20 g of cholesterol, 9.16 g of DOPE, and 0.50 g of MSPC were dissolved in 62.5 mL of ethanol. The organic phase was gently heated to 60 °C to dissolve the lipid components. Then, the lipid-containing ethanol was injected into 437.5 mL of 250 mM ammonium sulfate solution at 250 rpm. Multilamellar vesicles (MLVs) were assembled and dispersed during ethanol injection and downsized by serial extrusion cycles with polycarbonate filter pore sizes ranging from 200 to 80 nm, using a LIPEX® 800mL Thermobarrel extruder (Evonik, Canada). The temperature of the vesicles was maintained at 50 °C during the extrusion. The dispersion of extruded liposomes was exchanged with pH 6.5, 10% sucrose, and 10 mM histidine buffer using a 12–14-kDa dialysis membrane. The ammonium gradient across the liposomal membrane was generated by exchanging ammonium sulfate to the buffer. DOX was encapsulated into the intraliposomal aqueous phase using the remote loading method. DOX was added to the liposome dispersion at a ratio of 1:8 to liposomes and stirred at 37 °C for 2 h. DOX-loaded liposomes were diluted with a buffer solution so that the DOX

concentration was 2 mg/mL, and stored at 2-8 °C.

2.4.2.5. Characterization of DLL and DLPL

The size distribution of DLL and DLPL was measured using dynamic light scattering (DLS; Nano ZS90, Malvern Panalytical, UK). The morphology of liposomes was examined using transmission electron microscopy (TEM). Specimens for TEM analysis at the National Center for Inter-University Facilities, Seoul National University (South Korea).

2.4.2.6. In vitro kinetics of DOX release from DLL and DLPL

To conduct the DOX release test of DLPL, plane wave ultrasound was irradiated by portable ultrasound for 5 min at a 3W/cm^2 and a continuous wave. Briefly, 2 mL of liposomal suspension ultrasound-irradiated was loaded onto a desalting column, followed by the addition of distilled water (DW) (0.5 mL). An additional 4 mL of DW was added to the desalting column and collected in a cuvette to measure the absorbance of liposomal DOX at 475 nm. Reduced absorbance compared with non-irradiated liposomes indicated the amount of DOX released.

2.4.2.7. Cell culture

Mouse breast cancer cell line 4T1-WT cells were acquired from the American Type Culture Collection (ATCC) and were cultured in Dulbecco's modified eagle medium (DMEM) supplemented with 10% heat-inactivated fetal bovine serum (FBS), 100 IU/mL penicillin, 100

mg/mL streptomycin, and 2 mM L-glutamine. Cultures were maintained in a humidified atmosphere with 5% CO_2 at 37°C and routinely tested for mycoplasma contamination. Cells were sub-cultured once they reached 80% confluency, determined by the trypan blue dye exclusion method.

2.4.2.8. Cell viability assay

The CellTiter 96® AQueous One Solution Cell Proliferation Assay (MTS) was used to assess the effects of nanoparticles on cell viability. 4T1-WT cells were seeded on 96-well plates at a density of 5×10^3 cells per well and incubated overnight. First, effects of ultrasound (-) groups on cell viability were evaluated by adding various concentrations of doxorubicin, DLL, DLPL to 4T1-WT cells. In addition, effects of ultrasound (+) groups were examined by same groups before into cells and incubating for up to 3 hrs for cell uptake process, wash with PBS, and incubating another 48 hrs. Cells were removed from the incubator at designated time points and their viability was evaluated against the phosphate-buffered saline (PBS) controls using the MTT solution to derive approximate IC50 values.

2.4.2.9. In vivo study

6-8 week old immunocompetent female immunodeficient BALB/c nude mice were purchased from Orient Bio (Seoul, South Korea) for

toxicity and efficacy studies, respectively. The mice were acclimated for a week before the start of the study and were maintained at standard conditions in specific pathogen-free (SPF) environments: 25 ± 2 °C temperature, 50 ± 10% relative humidity, and 12 h light/12 h dark. All mice were fed with sterilized standard mouse chow and water ad libitum. After acclimatization periods, 1×10^6 4T1-WT cells suspended in Matrigel (Corning, Massachusetts, US) were injected into the right flank region of the nude mice. Once the tumor volume had reached ~150mm3, the mice were randomly sorted for the treatment. The tumor size was monitored with a digital caliper and the volumes were calculated according to the formula $width^2\times length\times0.5$. All in vivo protocols were verified according to the guidelines of the Seoul National University Bundang Hospital.

2.4.2.10. Ultrasound treatment protocols

Portable ultrasound was used for ultrasound treatment. Once the intravenous injections of treatment formulations and microbubbles were completed, the tumor-bearing mice were set on a heating pad, and the target tumor was positioned at the center of the therapeutic transducer's focal zone according to ultrasound guidance. The following acoustic parameters were used: $3W/cm^2$; Continuous wave; 5 min ultrasound exposure.

2.4.2.11. Experimental groups and protocols for efficacy study

The experimental groups for acute toxicity study were defined as follows: (i) Negative control injected with saline (ii) DOX (iii) DLL (iii) DLPL (iv) US (v) DOX + US (vi) DLL + US and (vii) DLPL + US. Each group received 2mg/kg of DOX and a single intravenous injection of 200 μL of respective doses. The mice were monitored for two weeks following the injection, and their weights and conditions were recorded at days 3, 6, 9, 12, and 15 post-injections.

2.4.3. Results and Discussion

2.4.3.1. Schematics of DLL and DLPL mechanism

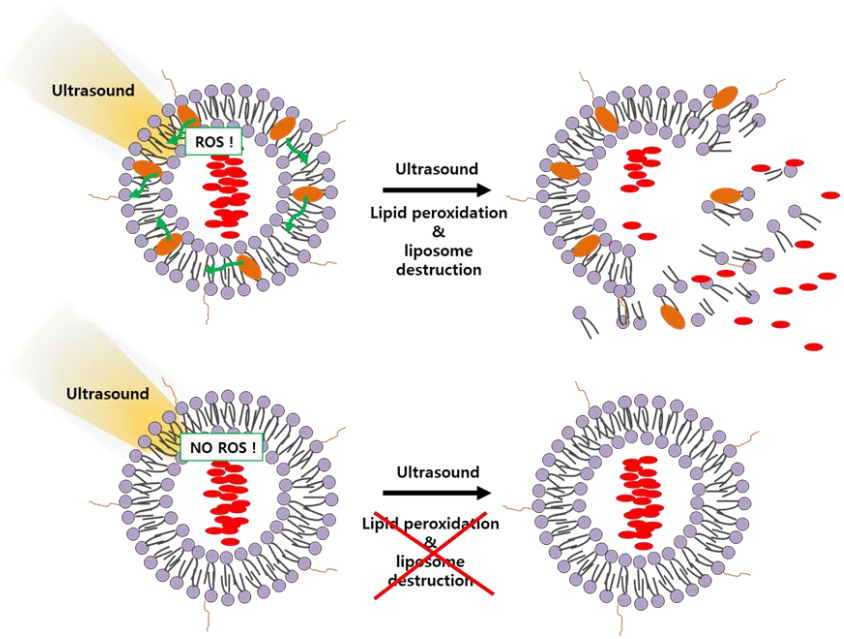

Figure 2.4.1. The proposed mechanism of action for DLL and DLPL by ultrasound irradiation. Expression that the degree of liposome breakage and drug release by ultrasound is different depending on the presence of sonosensitizer in the liposome.

2.4.3.2. Characterization of the DLL and DLPL

Porphyrin liposomes and general liposomes that are sensitive to ultrasound were prepared, and their size and PDI values were measured. The size came out as 132±21 nm and 134±18 nm, respectively, and it was confirmed that there was no significant difference between the two. And to confirm the size and shape, it was confirmed by taking a TEM picture. In addition, the stability of the liposome particles was checked up to 3 months, and it was confirmed that there was no significant change in size and no change in dox loading rate (Figure 2.4.2).

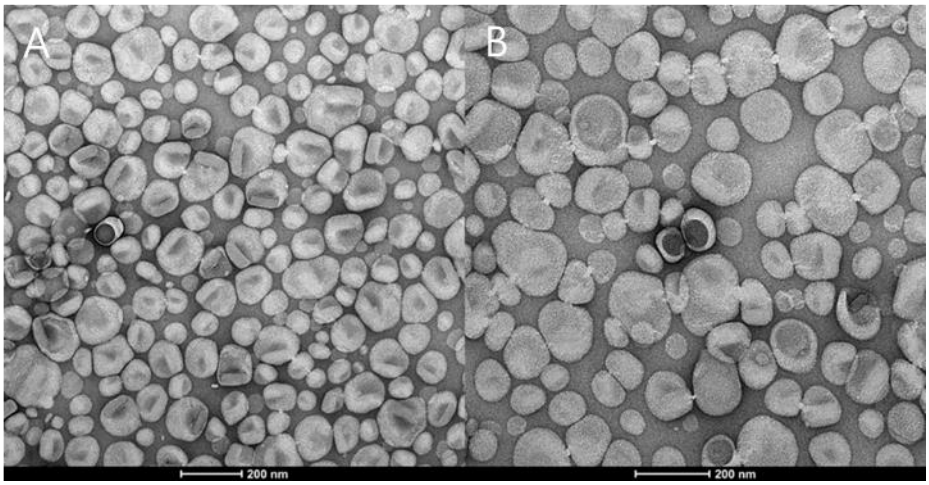

Figure 2.4.2. Images of DLL and DLPL obtained by transmission electron microscopy. Based on the images, the two nanoparticles had similar morphology and size. (A) TEM image of DLL (B) TEM image of DLPL.

2.4.3.3. In vitro release kinetics of DLL and DLPL

To compare the ultrasonic sensitivity of porphyrin liposomes and general liposomes, two types of liposomes were placed in a 24-well plate and irradiated with ultrasound. In the case of porphyrin liposomes, the release amount was more than 95%, and in the case of general liposomes, the release amount was less than 5%. It could be inferred that the double bond of DOPE composed mostly of both liposomes and ROS generated from porphyrins caused lipid peroxidation, resulting in lipid destruction.

Table 2.4.1. The loading efficiency and release ratio of doxorubicin from DLL and DLPL.

Material	Loading efficiency (%)	Release ratio (%)
DLL	97.1%	4.4%
DLPL	95.8%	86.4%

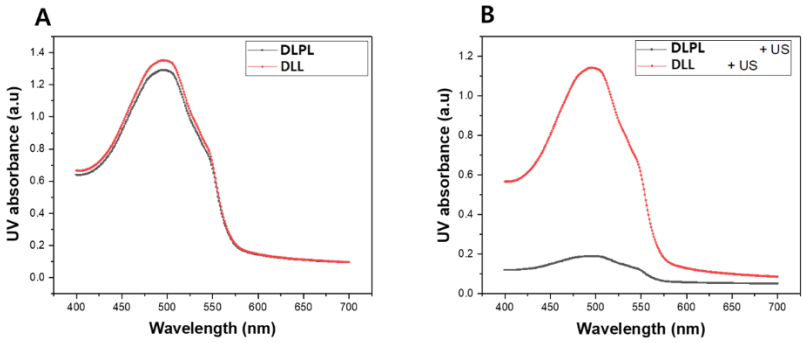

Figure 2.4.3. Doxorubicin release ratio data of UV spectrometer. (A) Release ratio of doxorubicin was measured from DLL and DLPL by UV spectrometer. (B) same experiment after US irradiation. UV absorption value was 475 nm in both experiments.

2.4.3.4. In vitro cell viability study

To confirm the ultrasound-induced cytotoxicity, the cytotoxicity was confirmed by MTT analysis using the 4T1 cell line (Figure 2.4.4). We compared porphyrin liposomes, porphyrin-free liposomes, and free DOX. Each group was divided into a group that was irradiated with ultrasound and a group that was not, and all groups were treated with cells at a concentration ranging from 2 to 10 μg/ml. There was no difference between porphyrin liposomes and normal liposomes in the group not exposed to ultrasound. Through this, it was possible to confirm the stability of the liposome, and it was confirmed that there was no DOX release. However, different results were obtained for the ultrasonically pretreated materials. The difference between porphyrin liposomes and normal liposomes was clearly seen, and it was confirmed that the ultrasonic waves destroyed the porphyrin liposomes and at the same time the DOX contained therein was released. Porphyrin liposomes at 6 μg/ml inhibited the survival rate of 4T1 cells by more than 50%, whereas normal liposomes were not inhibited at the same concentration.

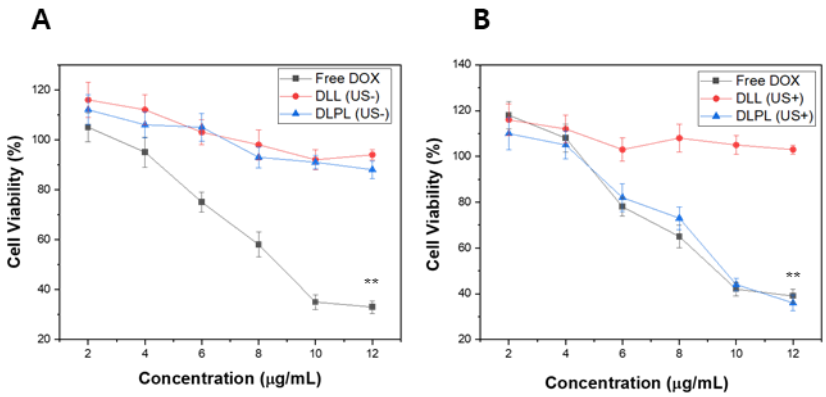

Figure 2.4.4. Cytotoxicity of DLL and DLPL in vitro. Both nanoaprticles were evaluated using 4T1-WT murine cancer cell line. (A) the cytotoxicity of DLL and DLPL without US irradiation. (B) the cytotoxicity of both nanoparticles with US irradiation. Values are mean ± SD (n = 6). * $p \leq 0.05$, ** $p \leq 0.01$.

2.4.3.5. In vivo efficacy

Also, we prepared animal experiments to evaluate the therapeutic index of the DLL and DLPL. Eight experimental groups bearing 4T1-WT murine breast cancer models were prepared: (i) negative control injected with saline, (ii) Free DOX (2 mg/kg), (iii) DLL (2 mg/kg), (iv) DLPL (2 mg/kg), (v) US, (vi) Free DOX + US, (vii) DLL + US, and (viii) DLPL + US. First, the ultrasound treatment group showed that there is not significant effect on the tumor growth, as the tumor growth in both the control group and the ultrasound only group was unchanged (Figure 2.4.5.A). Furthermore, while all formulations that contained DOX had significantly suppressed size of tumor. When DLPL was complemented with ultrasound, the therapeutic efficacy was maximized. It is also worth noting that all the protocols, including those that included DOX, did not induce significant changes in the weights of the mice (Figure 2.4.5.B).

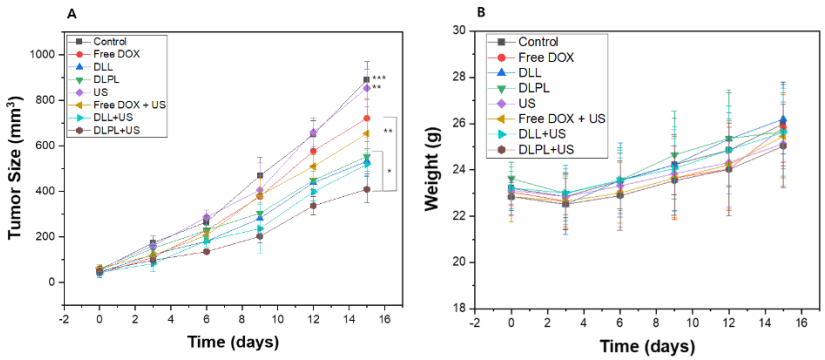

Figure 2.4.5. Efficacy of treatment protocols against tumor growth, and the changes in body weight. (A) The data was shown that the significant differences between the control and US groups and the treatment groups (DLL, DLPL, DLL+US, DLPL+US) were observed. A concentration equivalent of 2 mg/kg Doxorubicin was used per treatment. (B) No significant changes in the body weights of the different groups were observed. Values are mean ± SD (n = 5). * $p \leq 0.05$, ** $p \leq 0.01$, *** $p \leq 0.001$.

2.4.4. Conclusion

Sonosensitizer was loaded on liposome with unsatuated lipid (DOPE) to destroy particles through ultrasound and at the same time to release doxorubicin. It was confirmed that porphyrin, a well-known phososensitizer, generates ROS by ultrasound causing the breakdown of the liposome. When preparing the liposome, the porphysome prepared by conjugating the sonosensitizer to the lipid may require a lot of analysis and data for clinical applications. On the other hand, the utilization of liposomes and sonosensitizer that have already been approved for clinical use may accelerate the clinical translation. We believe that the porphyrin-based liposome is a promising material that can maintain the benefits of liposome-based anti-cancer drug vehicles that is the most used in clinical practice. Furthermore, with the drug release mechanism using sonosensitizers, we expect that this platform can be expanded for applications in a variety of cancer targets.

References

[1] DeSantis, Carol, et al. "Breast cancer statistics, 2013." CA: a cancer journal for clinicians 64.1 (2014): 52-62.

[2] Hery, C., et al. "Changes in breast cancer incidence and mortality in middle-aged and elderly women in 28 countries with Caucasian majority populations." Annals of oncology 19.5 (2008): 1009-1018.

[3] Van der Groep, Petra, Elsken Van Der Wall, and Paul J. Van Diest. "Pathology of hereditary breast cancer." Cellular oncology 34.2 (2011): 71-88.

[4] Tyrer, Jonathan, Stephen W. Duffy, and Jack Cuzick. "A breast cancer prediction model incorporating familial and personal risk factors." Statistics in medicine 23.7 (2004): 1111-1130.

[5] Sibbering, Mark, and Carol-Ann Courtney. "Management of breast cancer: basic principles." Surgery (Oxford) 34.1 (2016): 25-31.

[6] Kaur, H., et al. "Current Therapies and Novel Targets in Treatment of Breast Cancer." Systematic Reviews in Pharmacy 1.1 (2010).

[7] Abdulkareem, I. H., and I. B. Zurmi. "Review of hormonal treatment of breast cancer." Nigerian journal of clinical practice 15.1 (2012).

[8] Sakorafas, G. H., and Michael Safioleas. "Breast cancer surgery: an historical narrative. Part III. From the sunset of the 19th to the dawn of the 21st century." European Journal of Cancer Care 19.2 (2010): 145-166.

[9] Sarmiento, Juan M., et al. "Surgical treatment of neuroendocrine metastases to the liver:: a plea for resection to increase survival." Journal of the American College of Surgeons 197.1 (2003): 29-37.

[10] Hassan, M. S. U., et al. "Chemotherapy for breast cancer." Oncology reports 24.5 (2010): 1121-1131.

[11] Broët, Philippe, et al. "Short and long-term effects on survival in breast cancer patients treated by primary chemotherapy: an updated analysis of a randomized trial." Breast cancer research and treatment 58.2 (1999): 151-156.

[12] Bedard, Philippe L., Angelo Di Leo, and Martine J. Piccart-Gebhart. "Taxanes: optimizing adjuvant chemotherapy for early-stage breast cancer." Nature Reviews Clinical Oncology 7.1 (2010): 22-36.

[13] Kayl, Anne E., and Christina A. Meyers. "Side-effects of chemotherapy and quality of life in ovarian and breast cancer patients." Current opinion in obstetrics and gynecology 18.1 (2006): 24-28.

[14] Kwak, Minyoung, et al. "Prevalence and predictors of post-traumatic stress symptoms in adolescent and young adult cancer survivors: a 1-year follow-up study." Psycho-Oncology 22.8 (2013): 1798-1806.

[15] Goodman, Michelle. "Managing the side effects of chemotherapy." Seminars in oncology nursing. Vol. 5. No. 2. WB Saunders, 1989.

[16] Cho, Kwangjae, et al. "Therapeutic nanoparticles for drug delivery in cancer." Clinical cancer research 14.5 (2008): 1310-1316.

[17] Elbayoumi, Tamer A., and Vladimir P. Torchilin. "Tumor-specific antibody-mediated targeted delivery of Doxil® reduces the manifestation of auricular erythema side effect in mice." International journal of pharmaceutics 357.1-2 (2008): 272-279.

[18] Barenholz, Yechezkel Chezy. "Doxil®—the first FDA-approved nano-drug: lessons learned." Journal of controlled release 160.2 (2012):

117-134.

[19] Hubert, A., et al. "Doxil (Caelyx): an exploratory study with pharmacokinetics in patients with hormone-refractory prostate cancer." Anti-Cancer Drugs 11.2 (2000): 123-127.

[20] Tharkar, Priyanka, et al. "Nano-enhanced drug delivery and therapeutic ultrasound for cancer treatment and beyond." Frontiers in Bioengineering and Biotechnology (2019): 324.

[21] Mo, Steven, et al. "Ultrasound-enhanced drug delivery for cancer." Expert opinion on drug delivery 9.12 (2012): 1525-1538.

[22] Pitt, William G., Ghaleb A. Husseini, and Bryant J. Staples. "Ultrasonic drug delivery–a general review." Expert opinion on drug delivery 1.1 (2004): 37-56.

[23] Upadhyay, Awaneesh, and Sameer V. Dalvi. "Microbubble formulations: synthesis, stability, modeling and biomedical applications." Ultrasound in medicine & biology 45.2 (2019): 301-343.

[24] Serpe, Loredana, Federica Foglietta, and Roberto Canaparo. "Nanosonotechnology: the next challenge in cancer sonodynamic therapy." Nanotechnology Reviews 1.2 (2012): 173-182.

[25] Zhou, Yiming, Xiaolong Liang, and Zhifei Dai. "Porphyrin-loaded nanoparticles for cancer theranostics." Nanoscale 8.25 (2016): 12394-12405.

[26] Trendowski, Matthew. "The promise of sonodynamic therapy." Cancer and Metastasis Reviews 33.1 (2014): 143-160.

2.5. PMP(Porphyrin-Micelle-PSMA) Nanoparticles for Photoacoustic and Ultrasound Signal Amplification

2.5.1. Introduction

Prostate cancer is the second-most common cancer in men worldwide [1]. The 5-year survival rates are relatively high, allowing numerous treatment options depending on the patient's condition [2]. Active surveillance, where cancer progression is monitored without intervention, is regularly exercised during the early stages, while interventionist treatment options such as chemotherapy, radiation, hormone therapy, and radical prostatectomy are also practiced to prevent disease progression [3,4]. Nevertheless, these interventions often have serious side effects such as urinary incontinence and erectile dysfunction, affecting the quality of life for those receiving the treatment [5,6,7]. As such, theranostic options with early diagnosis and minimal side effects are preferred [8]. Currently, biopsies, prostate-specific antigen (PSA) tests, ultrasound, and magnetic resonance imaging (MRI) are used for prostate cancer diagnosis. Each method has its limitations: biopsies are often invasive and may cause discomfort; PSA tests and ultrasound imaging are prone to misdiagnosis and often require biopsy confirmation; MRI

imaging, while accurate, can be quite costly and is often used to complement the abovementioned methods [9,10,11,12,13,14,15]. As such, a minimally invasive, cost-efficient method to detect the disease in the early stages is strongly desired [16,17,18].

Porphyrin-based substances are currently being used in clinical practice [19,20,21,22,23]. For example, Visudyne is a porphyrin-based photosensitizer that is used to remove abnormal blood vessels in those with eye conditions such as macular degeneration [24,25,26]. Furthermore, due to their excellent biocompatibility and unique optical properties, porphyrin-based molecules are being actively investigated preclinically and clinically for cancer theranosis [27,28]. Accordingly, the optical properties of porphyrins have been maximized by employing them in photoacoustic (PA) imaging, where the molecules are excited by a laser to emit specific echogenic signals that are detected by ultrasound transducers. As PA imaging is extremely sensitive and minimally invasive, it has become a strong candidate for prostate cancer diagnosis [29,30,31].

To address the need for novel theranostic methods, we are reporting porphyrin-based micelles targeting the prostate-specific membrane antigen (PSMA) [32,33,34]. Identification of disease-specific biomarkers and targeting strategies have also greatly improved treatment

options by minimizing potential side effects [35,36,37]. Accordingly, PSMA is a well-established biomarker for advanced prostate cancer, as prostate tumors highly overexpress this antigen [38,39]. In addition to such active targeting, preparation of porphyrins in micelles would also enhance their stability and half-life in circulation, thereby greatly improving their therapeutic window by combining improved tumor accumulation capacities and active targeting methods. We were able to demonstrate the robustness of PA signals from the porphyrin micelles themselves, and their superior sensitivity and selectivity against PSMA-expressing tumors in a xenograft mouse model. All in all, we believe that the concept of porphyrin micelles may become a strong candidate for the next generation of theranosis in prostate cancer patients.

2.5.2. Results

2.5.2.1. Schematic of Porphyrin-Micelle-PSMA (PMP) Tumor Binding Phenomenon

A summary of PMP mechanisms is described in Figure 1. As depicted in the figure, PSMA in PMP nanoparticles determines the intensity of binding affinity in PC-3 and LNCaP cancer cells. In the case of PC-3 which does not have PSMA binding site, since the binding affinity of PMP is relatively low, the phenomenon of materials passing in the direction of the arrow increases. Conversely, in the case of LNCaP with

PSMA binding site, the amount of accession to cancer cells increases due to the effect of PSMA attached to PMP.

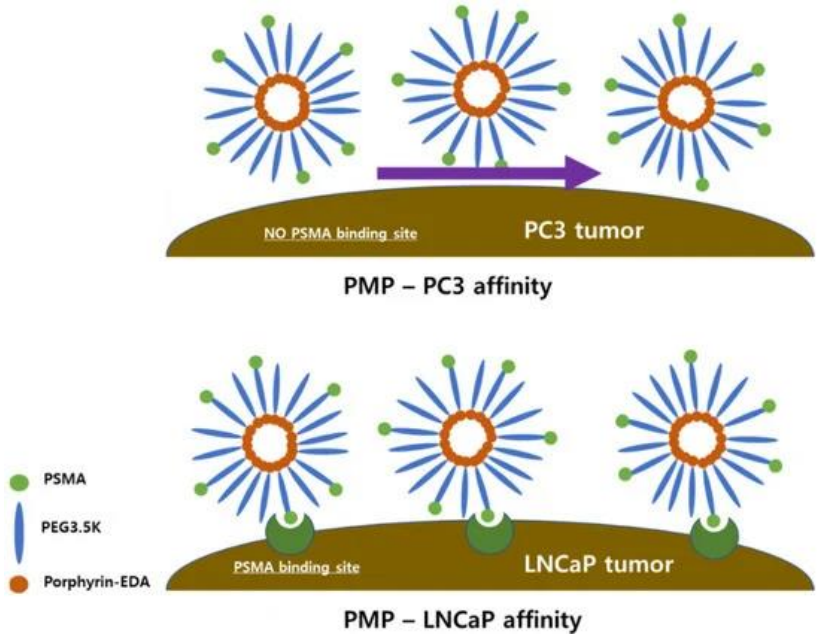

Figure 2.5.1. Schematic of PMP binding to the LNCaP tumor model.

2.5.2.2. Characterization of PM and PMP

Porphyrin–Micelle (PM) and Porphyrin–Micelle–PSMA (PMP) nanoparticles were characterized according to their size and zeta potentials (Table 2.5.1). For these measurements, dynamic light scattering was used (Malvern Zetasizer Nano, Malvern Instrument Ltd., Malvern, UK). There were no significant differences between the sizes and the total yields of the nanoparticle formulations, which had a mean diameter of 23 ± 4.5 and 26 ± 6.2 nm for PM and PMP, respectively. The sizes and the shapes of the nanoparticles were also evaluated with scanning electron microscopy (SEM) and transmission electron microscopy (TEM) (Figure 2.5.2B). We confirmed the spherical shape of the nanoparticles and that they were well-dispersed across the medium. Furthermore, there was no statistical difference between the zeta potential values for PM and PMP, which had voltages of −11.3 ± 2.1 and −14.4 ± 2.8 mV, respectively. As such, we speculated that the effects of the conjugated PSMA-targeting moiety on zeta potentials would be marginal. Furthermore, we examined the molecular weight of PM and PMP using MALDI–TOF, according to which data (Figure 2.5.2A), an increase in molecular weight was observed, suggesting the formation of Porphyrin Micelles. There was also an intensity between 3000 and 4000 m/z in the PEG3.5K graph, and it was speculated that most sizes of

PEG3.5K would be in this range. After PPR was conjugated to PEG3.5K, the m/z intensity in that range significantly decreased, because, we speculated, the PPR reacted better with the short PEG.

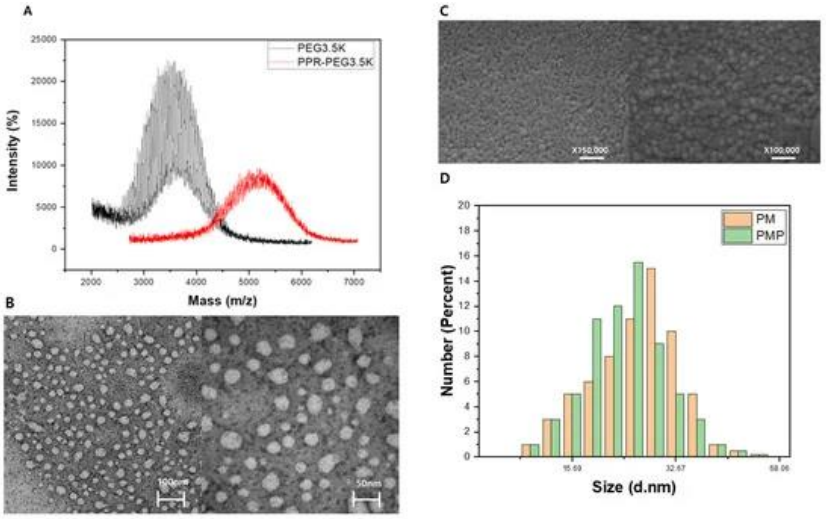

Figure 2.5.2. (A) MALDI–TOF data of PEG3.5K and porphyrin-PEG3.5K.

(B) TEM image of PM. (C) SEM image of PM. (D) DLS data of PM & PMP.

Table 2.4.2. Size and zeta potential of porphyrin micelle nanoparticles.

Porphyrin Micelle	Size (nm)	Zeta Potential (mV)
PM	23 ± 4.5	−11.3 ± 2.1
PMP	26 ± 6.2	−14.4 ± 2.8

2.5.2.3. In Vitro Cell Viability Study and Confocal Microscopy

The cytotoxic effects of Porphyrin, PM, and PMP were first evaluated in vitro using the PSMA-expressing LNCaP and PSMA-null PC-3 cancer cell lines and the materials not attached to the PSMA-targeting moiety were excluded because they did not adhere well to the surface of cells [40]. First, different concentrations of Porphyrin, PM, and PMP were incubated with the cells to observe the effects on the cell viability of the two cell lines. Compared to the untreated control, none of Porphyrin, PM, and PMP groups had a significant effect on the viability or morphology of the LNCaP (Figure 2.5.3A) and PC-3 (Figure 2.5.3B) cells. Next, the cells were incubated with PMP for 24 h and then observed under a confocal microscope. While a strong localization signal from PMP was observed on the surface of PSMA-expressing LNCaP cells, no fluorescence was observed in the PSMA-null PC-3 cells incubated with PMP, demonstrating the strong binding efficiency of the PSMA-targeting PMPs (Figure 2.5.3C).

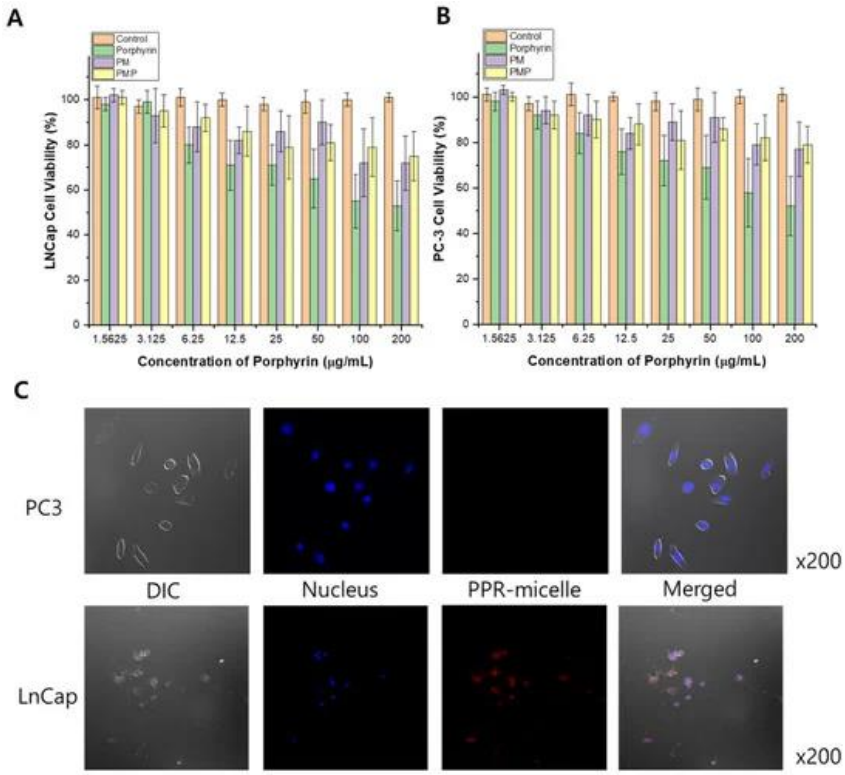

Figure 2.5.3. Cytotoxicity of porphyrin, PM, and PMP in vitro. (A) LNCaP cell line at difference material concentrations. (B) PC-3 cells at different material concentrations. (C) Confocal images of LNCaP and PC-3 cells treated with PMP to test binding affinity. Scale bar: 50 μm.

2.5.2.4. Selection of Optimal Laser Wavelength

For the selection of the optimal imaging laser wavelength, PA signals generated by porphyrin and PM were measured by changing the wavelength from 680 to 880 nm [40]. Note that changes in PA signal intensity were linearly proportional to the optical absorbance of a target. The ultrasound images in Figure 2.5.4A showed the upper and bottom portions of the silicone tube that contained PM nanoparticles, porphyrin, and water. Since the nanoparticle size was on the order of tens of nanometers and it was much smaller than the ultrasound wavelength (i.e., hundreds of micrometers), ultrasound backscattering was negligible and thus any information about the nanoparticles or porphyrin and water did not appear in the ultrasound images. In contrast, the PA images of PMP and porphyrin nanoparticles were clearly shown (Figure 2.5.4B) because the particles were able to absorb the laser energy and generate PA signals. Since the water did not contains any laser absorbers, low PA signals were observed. The average PA signal intensity was 2.89 times higher for PMP than for porphyrin (Figure 2.5.4C). This implies that the PMP particles were better laser absorbers than porphyrin. In addition, the PMP particles absorbed the laser to the maximum when the wavelength was 680 nm; the PA signal generated by the PMP particles was 5.06 times higher

than that of porphyrin at the same wavelength; thus, it was considered the optimal wavelength for PA imaging of the PMP particles.

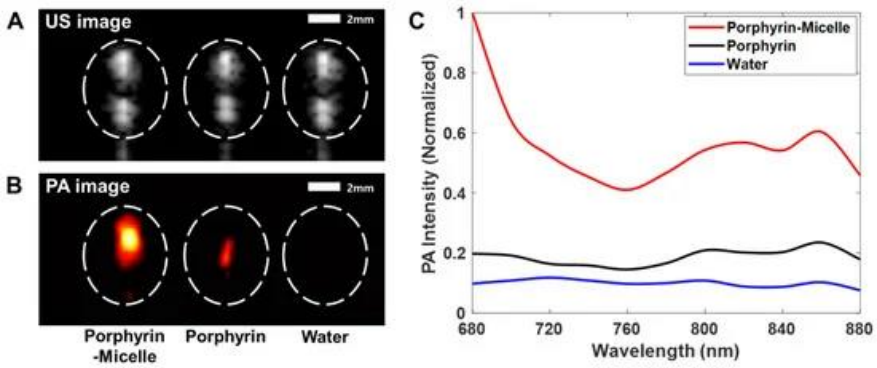

Figure 2.5.4. Ultrasound and photoacoustic images of silicone tubes containing Porphyrin–Micelle (left), Porphyrin (center), and water (right): (A) ultrasound images and (B) photoacoustic images. (C) Plot of changes in photoacoustic signal intensity as a function of laser wavelength.

2.5.2.5. Photoacoustic Imaging of the Tumor in Vivo

The in vivo imaging performance of each particle was evaluated with the mouse models bearing PC-3 and LNCaP tumors. After injecting porphyrin, PM and PMP, both ultrasound and PA images were acquired every 5 min for 30 min. For the PA imaging, the optimal laser wavelength of 680 nm was used. The combined ultrasound and PA images are shown in Figure 2.5.5 before the injection of PMP (left panel of Figure 5A), PM (the left panel of Figure 2.5.5B), or porphyrin (left panel of Figure 2.5.5C). The PA signals were observed only in the cutaneous region of the mice prior to the injection, but the generation of the PA signals was negligible within the tumor regions indicated by the dashed white circles in Figure 2.5.5. Five minutes after PMP injection, the PA signal strength increased significantly within the LNCaP tumor, but it did not change much within the PC-3 tumor (see Figure 2.5.5A,D,E). No significant changes in PA signal strengths were also observed within the LNCaP and PC-3 tumors after the PM and porphyrin injection. The average PA signal intensity was 13 times higher for PMP inside the LNCaP tumor than for PMP inside the PC-3 tumor or for PM and porphyrin inside both LNCaP and PC-3 tumors. The results implied that only PMP nanoparticles bind well PSMA, which is highly overexpressed by prostate (LNCaP) tumors.

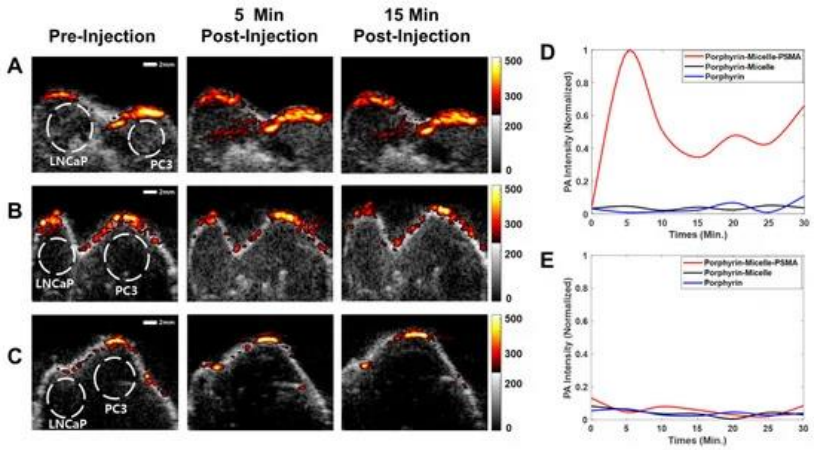

Figure 2.5.5. Combined ultrasound and photoacoustic images of the tumors in the mice before (left panels) and after intravenous injection of the particles (middle panels: after 5 min, right panels: after 15 min): (A) PMP, (B) PM, and (C) porphyrin. Plots of the changes in PA intensity inside (D) the LNCaP tumors and (E) the PC-3 tumors as a function of time.

2.5.3. Discussion

2.5.4. Materials and Methods

Porphyrin-based materials are continuously being investigated in biomedicine owing to their unique characteristics, such as absorbing light efficiently at a wide range, thereby inducing chemical and physical changes. Because of these properties, porphyrin derivatives have been used in clinics as photodynamic agents in bladder cancer treatment. As demonstrated in this work, a higher accumulation of photosensitizers at the tumor region allows selective, highly sensitive PA imaging of the targeted tumors. To improve the circulation half-life and the accumulation of these PA agents, we also prepared porphyrins in nanoparticle formulations. The porphyrin micelles, PM, and the PSMA-targeting PMs (PMPs) were prepared in a way that porphyrins were packed inside the globular structure with branches of polyethylene glycol facing outward to the surface.

This phenomenon is presumed probably because the aggregated porphyrin concentration is higher than that of the porphyrin that only spread in all directions in the solution. In fact, when compared to blood, a signal about 4 times higher than that of only porphyrin was confirmed because of checking at the same concentration, and a superior signal was confirmed compared to only porphyrin. Since the concentration of PMP

that can be injected is low compared to the high concentration of blood in living organisms, there was no noticeable difference in the in vivo experiment, but when PSMA attached to the PM, the signal difference between PM and PMP was secured in the LNCaP model. Through this, it was possible to confirm the possibility of PMP. In addition to its diagnostic use, PMP is expected to be used as an anticancer agent against the toxic side effects of anticancer drugs. According to the results of many studies on porphyrin, the possibility of cancer treatment was confirmed through ROS generated by the meeting of porphyrin and ultrasound, and it can be considered as an excellent particle not only for diagnosis through PMP but also used for cancer treatment using ultrasound in the future.

2.5.4.1. Reagents and Equipment

Hemin porphyrin was acquired from Sigma Aldrich (St. Louis, MO, USA). PEG3.5K was acquired from creative PEG Works (Chapel Hill, NC, USA) (Sodium borohydride (NaBH4), sodium cyanoborohydride (NaCNBH3), Zolazepam (Zoletil®) was obtained fromVirbac (Virbac, Carros, France), and xylazine hydrochloride (Rompun 2%)was acquired from Bayer (Bayer Korea, Seoul, Korea). The 1260 Infinity II LC system was acquired from Agilent Technologies (Agilent Technologies, Santa Clara, CA, USA).

2.5.4.2. Preparation of PMP

To synthesize PEG3.5K-TZ(PEG3.5K-methylenetetrazine), PEG3.5K-amine and methylene tetrazine-NHS were dissolved in DCM at 1:1 molar ratio over stirring for 30 min. After DCM was evaporated by distillation, Hemin Porphyrin and DMF were added in the same batch and stirred for 1 h. The solution was distilled, and the pellet was re-dispersed with distilled water. The solution was centrifugated at 15,000 rpm for 15 min at 4 °C to discard unreacted water-insoluble material. The final material was checked with MALDI–TOF to see if the PM had been synthesized. The size of PM was measured with DLS and freeze-dried. To prepare PMP, PSMA targeting moiety, PM and CDI were dissolved in distilled water at 0.3:1:0.3 molar ratio over stirring for overnight. 5k Amicon was used to purify the PMP and stored at 5 °C.

2.5.4.3. Characterization of PMP

The hydrodynamic size, polydispersity, and zeta potential of the prepared PMP and PM materials were measured by using the dynamic light scattering (DLS) (Zetasizer Nano ZS90; Malvern Instruments, Malvern, UK). The molecular weight of the synthesized PM was measured using MALDI–TOF and the morphology and size of the PMP and PM materials were further studied with transmission electron microscopy (TEM) and scanning electron microscopy (SEM) at the

National Center for Inter-University Facilities, Seoul National University, Korea.

2.5.4.4. Cell Culture

Human prostate cancer line LNCaP and PC-3 cells were acquired from the American Type Culture Collection (ATCC) and were cultured in Dulbecco's Modified Eagle Medium (DMEM) and Roswell Park Memorial Institute (RPMI), respectively, and supplemented with 10% heat-inactivated fetal bovine serum (FBS), 100 IU/mL penicillin, 100 mg/mL streptomycin, and 2 mM L-glutamine. Cultures were stored in a humidified atmosphere with 5% CO_2 at 37 °C and frequently tested for mycoplasma contamination. Cells were sub-cultured once they reached 80% confluence, determined by the trypan blue dye exclusion method.

2.5.4.5. Cell Viability Assay

The CellTiter 96® AQueous One Solution Cell Proliferation Assay (MTS) method was used to measure the effects of PM, PMP, and porphyrin on cell viability. LNcaP and PC-3 cells were seeded on 96-well plates at a density of 5×10^3 cells per well and incubated overnight. First, the effects of PM, PMP, porphyrin on cell viability were evaluated by adding various concentrations to both LNCaP and PC-3 cells. Cells were removed from the incubator at certain times, and their viability was evaluated against the phosphate-buffered saline (PBS) controls using the

MTS solution to derive approximate IC50 values.

2.5.4.6. Confocal Laser Scanning Microscopy

LNCaP and PC-3 cells were seeded on 8-well chamber slides (Nunc—Lab-Tek—II Chamber Slide—System, Thermo-Fisher Scientific, Waltham, MA, USA) at a density of 3×10^4 cells per well and incubated overnight. On the next day, the cells were treated with various concentrations of Porphyrin, PM, and PMP and further incubated for varying periods. Once incubation was complete, the cells were fixed for 15 min with 4% formaldehyde and counter-stained with 40,6-diamidino-2-phenylindole dyes (DAPI, Thermo-Fisher Scientific, Waltham, MA, USA). During fixation and staining, the cells were washed with fresh PBS. The images were acquired using a confocal microscope (Carl Zeiss, Inc., Oberkochen, Germany), using the excitation/emission wavelengths of 600 nm.

2.5.4.7. In Vivo Study

Immunodeficient, 6–8 week-old nude female mice were purchased from Orient Bio (Seoul, Korea) for the toxicity and efficacy studies. The mice were acclimated for a week before the start of the study and were maintained at standard conditions in specific pathogen-free (SPF) environments: 25 ± 2 °C temperature, 50 ± 10% relative humidity, and 12 h light/12 h dark. All mice were fed sterilized standard mouse chow

and water ad libitum. After acclimatization, 1×10^6 LNCaP and PC-3 cells suspended in Matrigel (Corning, Tewksbury, MA, USA) were injected into the right flank regions of the mice. Once the tumor volume had reached ~150 mm^3, the mice were randomly sorted for treatment. The tumor sizes were monitored with a digital caliper, and the volumes were calculated according to the formula $width^2 \times length \times 0.5$. All the in vivo protocols (Approval Number: BA-1911-283-083-01) were verified according to the guidelines of the Seoul National University Bundang Hospital.

2.5.4.8. Photoacoustic Protocols Ex-Vivo

For ultrasound imaging and PA signal reception, a commercial ultrasound research imaging scanner (Vantage 128, Verasonics, Inc., Redmond, WA, USA) equipped with an ultrasound linear array transducer (L7-4, Verasonics Inc., Kirkland, WA, USA) was used. For PA imaging, the linear array transducer was integrated with custom-made bifurcated optical fibers. Laser pulses with a length of 7 ns were generated by a Nd:YAG laser excitation system Surelite III-10 and Surelite OPO Plus, Continuum Inc., Santa Clara, CA, USA) and delivered into the target regions through optical fibers. The laser pulse repetition rate was 10 Hz and the energy density was measured at 4.23 mJ/cm^2 in front of the optical fibers. Detailed experimental arrangement

could be found in [41].

For optimal wavelength selection, three silicone tubes (AAQ04091, Tygon® MedicalTubing, Saint-Gobain Corp, Courbevoie, France) were prepared. The tube had an inner diameter of 1.27 mm (or 0.05 inches) and an outer diameter of 2.286 mm (or 0.09 inches). The tubes were immersed into a container filled with deionized water. Porphyrin, PM nanoparticles, and water were injected into the tubes. The concentrations of porphyrin and PM nanoparticles were each 0.8 mg/mL. Ultrasound imaging scanning was conducted to place the tubes at the focal depth of the array transducer; the final location of the tubes was 25 mm from the array surface. PA signals were acquired by changing the laser wavelength from 680 to 880 nm in 10 nm increments. The stored ultrasound and PA signals were used to construct images on MATLAB (MathWorks Inc., Natick, MA, USA). The strength of PA signals inside the ultrasound images of the tubes was measured, and the maximum signal intensity was calculated.

The in vivo experiment was performed with the same imaging equipment, but the laser wavelength was fixed at 680 nm, selected as the optimal wavelength. The ultrasound and PA images of both LNCaP and PC-3 cells injected regions were acquired as reference images. The PMP, PM, and porphyrin were injected into the tumor sites of three mice,

respectively. Both ultrasound and PA image data were acquired for 30 min at an interval of 5 min after the injection. The image data were used for construction of combined ultrasound and PA images with the MATLAB software. After delineating the LNCaP and PC-3 tumor regions on the ultrasound images, the strengths of PA signals inside the regions were measured, and the average PA strength was calculated.

2.5.5. Conclusion

In this work, we synthesized porphyrin conjugated to PEG3.5K and clarified the hydrophilic and hydrophobic parts that induce self-assembled porphyrin micelles. In addition, by attaching a targeting moiety (PSMA), which can only be attached to LNCaP, the delivery also improved. Through the photoacoustic device, it was possible to confirm the increase in the signal of the substance and its binding affinity, and through this another possibility for prostate cancer diagnosis was confirmed. Here, if porphyrin and ROS generated by ultrasound are used together, it will be an excellent theragnostic material that can be used to diagnose and treat at the same time without using anticancer drugs.

References

[1] Nelen, V. Epidemiology of prostate cancer. In Prostate Cancer; Springer: New York, NY, USA, 2007; pp. 1–8.

[2] Brawley, O.W. Trends in prostate cancer in the United States. J. Natl. Cancer Inst. 2012, 2012, 152–156.

[3] Chaudhry, P.; Asselin, E. Resistance to chemotherapy and hormone therapy in endometrial cancer. Endocr. Relat. Cancer 2009, 16, 363–380.

[4] Mannuel, H.D.; Hussain, A. Evolving role of surgery, radiation, hormone therapy, and chemotherapy in high-risk locally advanced prostate cancer. Clin. Genitourin. Cancer 2006, 5, 43–49.

[5] Dearnaley, D.P.; Khoo, V.S.; Norman, A.R.; Meyer, L.; Nahum, A.; Tait, D.; Yarnold, J.; Horwich, A. Comparison of radiation side-effects of conformal and conventional radiotherapy in prostate cancer: A randomised trial. Lancet 1999, 353, 267–272.

[6] Korfage, I.J.; Hak, T.; de Koning, H.J.; Essink-Bot, M.-L. Patients' perceptions of the side-effects of prostate cancer treatment—A qualitative interview study. Soc. Sci. Med. 2006, 63, 911–919.

[7] Bottomley, D.; Ash, D.; Al-Qaisieh, B.; Carey, B.; Joseph, J.; Clair, S.S.; Gould, K. Side effects of permanent I125 prostate seed implants in 667 patients treated in Leeds. Radiother. Oncol. 2007, 82, 46–49.

[8] Dadfar, S.M.; Roemhild, K.; Drude, N.; von Stillfried, S.; Knüchel, R.; Kiessling, F.; Lammers, T. Iron oxide nanoparticles: Diagnostic, therapeutic and theranostic applications. Adv. Drug Deliv. Rev. 2019, 138, 302–325.

[9] Van der Leest, M.; Cornel, E.; Israël, B.; Hendriks, R.; Padhani, A.R.;

Hoogenboom, M.; Zamecnik, P.; Bakker, D.; Yanti Setiasti, A.; Veltman, J.; et al. Head-to-head comparison of transrectal ultrasound-guided prostate biopsy versus multiparametric prostate resonance imaging with subsequent magnetic resonance-guided biopsy in biopsy-naive men with elevated prostate-specific antigen: A large prospective multicenter clinical study. Eur. Urol. 2019, 75, 570–578.

[10] Hoeks, C.M.; Schouten, M.G.; Bomers, J.G.; Hoogendoorn, S.P.; de Kaa, C.A.H.-V.; Hambrock, T.; Vergunst, H.; Sedelaar, J.M.; Fütterer, J.J.; Barentsz, J.O. Three-tesla magnetic resonance–guided prostate biopsy in men with increased prostate-specific antigen and repeated, negative, random, systematic, transrectal ultrasound biopsies: Detection of clinically significant prostate cancers. Eur. Urol. 2012, 62, 902–909.

[11] Fascelli, M.; Rais-Bahrami, S.; Sankineni, S.; Brown, A.M.; George, A.K.; Ho, R.; Frye, T.; Kilchevsky, A.; Chelluri, R.; Abboud, S.; et al. Combined biparametric prostate magnetic resonance imaging and prostate-specific antigen in the detection of prostate cancer: A validation study in a biopsy-naive patient population. Urol. 2016, 88, 125–134.

[12] Park, B.K.; Park, J.W.; Park, S.Y.; Kim, C.K.; Lee, H.M.; Jeon, S.S.; Seo, S.I.; Jeong, B.C.; Choi, H.Y. Prospective evaluation of 3-T MRI performed before initial transrectal ultrasound–guided prostate biopsy in patients with high prostate-specific antigen and no previous biopsy. Am. J. Roentgenol. 2011, 197, W876–W881.

[13] Rais-Bahrami, S.; Siddiqui, M.M.; Vourganti, S.; Turkbey, B.; Rastinehad, A.R.; Stamatakis, L.; Truong, H.; Walton-Diaz, A.; Hoang, A.N.; Nix, J.W.; et al. Diagnostic value of biparametric magnetic resonance imaging (MRI) as an adjunct to prostate-specific antigen (PSA)-based detection of prostate cancer in men without prior biopsies. BJU Int. 2014, 115, 381–388.

[14] Siddique, S.; Chow, J.C.L. Application of Nanomaterials in biomedical imaging and cancer therapy. Nanomaterials 2020, 10, 1700.

[15] Siddique, S.; Chow, J.C.L. Gold nanoparticles for drug delivery and cancer therapy. Appl. Sci. 2020, 10, 3824.

[16] Labrie, F.; Dupont, A.; Suburu, R.; Cusan, L.; Tremblay, M.; Gomez, J.-L.; Emond, J. Serum prostate specific antigen as pre-screening test for prostate cancer. J. Urol. 1992, 147, 846–851.

[17] Mohler, J.; Bahnson, R.R.; Boston, B.; Busby, J.E.; D'Amico, A.; Eastham, J.; Enke, C.A.; George, D.; Horwitz, E.M.; Huben, R.P.; et al. Prostate cancer. J. Natl. Compr. Cancer Netw. 2010, 8, 162–200.

[18] Govers, T.M.; Hessels, D.; Vlaeminck-Guillem, V.; Schmitz-Dräger, B.J.; Stief, C.G.; Martinez-Ballesteros, C.; Ferro, M.; Borque-Fernando, A.; Rubio-Briones, J.; Sedelaar, J.P.M.; et al. Cost-effectiveness of SelectMDx for prostate cancer in four European countries: A comparative modeling study. Prostate Cancer Prostatic Dis. 2018, 22, 101–109.

[19] Evans, N.; Jackson, A.; Matlin, S.; Towill, R. High-performance liquid chromatographic analysis of porphyrins in clinical materials. J. Chromatogr. A 1976, 125, 345–355.

[20] Mang, T.S.; Dougherty, T.J.; Potter, W.R.; Boyle, D.G.; Somer, S.; Moan, J. Photobleaching of porphyrins used in photodynamic therapy and implications for therapy. Photochem. Photobiol. 1987, 45, 501–506.

[21] Kessel, D. Methods in Porphyrin Photosensitization; Springer: New York, NY, USA, 1985.

[22] Akbarzadeh, I.; Yaraki, M.T.; Bourbour, M.; Noorbazargan, H.; Lajevardi, A.; Shilsar, S.M.S.; Heidari, F.; Mousavian, S.M. Optimized

doxycycline-loaded niosomal formulation for treatment of infection-associated prostate cancer: An in-vitro investigation. J. Drug Deliv. Sci. Technol. 2020, 57, 101715.

[23] Yaraki, M.T.; Pan, Y.; Hu, F.; Yu, Y.; Liu, B.; Tan, Y.N. Nanosilver-enhanced AIE photosensitizer for simultaneous bioimaging and photodynamic therapy. Mater. Chem. Front. 2020, 4, 3074–3085

[24] Bressler, N.M.; Bressler, S.B. Photodynamic therapy with verteporfin (Visudyne): Impact on ophthalmology and visual sciences. Investig. Ophthalmol. Vis. Sci. 2000, 41, 624–628.

[25] Bressler, N.M. Photodynamic therapy of subfoveal choroidal neovascularization in age-related macular degeneration with verteporfin: Two-year results of 2 randomized clinical trials-tap report. Arch. Ophthalmol. 2001, 119, 198–207.

[26] Khurana, M.; Collins, H.A.; Karotki, A.; Anderson, H.L.; Cramb, D.T.; Wilson, B.C. Quantitative in vitro demonstration of two-photon photodynamic therapy using Photofrin® and Visudyne®. Photochem. Photobiol. 2007, 83, 1441–1448.

[27] Zhou, Y.; Liang, X.; Dai, Z. Porphyrin-loaded nanoparticles for cancer theranostics. Nanoscale 2016, 8, 12394–12405.

[28] Zhang, L.; Lei, J.; Ma, F.; Ling, P.; Liu, J.; Ju, H. A porphyrin photosensitized metal–organic framework for cancer cell apoptosis and caspase responsive theranostics. Chem. Commun. 2015, 51, 10831–10834.

[29] Sternberg, E.D.; Dolphin, D.; Brückner, C. Porphyrin-based photosensitizers for use in photodynamic therapy. Tetrahedron 1998, 54, 4151–4202.

[30] Bonnett, R. Photosensitizers of the porphyrin and phthalocyanine series for photodynamic therapy. Chem. Soc. Rev. 1995, 24, 19–33.

[31] O'Connor, A.E.; Gallagher, W.; Byrne, A.T. Porphyrin and nonporphyrin photosensitizers in oncology: Preclinical and clinical advances in photodynamic therapy. Photochem. Photobiol. 2009, 85, 1053–1074.

[32] Maurer, T.; Eiber, M.; Schwaiger, M.E.M.; Gschwend, T.M.J.E. Current use of PSMA–PET in prostate cancer management. Nat. Rev. Urol. 2016, 13, 226–235.

[33] Ghosh, A.; Heston, W.D. Tumor target prostate specific membrane antigen (PSMA) and its regulation in prostate cancer. J. Cell. Biochem. 2004, 91, 528–539.

[34] Afshar-Oromieh, A.; Babich, J.W.; Kratochwil, C.; Giesel, F.L.; Eisenhut, M.; Kopka, K.; Haberkorn, U. The rise of PSMA ligands for diagnosis and therapy of prostate cancer. J. Nucl. Med. 2016, 57, 79S–89S.

[35] Ulrich, H.; Wrenger, C. Disease-specific biomarker discovery by aptamers. Cytom. Part A 2009, 75, 727–733.

[36] Dowling, P.; Clynes, M. Conditioned media from cell lines: A complementary model to clinical specimens for the discovery of disease-specific biomarkers. Proteomics 2011, 11, 794–804.

[37] Lolli, F.; Mulinacci, B.; Carotenuto, A.; Bonetti, B.; Sabatino, G.; Mazzanti, B.; D'Ursi, A.M.; Novellino, E.; Pazzagli, M.; Lovato, L.; et al. An N-glucosylated peptide detecting disease-specific autoantibodies, biomarkers of multiple sclerosis. Proc. Natl. Acad. Sci. USA 2005, 102, 10273–10278.

[38] Schmuck, S.; von Klot, C.A.; Henkenberens, C.; Sohns, J.M.; Christiansen, H.; Wester, H.-J.; Ross, T.L.; Bengel, F.M.; Derlin, T. Initial experience with volumetric 68Ga-PSMA I&T PET/CT for Assessment of whole-body tumor burden as a quantitative imaging biomarker in patients with prostate cancer. J. Nucl. Med. 2017, 58, 1962–1968.

[39] Bravaccini, S.; Puccetti, M.; Bocchini, M.; Ravaioli, S.; Celli, M.; Scarpi, E.; De Giorgi, U.; Tumedei, M.M.; Raulli, G.; Cardinale, L.; et al. PSMA expression: A potential ally for the pathologist in prostate cancer diagnosis. Sci. Rep. 2018, 8, 1–8.

[40] Kang, J.; Kim, E.-K.; Kwak, J.Y.; Yoo, Y.; Song, T.-K.; Chang, J.H. Optimal laser wavelength for photoacoustic imaging of breast microcalcifications. Appl. Phys. Lett. 2011, 99, 153702.

[41] Evazalipour, Mehdi, et al. "Generation and characterization of nanobodies targeting PSMA for molecular imaging of prostate cancer." Contrast Media & Molecular Imaging 9.3 (2014): 211-220.

[42] Kim, H.; Jo, G.; Chang, J.H. Ultrasound-assisted photothermal therapy and real-time treatment monitoring. Biomed. Opt. Express 2018, 9, 4472–4480.

Chapter 3
Inorganic Nanoparticles

Parts of this chapter apear in:
D Kim, H Kyung, S.S Lee, SY Park, WC Yoo, HJ Lee, Published in ***Bulletin of the Korean Chemical Society,*** 2020, 41(2), 112-116

3.1. Evaluation of In Vitro Cell Cytotoxicity and MRI imaging of an Iron Oxide Nanoparticle-Loaded Ultrasound Sensitive Liposome(IOL)

3.1.1. Introduction

Magnetic resonance imaging (MRI) is a technology that utilizes magnetic forces to emit high-frequency waves to the human body, measures and analyzes the signals collected, and images them through a computer [1,2]. MRI equipment is one of the most useful diagnostic equipment available because it is less invasive to the human body than other radiation-based imaging modalities and also relatively clear images of the body can be obtained [3,4]. It is known that the resolution is superior to that of CT because it is possible to select images from various angles as well as one cross-section. MRI can diagnose not only muscle, cartilage, blood vessel, and nerve cross-sections, but also diseases such as brain tumors, brain hemorrhages, spinal cord tumors, and cancer [5,6,7,8].

Cancer is known as the most dangerous disease among the existing diseases. Although many studies on treatment are being actively conducted, various contrast agents and cancer diagnosis technologies are being investigated as treatment through early detection can dramatically

improve the outcome of the patient [9,10].

To maximize the efficiency of imaging equipment, the quality of the contrast medium is important. Iron oxide nanoparticles, which are ideal for MRI contrast agents, have been under active investigation [11]. Iron oxide nanoparticles is biocompatible and are magnetic. Furthermore, they can be modified to carry various functional groups that may be used in further conjugations with various materials and molecules [12]. However, iron oxide nanoparticles, like other external nanoparticles, have an issue of excretion from the human body. Iron oxide nanoparticles with a size of 100 nm or larger are usually cleared from the circulation by the reticuloendothelial system. As such, the need for the existence of various carriers is still shown to minimize the clearance of the iron oxide nanoparticles because the clearance does not occur even with a small size.

Various drug carriers are required to contain the iron oxide nanoparticles in the carrier. There are several types of drug carriers. Among them, liposomes have been widely studied for biomedical applications and are currently leading the nanomedicine market [13]. Liposomes can improve bioavailability and increase cellular uptake of substances carried therein [14]. The substances supported on the liposome are physiologically protected, and the components of the liposome can support various substances due to the aqueous core and the

hydrophobic lipid bilayer [15]. Despite the functions of tumor delivery, long circulation, and substance protection of existing liposomes, problems due to limitations in substance release have been discussed. This problem can be solved by increasing the release effect of substances supported in liposomes through physical stimulation of ultrasound, and many studies are being conducted to find various release mechanisms up to now [15].

In addition to imaging, ultrasound can generate high pressure and temperature through cavitation [16]. This can lead to the destruction of the particles carrying the material, which could subsequently trigger the release of the payload. In addition, the harsh environment generated by ultrasound could cause enhanced accumulation of iron oxide nanoparticles, which may lead to improved MRI imaging of the region of interest upon ultrasound irradiation [17].

Utilizing this mechanism, liposomes that carry iron oxide particles as payloads can be designed in a way so that only upon the ultrasonic irradiation the nanoparticles are released into the surroundings (i.e., the desired region). This way, not only the contrast agent is protected from the reticuloendothelial clearance and potential side effects, but improved imaging performance can also be expected. In this study, MRI performance of the liposomes loaded with iron oxide nanoparticles under

the presence of ultrasound was evaluated. In addition, the toxicity of the substance was also looked upon.

3.1.2. Materials and Methods

3.1.2.1. Materials

1,2-distearoyl-sn-glycero-3-phosphocholine (DSPC), N-(Methylpolyoxyethylene oxycarbonyl)-1,2-distearoyl-sn-glycero-3-phosphoethanolamine (DSPE-mPEG2000), 1,2-Dioleoyl-sn-glycero-3-phosphoethanolamine (DOPE), 1-Stearoyl-2-lyso-sn-glycero-3-phosphocholine (S-LysoPC) and hydrogenated soybean phosphatidylcholine (HSPC) were purchased from NOF Co., Ltd. (Tokyo, Japan). Sphingomyelin was purchased from Avanti Polar Lipid (AL, USA). Cholesterol and ammonium sulfate were purchased from Merck (CA, USA). Ferric nitrate nonahydrate, poly (ethylene glycol) 600 (PEG), ethanol (EtOH, 99.9%), and ether were purchased from Samchun Chemical (Seoul, Korea). Double-distilled sterilized water was obtained using a water-purification system.

3.1.2.2. Preparation of Iron Oxide Nanoparticles

We prepared iron oxide nanoparticles using ferric nitrate as a precursor in a PEG medium. 0.404 g (1 mmol) of ferric nitrate nonahydrate was mixed with 12 g (20 mmol) of PEG to obtain a transparent red solution. The resulting mixture was heated to 90 °C at a

constant heating rate of 10 ℃·min-1 and maintained at that temperature for 30 minutes. During maintenance, the synthesis was performed under low pressure (76 cm Hg) to remove the generated H_2O vapor present in PEG and precursor using a shrink line. Then, nitrogen was purged into the reactor until the reaction was complete. Then, the mixture was heated to 265 ℃ at a constant heating rate of 3 ℃·min^{-1} and held at that temperature for 20 minutes. In this process, the initial transparent red solution gradually turned brown when the temperature was 140 ℃ or higher. At the end of the reaction, a brown-black solution is obtained, indicating the formation of iron oxide nanoparticles. The heat source was then removed, and the resulting solution was cooled to room temperature. A 1:3 ethanol-ether mixture was added to the solution and the nanoparticles were separated by centrifugation.

3.1.2.3. Preparation of SLs and IOLs

The lipid composition of liposome, which was obtained from a pilot study, was DSPC/DSPE-PEG/cholesterol/DOPE. liposome was fabricated by ethanol injection followed by extrusion. Briefly, 1.47 mg of DSPC, 2.62 mg g of DSPE-PEG, 2.17 mg of cholesterol, 9.73 mg of DOPE and 200 μg of iron oxide nanoparticles were dissolved in 1 mL of ethanol. The organic phase was gently heated to 60 °C to dissolve the lipid components. Then, the lipid-containing ethanol was injected into 4

mL of 250 mM ammonium sulfate solution at 250 rpm. Multilamellar vesicles (MLVs) were assembled and dispersed during ethanol injection and downsized by serial extrusion cycles with polycarbonate filter pore sizes ranging from 200 to 80 nm, using a LIPEX® 800 mL Thermobarrel extruder (Evonik, Canada). The temperature of the vesicles was maintained at 50 °C during the extrusion. The dispersion of extruded liposomes was exchanged with pH 6.5, 10% sucrose, and 10 mM histidine buffer using a 12–14-kDa dialysis membrane. The ammonium gradient across the liposomal membrane was generated by exchanging ammonium sulfate to the buffer and stored at 2-8 °C.

3.1.2.4. Characterization of Iron Oxide Nanoparticles, Sonosensitive-Liposome (SL), and IOLs

The hydrodynamic size, polydispersity, and zeta potential of the prepared nanoparticles were measured using the dynamic light scattering (DLS) method (Zetasizer Nano ZS90; Malvern Instruments, Malvern, UK). The morphology and size of the Iron Oxide NPs, SL, and IOLs were further studied with transmission electron microscopy (TEM) at the National Center for Inter-University Facilities, Seoul National University (South Korea).

3.1.3. Results and Discussions

3.1.3.1. Characterization of Iron Oxide Nanoparticles,

Sonosensitive-Liposome (SL), and IOLs

Iron oxide NPs, SL, and IOLs were prepared, and their size and PDI values were measured. The size values came out as 21±3 nm, 138±23.2 nm, and 154±29.7 nm, respectively (Table 3.1.1), and to confirm the size and shape, it was confirmed by taking a TEM picture. Also the Zeta potential of Iron oxide NPs, SL, and IOLs were measured and the value were -17±2.1, -12±1.9, and -15±2.1 mV respectively.

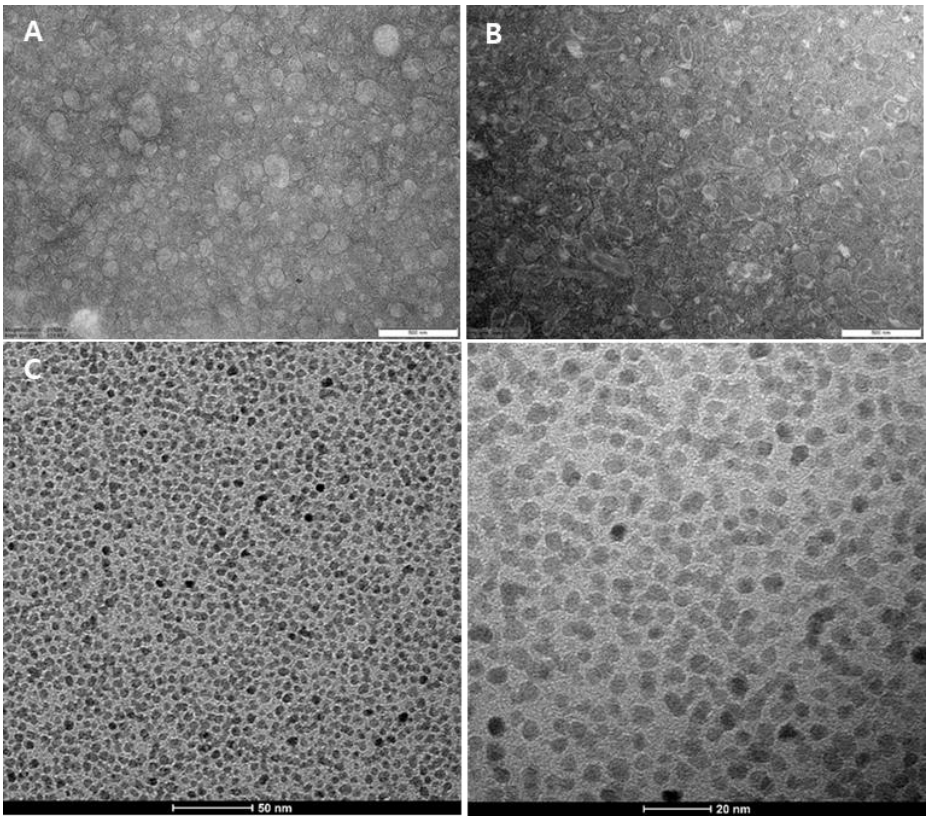

Figure 3.1.1. (A) TEM image of SL. (B) TEM image of IOL. (C) TEM image of Ion oxide nanoparticle.

Table 3.1.1. The average size and the zeta potential values of sonosensitive-liposome (SL) and Iron oxide loaded sonosensitive-liposome (IOL)

Materials	Mean Size (Mean ± SD, nm)	Zeta Potential (mV)
SL	138 ± 23.2	-12.2 ± 1.9
IOL	154 ± 29.7	-15.1 ± 2.1

3.1.3.2. In vitro cell toxicity

The cytotoxicity was confirmed by MTT analysis using the U87MG cell line (Figure 3.1.2). We compared iron oxide NPs and IOL. Both groups were treated with cells at a concentration ranging from 0 to 100 μg/ml. Two time periods were conducted which were 48h and 72h. Iron oxide and IOLs did not affect on the cell in both time period and no difference between iron oxide NPs and IOLs groups. The data showed that there was no cytotoxic effect on the cell.

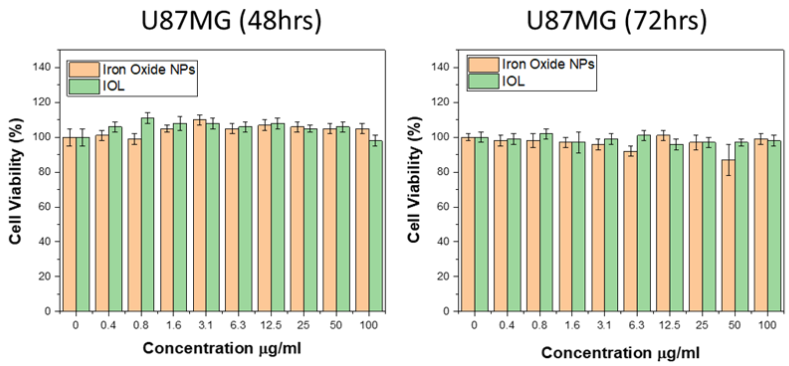

Figure 3.1.2. Cytotoxicity of Iron oxide nanoparticles and Iron oxide loaded sonosensitive-liposome (IOL) in vitro at 48 and 72 hrs time points.

3.1.3.3. In vitro MRI Imaging

Total of three groups were prepared: i) sonosensitive-liposome (SL), ii) Iron oxide nanoparticles loaded sonosensitive-liposomes (IOL) without ultrasound irradiation, iii) Iron oxide nanoparticles loaded sonosensitive-liposome (IOL) with ultrasound irradiation (Figure 3.1.3). The MRI imaging was tested by Ji Seok-Yeong Biomedical Research Institute. The data was shown that ultrasound irradiation (1MHz, 100W, 10%, 1 min per spot) group has stronger imaging compared to the group without ultrasound irradiation which indicates that the iron oxide nanoparticles agglomerated due to the high temperature and pressure generated by ultrasound.

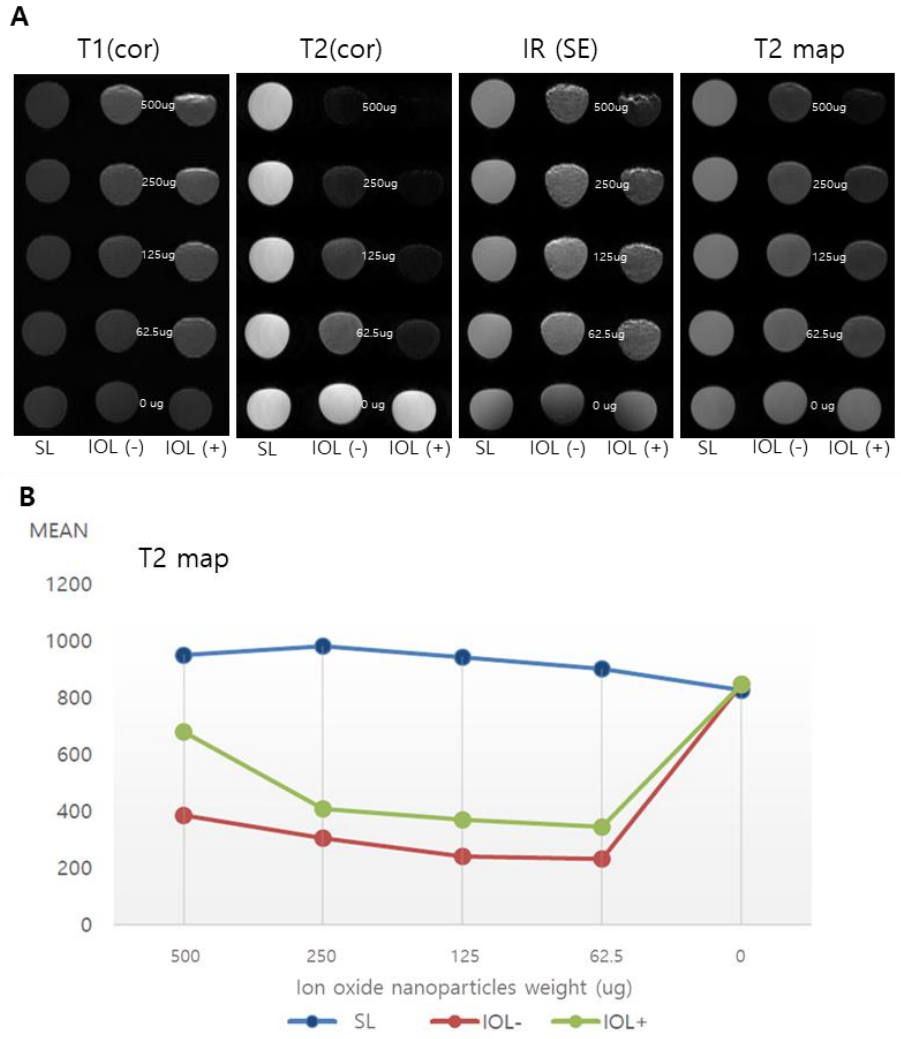

Figure 3.1.3. MRI image of SL, IOL (-), and IOL(+). (A) MRI image of T1, T2, IR, and T2 map with difference groups and different concentration of ion oxide nanoparticles. (B) Plot of changes in MRI signal intensity of SL, IOL(-), and IOL(+).

3.1.4. Conclusion

Through this experiment, we speculated that the ultrasound can be used to destruct the liposome and agglomate the iron oxide nanoparticles by generating high temperature and the pressure. There was a difference in the MRI imaging performance between the group irradiated with ultrasound and the group not irradiated with ultrasound, and through this, we found that we could reduce excretion by loading iron oxide nanoparticles into liposomes and also improve MRI imaging performance of a desired area through ultrasound irradiation.

References

[1] Pusey, Elizabeth, et al. "Magnetic resonance imaging artifacts: mechanism and clinical significance." Radiographics 6.5 (1986): 891-911.

[2] Dill, T. "Contraindications to magnetic resonance imaging." Heart 94.7 (2008): 943-948.

[3] Pipitone, Nicolò. "Value of MRI in diagnostics and evaluation of myositis." Current Opinion in Rheumatology 28.6 (2016): 625-630.

[4] Formica, Domenico, and Sergio Silvestri. "Biological effects of exposure to magnetic resonance imaging: an overview." Biomedical engineering online 3.1 (2004): 1-12.

[5] Carmi, Eyal, et al. "Resolution enhancement in MRI." Magnetic resonance imaging 24.2 (2006): 133-154.

[6] Puderbach, Michael, et al. "Proton MRI appearance of cystic fibrosis: comparison to CT." European radiology 17.3 (2007): 716-724.

[7] Makris, Nikos, et al. "MRI-based anatomical model of the human head for specific absorption rate mapping." Medical & biological engineering & computing 46.12 (2008): 1239-1251.

[8] Gillies, Robert J., et al. "MRI of the tumor microenvironment." Journal of Magnetic Resonance Imaging: An Official Journal of the International Society for Magnetic Resonance in Medicine 16.4 (2002): 430-450.

[9] Ott, J. J., A. Ullrich, and A. B. Miller. "The importance of early symptom recognition in the context of early detection and cancer survival." European Journal of Cancer 45.16 (2009): 2743-2748.

[10] Schiffman, Joshua D., Paul G. Fisher, and Peter Gibbs. "Early detection of cancer: past, present, and future." American Society of Clinical Oncology Educational Book 35.1 (2015): 57-65.

[11] Babes, Lucia, et al. "Synthesis of iron oxide nanoparticles used as MRI contrast agents: a parametric study." Journal of colloid and interface science 212.2 (1999): 474-482.

[12] Xie, Wensheng, et al. "Shape-, size-and structure-controlled synthesis and biocompatibility of iron oxide nanoparticles for magnetic theranostics." Theranostics 8.12 (2018): 3284.

[13] Wang, Shu, et al. "Application of nanotechnology in improving bioavailability and bioactivity of diet-derived phytochemicals." The Journal of nutritional biochemistry 25.4 (2014): 363-376.

[14] Rahman, Aquilur, et al. "Liposomal protection of adriamycin-induced cardiotoxicity in mice." Cancer research 40.5 (1980): 1532-1537.

[15] Winterhalter, Mathias, and Danilo D. Lasic. "Liposome stability and formation: experimental parameters and theories on the size distribution." Chemistry and physics of lipids 64.1-3 (1993): 35-43.

[16] Izadifar, Zahra, Paul Babyn, and Dean Chapman. "Ultrasound cavitation/microbubble detection and medical applications." Journal of Medical and Biological Engineering 39.3 (2019): 259-276.

[17] Unterweger, Harald, et al. "Dextran-coated superparamagnetic iron oxide nanoparticles for magnetic resonance imaging: Evaluation of size-dependent imaging properties, storage stability and safety." International journal of nanomedicine 13 (2018): 1899.

3.2. In vitro Evaluation of Carbon-Based Nanospheres as Drug Delivery Vesicels in Breast Cancer Cell

3.2.1. Introduction

Cancer still remains one of the leading causes of deaths across the globe, with its rate of incidence on the rise despite many efforts for developing prophylactics and treatment [1]. In addition to surgery, promising treatment options such as radiotherapy, gene therapy, photodynamic therapy, and biomarker-based treatments are currently under development across many labs, accounting for different types of cancers [2]. Often, classical chemotherapy relies on the systemic circulation and accumulation of cytotoxic chemical agents at the target of interest [3]. Since tumor microenvironment is characterized by uncontrolled neovascularization and a lack of organization, researchers have initially taken advantage of such phenomena and developed their drug delivery strategy based on such enhanced permeability and retention (EPR) effect [2,4]. Nonetheless, it has been demonstrated that despite the EPR effect, only a marginal amount of active pharmaceutical ingredient (API) actually reaches the tumor region, leading to low efficacy and unfavorable safety profiles. Therefore, one of the biggest

challenges in the development of APIs in the recent decades have been to develop nanoparticle-based drug delivery systems (DDS) that can enhance drugs' efficacy and safety profiles [5]. A desirable nanoparticle-based DDS needs to be biocompatible and yield high drug-loading capacity. For example, liposomes are one of the most widely used drug vesicles in DDS but they often have challenges in drug loading efficiency due to the limitation in the amount of agents that could actually be loaded [6]. Therefore, a successful DDS needs to find a balance between bio-compatibility and high drug-loading capacity, which would allow minimizing the dosage used while maximizing the therapeutic effect. In this regard, carbon-based materials such as graphene oxides, carbon nanotubes, carbon nanohorns, and carbon nanospheres have recently been investigated as drug delivery vehicles (DDVs) owing to their excellent bio-compatibility, EPR effect, and tailored surface modification [7,8,9]. Among those, carbon nanospheres (CSs) have gained great interest due to their tunable size and pore size and ultrahigh specific surface area (SSA) with aforementioned features. For example, Zhao et al. reported that mesoporous carbon spheres presented relatively stable cell-permeability toward KB (human nasopharyngeal epiclermal carcinoma) cells and high drug loading capacity (ibuprofen, 30 mg/g) [10]. They also reported a hydrophobic/hydrophilic multidrug delivery

approach using rattle-like dual-pore mesoporous carbon/silica nanospheres, resulted in superior cell killing efficacy compared to single-drug treatment [11]. In addition, hollow carbon spheres can also have high drug-loading capacity, low cell toxicity, and optimal drug release profile at low pH, which resulted in significant inhibition of tumor growth in esophageal xenograft cancer models [12]. In this study, monodisperse and size-tunable (170– 583 nm) CSs with ultrahigh SSA were successfully prepared and characterized as possible DDVs based on their biocompatibility, dispersion ability, stability, drug loading capacity, and cell viability. It was investigated that smaller CS with size of 170 nm (CS_S) showed great dispersibility and cell viability compared to the larger CSs (e.g., 397 and 583 nm) that presented cytotoxicity in the in vitro study, confirming the critical particle size of CS for DDS. In addition, activated CS_S (145 nm, denoted as CS_Sa) with ultrahigh SSA of 2619 m^2/g displayed high drug loading capacities for four different chemotherapeutic agents (gemcitabine, doxorubicin, docetaxel, and paclitaxel), representing its versatility as DDV. Furthermore, three different drug-loaded CS-Sa showed significant growth inhibition/IC50 values which shows the percentage of cell growth inhibition against MDA-MB-231 human breast cancer cell lines for up to 48 h.

3.2.2. Experimental Section

3.2.2.1. Materials

Resorcinol and formaldehyde were obtained from JUNSEI (Kyoto, Japan). Ammonia solution (25%) was obtained from FUJIFILM WAKO PURE CHEMICAL (Osaka, Japan).

3.2.2.2. Preparation of Carbon-Based Nanoparticles

Monodisperse and size-tunable PSs were synthesized by the modified Stober method using resorcinol (6.18, 13, and 18 mmol for PS_S, M, L, respectively) and formaldehyde (26, 54, and 76 mmol for PS_S, M, L, respectively) as precursors and ammonia (0.7 mL) as a base catalyst under aqueous solution (200 mL). The corresponding amounts of precursors for different sizes of PS were dissolved in the aqueous solution containing ammonia catalyst, and the solutions then were stirred for 24 h at room temperature and heated for 24 h at 90°C. The solutions were then centrifuged and washed with deionized water and ethanol for several times and dried in an 80°C oven. For carbonization, the synthesized PSs were heated with a ramp rate of 4.3 °C/min under a nitrogen atmosphere and maintained at 800°C for 3 h.

3.2.2.3. Preparation of Activated Carbons

The CS_S was heated with a ramp rate of 29°C/min under a nitrogen atmosphere and the gas changed to carbon dioxide (1000 cm^3/min) for

240 min (CS_Sa). After the activation process is completed, the gas was changed to nitrogen gas and the chamber was cooled down.

3.2.2.4. Dispersion of Carbon-Based Nanoparticles

Different types of carbon nanoparticles were dispersed in complete cell culture medium (RPMI-1640, a growth medium used in cell culture, Roswell Park Memorial Institute, from where it derives its name) to evaluate dispersibility in various solutions.

3.2.2.5. Particle Size and Zeta-Potential Measurement

The average size of prepared particles was measured by DLS using a Malvern Zetasizer (Malvern Instruments Ltd., Malvern, UK). The samples were diluted 1:400 with purified water and were measured at of 25°C at a scattering angle of 90°. The zeta potential of these particles was also measured with the same instrument (Malvern Instruments Ltd., Malvern, UK). The prepared nanoparticles were diluted 1:200 with 50 mM phosphate buffer at pH 7.4 and the zeta potential was determined by Laser Doppler microelectrophoresis.

3.2.2.6. Drug Loading to CSs

A stock solution of the different chemotherapy drugs (gemcitabine, doxorubicin, docetaxel and paclitaxel) (5 mg/mL) was prepared, from which and volumes between 50 and 800 µL were added to 20 mg of the empty nanoparticles. These mixtures were topped up to 4.0 mL with

deionized water, then were stirred for 24 h at room temperature to achieve an adsorption equilibrium of drugs to on the nanoparticle surface. Once the equilibrium was reached, the nanoparticles were washed as previously described. The supernatants of the washing steps were collected and the concentration of free drugs were analyzed by high-performance liquid chromatography.

3.2.2.7. In vitro Study

Breast cancer cell line (MDA-MB 231) was cultured in RPMI-1640 cell culture medium supplemented with 10% heat inactivated fetal bovine serum, 100 IU/mL penicillin, 100 mg/mL streptomycin, and 2 mM l-glutamine. Cultures were maintained in a humidified atmosphere with 5% CO^2 at 37°C. The cultured cells were sub cultured twice each per week, seeding at a density of about 2×10^3 cells/mL. Cell viability was determined by the trypan blue dye exclusion method.

3.2.2.8. Cell Viability-Assay

Cellular viability was examined using the MTT assay method (a colorimetric assay for assessing cell metabolic activity using a dye MTT [3-(4,5-dimethylthiazol-2-yl)-2,5-diphenyltetrazolium bromide]). MDA-MB-231 cells were seeded to 96-well plates at a density of 2×10^3 cells per well and left overnight in the incubator. On the next day, these cells were treated with three different RFC-L nanoparticles and were

incubated for 48 h. Cells were then removed from the incubator and their viability was evaluated using the MTT solution according to the manufacturer's instruction.

3.2.2.9. Characterization

Scanning electron microscopy (SEM) images were obtained with a HITACHI S-4800 microscope with an accelerating voltage of 15.0 kV. Nitrogen adsorption/desorption isotherms were measured using BELSORP MINI II. Specific surface areas were calculated by using Brunauer–Emmett–Teller (BET) method. Pore size distributions were calculated by using Barrett–Joyner–Halenda (BJH) method.

3.2.3. Results and Discussions

In attempts to prepare CSs, monodisperse and size-tunable polymer spheres (PSs) were first synthesized by the modified Stöber method previously reported elsewhere.13-16 Briefly, phenolic-resin PSs were synthesized by using resorcinol and formaldehyde (RF) as precursors and ammonia as a base catalyst in the water-ethanol mixture. By controlling the amount of RF, monodisperse PSs with size of 200 ± 27, 600 ± 20, and 802 ± 44 nm were successfully prepared and identified by SEM measurement (Figure 3.2.1). As-prepared PSs were then subjected to carbonization under nitrogen atmosphere to prepare CSs. During the carbonization process, the size of PSs was gradually reduced by 15–34%

due to radial shrinkage,13, 17 resulting in CSs with size of 171 ± 21 nm (small, S), 397 ± 16 (medium, M), and 583 ± 18 (large, L), hereafter denoted as CS_S, M, and L, respectively (Figure 3.2.1(a)–(c)). It is noteworthy that the monodispersity of these nanoparticles was relatively well preserved.

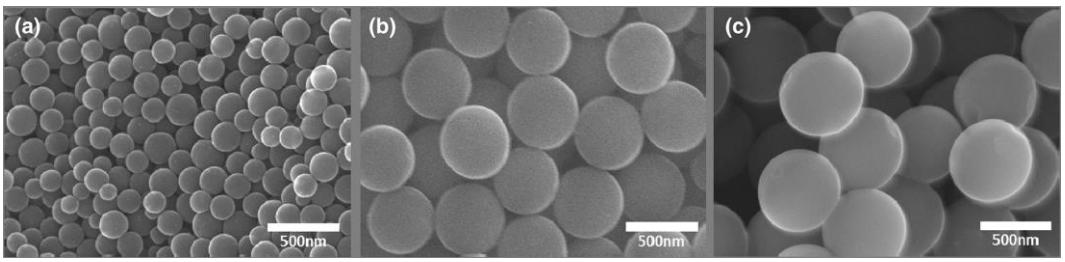

Figure 3.2.1. SEM images of CS_S (a, 171 ± 26 nm), CS_M (b, 397 ± 16 nm), CS_L (c, 583 ± 18 nm).

CSs were tested for their dispersibility in cell culture medium (RPMI). According to dynamic light scattering (DLS) analysis, the sizes of CSs were measured as 208 ± 90 (CS_S), 433 ± 63 (CS_M), and 987 ± 136 nm (CS_L), which were slightly larger than those measured under SEM investigation, clearly confirming the dispersion properties of CSs (Table S1). After 3 h dispersion, CSs were well-dispersed in the cell culture solution, strongly confirming their dispersibility (Figure S2). Such dispersion property of CSs could be attributed to the surface charge of CS in the cell culture solution, which were − 11.2 ± 0.3 (CS_S), −18.4 ± 0.8 (CS_M), and − 12.7 ± 0.6 (CS_L) determined by the Zetapotential measurement, respectively (Table S1).

For screening CSs as potential chemotherapeutic agent delivery, cellular cytotoxicity of CSs was examined against human breast cancer cell line (MDA-MB-231). CSs with different concentrations (0–100 μg/mL) were co-cultured with cancer cells for 3 days and cell viability post treatment were evaluated (Figure 3.2.2). CS_S presented negligible cellular cytotoxicity even at high concentration of 100 μg/mL, while cell viability profiles of CS_M and L showed obvious cellular toxicity at high concentrations (50–100 μg/mL) with CS_L presenting higher degree of cellular toxicity than CS_M (Figure 3.2.2). It seems that the particle size of CS significantly impacts on cell viability. It has widely

been accepted that nanoparticle-based DDVs with size less than 200 nm are appropriate for the delivery of chemotherapeutic agents.5 Since CS_S had negligible cell toxicity, it was chosen for further experiments, including maximize SSA for examining drug-loading and in vitro studies.

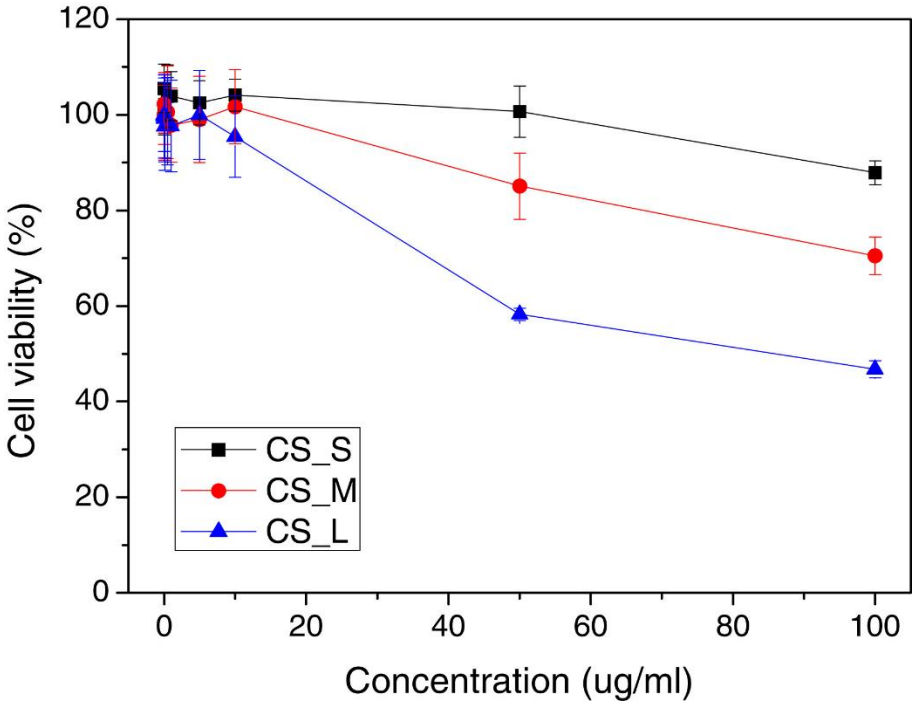

Figure 3.2.2. Cell viability of CS dependent on size. Cell viability of CS with size distribution at 208.7 ± 90.8 (CS_S; black), 433.9 ± 63.5 (CS_M; red), and 987.4 ± 136.1 (CS_L; blue), respectively.

Hot CO2 treatment was applied to CS_S to develop SAA (denoted as CS_Sa). The size of CS_Sa was reduced to 145 ± 19 nm from 171 ± 26 nm due to the loss of carbon ($CO2(g) + C(s) \rightarrow 2CO(s)$) during the activation process (Figure 3.2.3(a)).13, 17 In addition, nitrogen sorption isotherm of CS_Sa presented much increased uptake at very low relative pressure than that of CS_S, clearly confirming the development of microporosity (< 2 nm, Figure 3.2.3(b)). Presence of huge micropores with plainly visible small mesopores up to ca. 5 nm for CS_Sa compared to CS_S was also clearly confirmed by the BJH profiles (Figure 3.2.3(c)). According to the BET method, CS_Sa presented superior SSA of 2619 m^2/g than that (611 m^2/g) of CS_S, confirming that hot CO2 treatment effectively enhances SSA of the CS samples (Table 3.2.1). Furthermore, total pore volume (2.06 cm^3/g) measured at 0.99 P/P0 and micropore volume (1.08 cm^3/g) determined by the t-method of CS_Sa had increased significantly compared to those (0.47 and 0.24 cm^3/g) of CS_S during the activation process. Therefore, CS_S and Sa samples were tested for drug-loading and release, and in vitro experiments.

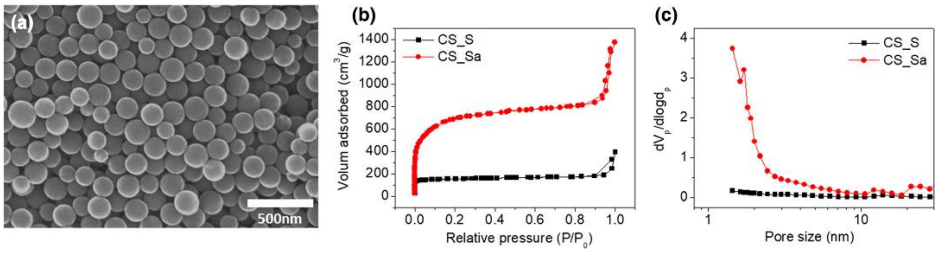

Figure 3.2.3. SEM images of CS_Sa (a, 145 ± 19 nm), (b) N2 sorption isotherm and (c) BJH pore size distributions of CS_S and CS_Sa.

Sample	BET surface area (m^2/g)	Total pore volume (cm^3/g)	Micropore volume (cm^3/g)	Drug loading (GEM, %)	Drug loading (DOX, %)	Drug loading (DTX, %)	Drug loading (PTX, %)
CS_S	611	0.47	0.24	30.5	50.4	0	0
CS_Sa	2619	2.06	1.08	98.4	100	92.1	96.4

Table 3.2.1. Textural and drug loading properties for CS_S and CS_Sa.

Next, we tried to load four types of chemotherapeutic agents—gemcitabine (GEM), doxorubicin (DOX), docetaxel (DTX), and paclitaxel (PTX), of which physical characteristics are listed in the Table S2—onto CS_S and Sa samples to evaluate their loading efficiency. When CS_S was employed for drug loading, moderate uptake efficiency for GEM (30.5%) and DOX (50.4%) were observed; in contrast, negligible uptakes for DTX and PTX were measured (Table 3.2.1). The molecular sizes of DTX and PTX are bigger than the others, thus small pore size distribution of CS_S could be responsible for the negligible uptakes of DTX and PTX. In addition, the other difference between listed drugs is their log p values, the unit for polarity of drug that related to the solubility. Different polarity of drug molecules could be a reason for different drug loading capacities of CS_S.

Meanwhile, CS_Sa was employed for drug loading tests. As expected, drug loading capacities of CS_Sa for GEM (98.4%) and DOX (100%) were significantly enhanced owing to the highly developed SSA (Table 3.2.1). Interestingly, drug uptakes for DTX (92.1%) and PTX (96.4%) were almost similar to the other drugs, strongly implying irrelevancy to the polarity of drug molecules. It seems reasonable that pore size distribution up to ca. 5 nm and ultrahigh SSA of 2619 m^2/g of CS_Sa could be attributed to such high drug loading capacities for DTX and

PTX (Figure 3.2.3(c) and Table 3.2.1). Since the CS_Sa had higher drug loading capacity compared to CS_S, we chose CS_Sa as the vehicle for drugs in in vitro studies.

DOX, DTX, and PTX loaded CS_Sa were examined for their potential anti-cancer effect (Figure 3.2.4). Drug-loaded CS-Sa showed significant growth inhibition/IC50 values which shows the percentage of cell growth inhibition against MDA-MB-231 human breast cancer cell lines for up to 48 h. DOX loaded CS_Sa group seemed to reach close to IC50 with the concentration of 25 μg/mL and slightly showed more anti-cancer effect on the cell, however, PTX and DTX loaded CS_Sa caught up when higher dose. Specially, the DTX loaded CS_Sa group showed the highest anti-cancer effect when concentration was increased up to 100 μg/mL. These results suggested that empty CS_Sa nanoparticles themselves do not have cytotoxicity and they released their drug cargo enough to inhibit cell growth in vitro despite the anti-cancer effect between drugs not being significantly different.

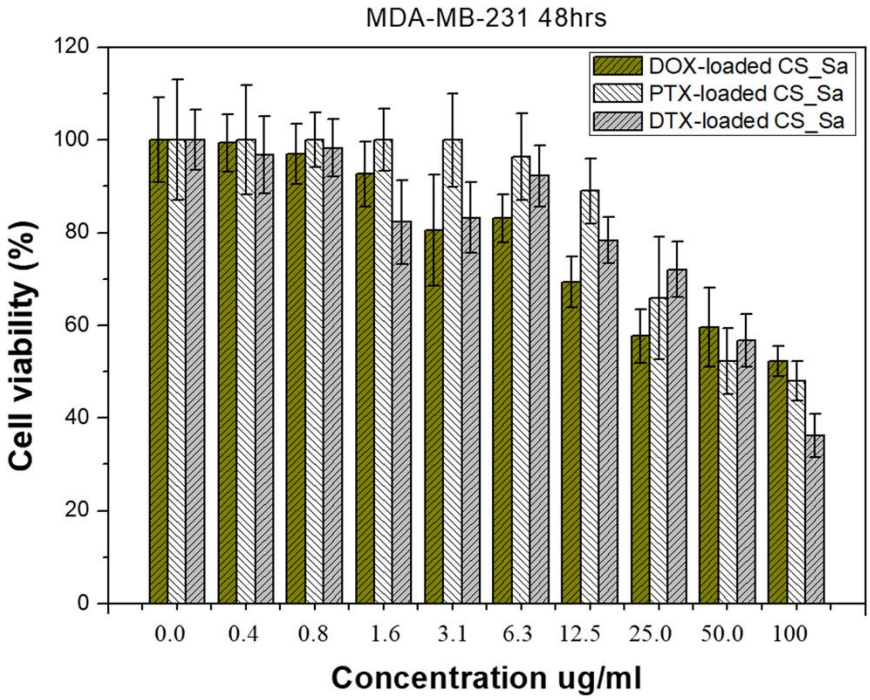

Figure 3.2.4 IC50 of CS_Sa loading doxorubicin (blue), paclitaxel (orange), and docetaxel (gray) to MDA-MB-231.

3.2.4. Conclusion

Monodisperse and size tunable CSs were successfully prepared, and additional activation process was further applied to enhance SSA up to 2619 m^2/g. Cellular cytotoxicity of different sizes of CSs were examined against human breast cancer cell line that larger CS_M and L presented cellular cytotoxicity against cancel cell; in contrast CS_S had negligible cell toxicity. When CS_S and Sa were tested for drug-loading of four different drugs, it was observed that CS_Sa with ultrahigh SSA and broad PSD up to ca. 5 nm showed excellent drug-loading capacity regardless of polarity and size of drugs. Furthermore, CS_Sa showed anti-cancer effects against MDA-MB-231 human breast cancer cell lines as well as favorable drug loading profiles. While we were not able to fully demonstrate the ability of CS_Sa to release 100% of their drug cargo upon specific stimulations yet, we believe that CSs may become promising in near future once appropriate drug release mechanism or cell uptake processes are elucidated.

Bibliography

[1] R. L. Siegel, K. D. Miller, A. Jemal, CA Cancer J. Clin. 2019, 69, 7.

[2] R. Misra, S. Acharya, S. K. Sahoo, Drug Discov. Today 2010, 15, 842..

[3] J. Della Rocca, D. Liu, W. Lin, Nanomedicine 2012, 7, 303..

[4] K. Greish, Cancer Nanotechnology, Springer, Switzerland AG, 2010, p. 25.

[5] T. M. Allen, P. R. Cullis, Science 2004, 303, 1818.

[6] Q. Xu, Y. Tanaka, J. T. Czernuszka, Biomaterials 2007, 28, 2687.

[7] T.-W. Kim, P.-W. Chung, I. I. Slowing, M. Tsunoda, E. S. Yeung, V. S.-Y. Lin, Nano Lett. 2008, 8, 3724.

[8] X. Huang, S. Wu, X. Du, Carbon 2016, 101, 135.

[9] T. Muthukumar, S. Prabhavathi, M. Chamundeeswari, T. P. Sastry, Mater. Sci. Eng. C 2014, 36, 14.

[10] Y. Fang, D. Gu, Y. Zou, Z. Wu, F. Li, R. Che, Y. Deng, B. Tu, D. Zhao, Angew. Chem. Int. Ed. 2010, 49, 7987.

[11] Y. Fang, G. Zheng, J. Yang, H. Tang, Y. Zhang, B. Kong, Y. Lv, C. Xu, A. M. Asiri, J. Zi, Angew. Chem. Int. Ed. 2014, 53, 5366.

[12] L. Zhang, M. Yao, W. Yan, X. Liu, B. Jiang, Z. Qian, Y. Gao, X.-j. Lu, X. Chen, Q.-l. Wang, Int. J. Nanomedicine 2017, 12, 6759.

[13] H. S. Kim, M. S. Kang, W. C. Yoo, J. Phys. Chem. C 2015, 119, 28512.

[14] J. Liu, S. Z. Qiao, H. Liu, J. Chen, A. Orpe, D. Zhao, G. Q. Lu, Angew. Chem. Int. Ed. 2011, 50, 5947.

[15] H. S. Kim, S. Lee, D. K. Kim, Y.-W. Lee, W. C. Yoo, RSC Adv. 2017, 7, 47251.

[16] M. Kim, H. S. Kim, S. J. Yoo, W. C. Yoo, Y.-E. Sung, J. Mater. Chem. A 2017, 5, 4199.

[17] N. P. Wickramaratne, J. Xu, M. Wang, L. Zhu, L. Dai, M. Jaroniec, Chem. Mater. 2014, 26, 2820.

Chapter 4
Conclusions

In this work, we have evaluated various organic and inorganic nanoparticles with ultrasound treatment and identified the key role of ultrasound in increasing drug delivery. After conjugation of anti-PD-L1 antibody with the contrast agent, we were able to observe cavitation-mediated enhancement of PD-L1 expression at the tumor. Furthermore, the synergistic effect of nanoparticles and microbubble-coupled ultrasound irradiation in drug delivery was observed drug-loaded albumin nanoparticles and MFL nanoparticles. Their anticancer effects were confirmed in animal experiments. In addition, the use of ultrasound allowed improvement in photoacoustic-based diagnostic imaging performance, as well as sonodynamic mechanisms inducing drug release from porphyrin-based nanoparticles in the absence of high-pressure ultrasound and contrast medium. With inorganic nanoparticles, a proof-of-concept in vitro experiment was designed to confirm the compatibility of ultrasonic irradiation with carbon-based and iron oxide nanoparticles. Although the results were not as dramatic, we were able to achieve a strong control of MRI performance using iron oxide nanoparticles.

We believe that the synergistic effect between the nanoparticle-based drug delivery system and ultrasound will become a strong foundation in conquering cancer. It is expected that the additional physical phenomena of ultrasonic waves, including enhanced penetration, physical pressure,

and nanoparticle fusion technology with a very small size can maximize the anticancer effect by breaking through the cancer tissue's defense mechanism and physical barriers.

국 문 초 록

암은 가장 치명적인 질병 중 하나로 현재 이를 극복하기 위한 다양한 연구가 진행 중입니다. 그럼에도 불구하고 가장 널리 사용되는 항암제는 종종 환자에게 심각한 부작용을 일으켜 사용에 제한적이며 보다 효과적으로 부작용을 줄일 수 있는 치료법이 시급한 상황입니다. 이 논문에서는 부작용 감소 및 항암 효과 개선을 위한 초음파 약물 전달 및 진단에 대한 일련의 연구를 수행하였습니다. 실험에 사용된 약물전달물질인 나노입자는 크게 유기물질과 무기물질로 구분되어집니다. 유기 나노입자는 조영제로 사용되는 마이크로버블, 인지질로 이루어진 리포좀, 인간 혈청 알부민을 기반으로 한 알부민 나노입자, 고분자와 포피린으로 이루어진 미셀, 인지질과 포피린으로 이루어진 초음파 감응성 리포좀을 포함하고 있습니다. 무기물로 구성된 나노입자에는 탄소계-나노입자와 산화철 나노입자가 있습니다.

먼저, 마이크로버블(~1,000 nm 크기)를 면역 치료제인 항 PD-L1 항체와 접합시켜 면역 마이크로버블 복합체(Immuno-Microbubble Complex)를 형성하였습니다. 이러한 마이크로버블은 초음파 에너지를 흡수하고 종양 미세환경의 혈관 조직 주위에 일시적인 구멍을 만들 수 있는

것으로 알려져 있습니다. 이러한 마이크로버블이 터지면서 기포 인지질에 부착된 PD-L1 항체는 암세포를 더 잘 표적화하여 생체 내 실험에서 관찰된 바와 같이 효능과 독성을 개선할 수 있었습니다(Kim et al 2020). 또한 desolvation method를 사용하여 인간 혈청 알부민을 이용한 알부민 나노입자를 합성하였고, 동물 실험을 통해 마이크로버블과 초음파와 결합하여 약물 전달 물질로써 가능성을 입증하였습니다(Kim et al 2020).

또한 리포좀 기반의 실험도 진행하였습니다. 먼저, 세포막과 융합하도록 설계된 인지질(membrane fusogenic liposomes, MFL)로 이루어진 리포좀에 소량의 도세탁셀을 로딩하였고 이를통한 세포 및 동물 실험을 통해 물질의 항암효과를 확인하였습니다. 또한, 동물 실험을 통해 초음파 치료 시 화학요법제를 방출하도록 설계된 포피린 기반 리포좀(DLPL)의 항암 효과가 마이크로버블 기반 캐비테이션이 아니라 Sonodynamic에 의한 약물 방출임을 확인했습니다. 마지막으로 고분자와 포피린을 합성하여 마이셀을 제조한 후 PSMA 표적물질을 개발하고 동물 실험을 통해 광음향 장비를 통한 전립선암 영상 성능 향상을 확인했다.

무기 물질로 구성된 나노 입자의 경우 초음파에 노출되면

제어된 방식으로 산화철 나노 입자가 방출되는 초음파 민감성 리포좀에서 개선된 MRI 성능이 확인되었습니다. 마지막으로 탄소 기반 나노입자를 약물에 담지하고 초음파 치료 시 약물의 방출과 치료 효과를 시험관 내 실험을 통해 평가했습니다. 탄소계-나노입자에 대한 약물 로딩은 50% 이상이었지만 초음파 조사를 통한 약물의 방출은 10% 미만이어서 높은 방출률을 보이진 않았지만 세포실험을 통해 세포독성을 확인했고, 입자 표면을 개선해 약물과의 상호작용을 조절할 수 있는 입자를 개발하면 지금보다 더 좋은 결과를 얻을 수 있음을 시사하였습니다.

초음파와 임상 현장에서 사용할 수 있는 다양한 나노입자의 융합 기술을 통해 항암치료 및 진단 영상의 가능성을 확인할 수 있었습니다.

주요어: 암, 초음파, 약물전달, 나노입자, 테라노스틱스

학 번: 2017-29842